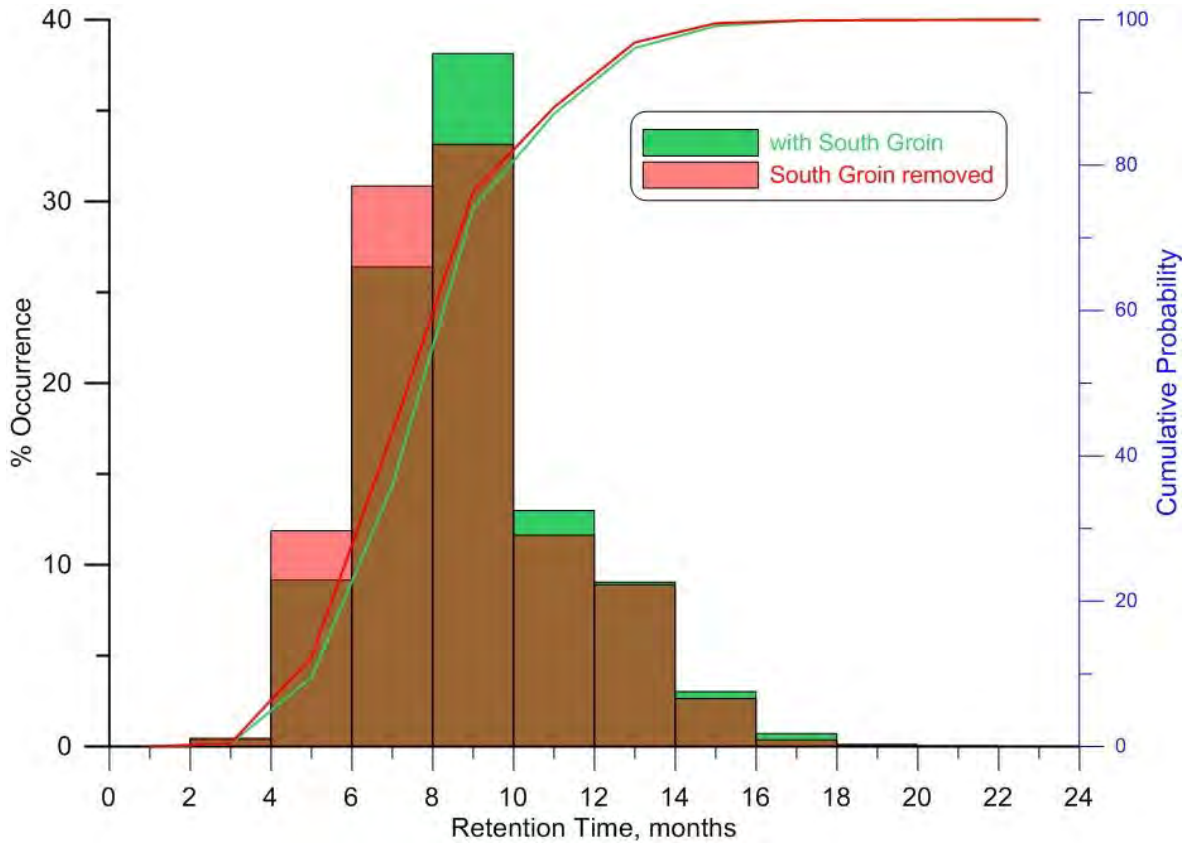Appendix L   Technical Memorandum: Shoreline Evolution
              Analysis of Impacts Related to Removal of the
              South Beach Groin at Encina Power Station,
              Carlsbad, CA by Scott A. Jenkins, PhD
              (February 2013)

Technical Memorandum: Shoreline Evolution Analysis of Impacts Related to Removal of the South Beach Groin at Encina Power Station**,** Carlsbad, CA

Submitted by:

Scott A. Jenkins, Ph.D.
Dr Scott A. Jenkins Consulting
14765 Kalapana St
Poway, CA 92064

Submitted to:

Sheila Henika, P.E. MBA-TM
NRG Cabrillo Power Operations Inc.
Encina Power Station
4600 Carlsbad Blvd.
Carlsbad, CA 92008

Revised: 28 February 2013

ABSTRACT: This study invokes a well-tested and peer-reviewed Coastal Evolution Model to assess potential beach impacts in the near-field of Encina Power Station as a consequence of removal of the stone rip-rap jetty on South Beach (South Beach Groin) that presently amours a fuel oil pipeline. (This pipeline is being de-commissioned by the power station). From computer simulations using this model to predict shoreline evolution over 20-year long historic periods of waves, tides, currents and dredge disposal, the following conclusions were reached: 1) The South Beach Groin has no apparent effect on shoreline change over the short-term. Only after five years is there a discernible difference in shoreline change in the absence of the South Beach Groin, and this difference is localized to South Beach, where removal of the South Beach Groin causes a small amount of shoreline retreat on the order of 6 ft in the immediate neighborhood of the groin's present location (400 ft to 500 ft south of the discharge channel). 2) Shoreline change impacts related to removal of the South Beach Groin are cumulative over time and generally erosional in nature relative to the present condition with the groin in place. Over longer time periods (10 yr. to 20 yr.) these erosional impacts are not confined to the immediate neighborhood of the present location of the South Beach Groin, but the largest impacts occur at South Beach where beach widths are reduced locally by as much as 17 ft, 20 years after the groin is removed. Removal of the South Beach Groin reduces the median retention time of dredged sands placed on South Beach by 1 month; while longer retention times on the order of 18 months to 20 months are only possible with the South Beach Groin remaining in its present condition and location. The reason shoreline change impacts related to removal of the South Beach Groin are cumulative and not localized entirely to South Beach is because of the long term effects of back-passing. Since dredging and beach disposal of the dredged sands typically occurs every 2 years, an average loss of 1 month of retention time adds up to a significant loss of beach sand volume over many years for the North Beach/Middle Beach/South Beach back-passing, sand re-cycling system.

1.0) Introduction:

The California State Lands Commission is requiring an evaluation of potential beach and shoreline impacts that might result from removal of the South Beach Groin shown in Figures 1 & 2, presently located 403 ft south of the cooling water discharge channel at Encina Power Station, Carlsbad, CA. Long term littoral drift rates and equilibrium beach profile and shoreline changes are computed in sensitivity analyses involving periodic beach disposal of dredged sands from Agua Hedionda Lagoon dredging. This equilibrium beach profile sensitivity analysis is computed with present back-passing dredge disposal permit requirements. (Back-passing has been a City of Carlsbad, California Coastal Commission and California Department of Parks and Recreation permit requirement with the City of Carlsbad as the lead requestor).
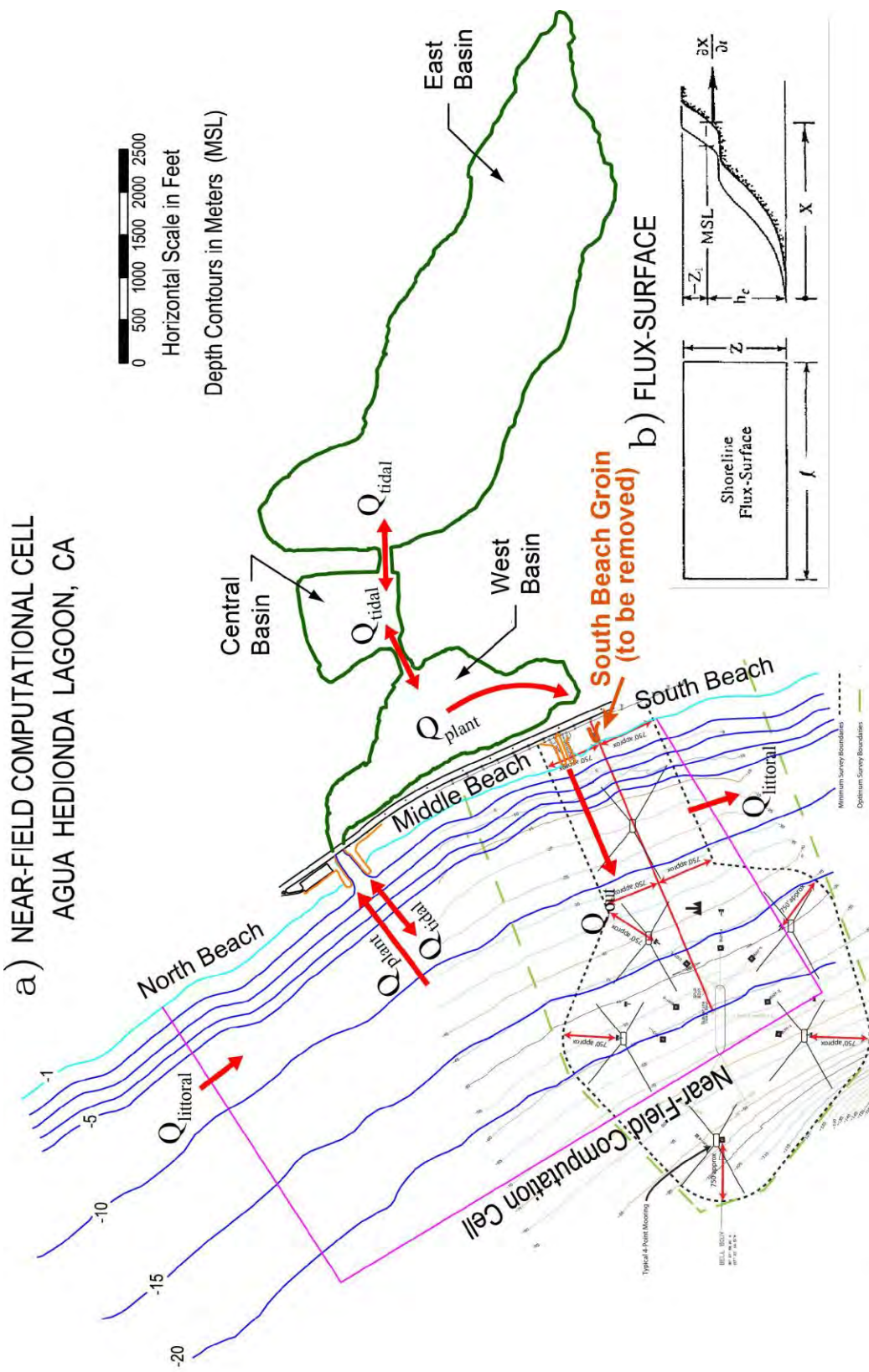
3

Figure 1. Near-field computational cell for calculating sediment transport at Agua Hedionda Lagoon, CA; a) Lagoon Plan View. b) Beach Cross-section.

Figure 2: Google Earth image of the South Beach Groin presently located 403 ft south of the cooling water discharge channel at Encina Power Station, Carlsbad, CA.

The present day Agua Hedionda Lagoon is not a natural geomorphic structure; rather, it is a construct of modern dredging. Its West Tidal Basin (Figure 1) is unnaturally deep (-20 to – 25 ft MLLW) and the utilization of lagoon water for once-through cooling by the Encina Power Station renders Agua Hedionda's hydraulics distinctly different from any other natural tidal lagoon. Power plant cooling water uptake (Q_{plant}) acts as a kind of "negative river." Whereas natural lagoons have a river or stream adding water to the lagoon, causing a net outflow at the ocean inlet, the power plant infall removes water from Agua Hedionda Lagoon, resulting in a net inflow of water (Q_{plant}) through the ocean inlet. This net inflow has several consequences for sediment transport into and out of the lagoon: 1) it draws nutritive particulate and suspended sediment from the surf zone into the lagoon, the latter forming bars and shoals that subsequently restrict the tidal circulation, and 2) the net inflow of water diminishes or at times cancels the ebb flow velocities out of the inlet, thereby providing insufficient transport energy to flush sediments (essentially uphill) out of the deep West Basin of the lagoon. Therefore, the plant demand for lagoon water strongly controls the rate at which Agua Hedionda traps sediment and other solid particulate, but is not the only controlling factor.

Variations in local beach sand volumes and wave climate can also have a significant effect on sand influx rates at Agua Hedionda. Computer simulations for the North Jetty Restoration Project by Jenkins and Wasyl (2001) showed that back passing as required under current dredge permits has significantly increased sand influx rates over prior historic rates at equivalent power plant water consumption rates. Grain size analysis and X-Ray diffraction "fingerprinting" of the newly deposited lagoon sediments conducted by Jenkins and Wasyl (2003) produced a self-consistent body of evidence that the San Diego Regional Beach Sand Project has increased sedimentation rates at Agua Hedionda Lagoon on the order of 84% in spite of benign wave climate during the intervening period.

Table 1 gives a listing of the complete dredging history at Agua Hedionda Lagoon. The dredging events listed as "maintenance" in Table 1 occurred within the recharge zone of the West Basin (Figure 1) and give estimates of sediment influx rates when the volumes for these events are factored against the time intervals between them.

Table 1. Dredging and Disposal History at Agua Hedionda Lagoon (from Jenkins and Wasyl, 2001)

Dredging And Disposal History						
Year	**Dredging**			**Disposal**	**Comments**	
	Date		Volume (yds^3)	Basin Dredged	Volume (yds^3)	Location Placed 1
	Start	Finish				
1954	Feb-54	Oct-54	4,279,319	Outer, Middle, & Inner	4,279,319	N, M, S	Initial construction dredging
1955	Aug-55	Sep-55	90,000	Outer	90,000	S	Maintenance
1957	Sep-57	Dec-57	183,000	Outer	183,000	S	Maintenance
1959-60	Oct-59	Mar-60	370,000	Outer	370,000	S	Maintenance
1961	Jan-61	Apr-61	227,000	Outer	227,000	S	Maintenance
1962-63	Sep-62	Mar-63	307,000	Outer	307,000	S	Maintenance
1964-65	Sep-64	Feb-65	222,000	Outer	222,000	S	Maintenance
1966-67	Nov-66	Apr-67	159,108	Outer	159,108	S	Maintenance
1968-69	Jan-68	Mar-69	96,740	Outer	96,740	S	Maintenance
1972	Jan-72	Feb-72	259,000	Outer	259,000	S	Maintenance
1974	Oct-74	Dec-74	341,110	Outer	341,110	M	Maintenance
1976	Oct-76	Dec-76	360,981	Outer	360,981	M	Maintenance
1979	Feb-79	Apr-79	397,555	Outer	397,555	M	Maintenance
1981	Feb-81	Apr-81	292,380	Outer	292,380	M	Maintenance
1983	Feb-83	Mar-83	278,506	Outer	278,506	M	Maintenance
1985	Oct-85	Dec-85	403,793	Outer	403,793	M	Maintenance
1988	Feb-88	Apr-88	333,930	Outer	103,000	N	Maintenance
					137,860	M	Maintenance
					93,070	S	Maintenance
1990-91	Dec-90	Apr-91	458,793	Outer	24,749	N	Maintenance
					262,852	M	Maintenance
					171,192	S	Maintenance
1992	Feb-92	Apr-92	125,976	Outer	125,976	M	Maintenance
1993	Feb-93	Apr-93	115,395	Outer	115,395	M	Maintenance
1993-94	Dec-93	Apr-94	158,996	Outer	74,825	N	Maintenance
					37,761	M	Maintenance
					46,410	S	
1995-96	Sep-95	Apr-96	443,130	Outer	106,416	N	Maintenance
					294,312	M	
					42,402	S	
1997	Sep-97	Nov-97	197,342	Outer	197,342	M	Maintenance

Table 1. Continued

Year	Dredging		Volume(yds^3)	Basin Dredged	Disposal Volume (yds^3)	Comments	
	Date					Location Placed 1	
	Start	Finish					
1998	Dec-97	Feb-98	60,962	Middle	60,962	M	Modification dredging
	Feb-98	Feb-99	498,736	Inner	370,297	M	Modification dredging
					128,439	S	
1999	Feb-99	May-99	202,530	Outer	202,530	N	Maintenance
2000-01	Nov-00	Apr-01	429,084	Outer	142,000	N	Maintenance
					202,084	M	
					85,000	S	
2002-03	Dec-02	Apr-03	336,357	Outer	100,907	N	Maintenance
					141,270	M	
					94,180	S	
2004-05	Jan-05	Mar-05	348,151	Outer	104,446	N	Maintenance
					146,223	M	
					97,482	S	
2006-07	Jan-07	Apr-07	333,373	Outer	100,012	N	
					140,017	M	
					93,344	M	Maintenance
Total (Construction + Maintenance)			12,310,247		12,310,247		
Sub-Total (Maintenance Only)			7,471,380		7,471,380		

N = North Beach

M = Middle Beach

S = South Beach

Beach erosion, longshore transport of sand and sand influx into the lagoon are impacted El Nino/Southern Oscillation (ENSO) events and long-term climate oscillations such as the Pacific Decadal Oscillation (PDO). These cyclical climate events cause intensification of wave climate, accelerated beach erosion and transport; and consequently more suspended sediment in the neighborhood of the lagoon inlet to be entrained by the net inflowing stream. However, the sand influx rates are further impacted by beach nourishment activities up-drift of the lagoon. Beach nourishment activities up-drift of Agua Hedionda are seen to have roughly doubled the daily influx rates to 400-600 cubic yards per day, as occurred following beach building projects in 1963, 1973, 1982, 1994 and 2001. Because of the transient impacts of beach restoration on sand influx rates, comparisons between Table 1 and Appendix-A reveal that historically sand influx rates rise dramatically in years during and immediately following beach nourishment activities in Oceanside or Carlsbad. This was first explained by Inman & Jenkins (1983) in terms of the longshore transport rate Q_L (cf. Figure 3) in this region being sand supply limited. In other words there is more potential transport than the available sand supply can sustain. Any artificial intervention that increases updrift sand supply will increase longshore transport rates, and thereby increase the rates at which sand moves by the inlet and made available for tidal entrainment into the lagoon, with the ultimate consequence of increased lagoon maintenance dredging and subsequent beach disposal of dredged sands.

Additional sand has historically been placed on the regional beaches from sources outside of Agua Hedionda. These historic beach fills are listed in Appendix A and involved sand sources from construction and maintenance dredging of Oceanside Harbor and from beach nourishment projects using watershed sources (cf. Figure 3a). The lagoon prior to the late 1980's typically ingested 200-300 cubic yards per day, *unless* major updrift nourishment occurred at Oceanside or Carlsbad. Beach nourishment in the neighborhood of Agua Hedionda correlate with doubling of the influx rates, increasing to as much as 400-600 cubic yards per day. This occurred in 1963, 1973, 1982 and 1994 (Appendix A). The most dramatic example of such beach nourishment impacts occurred subsequent to the massive beach building projects in 1982, when 923,000 cubic yards of
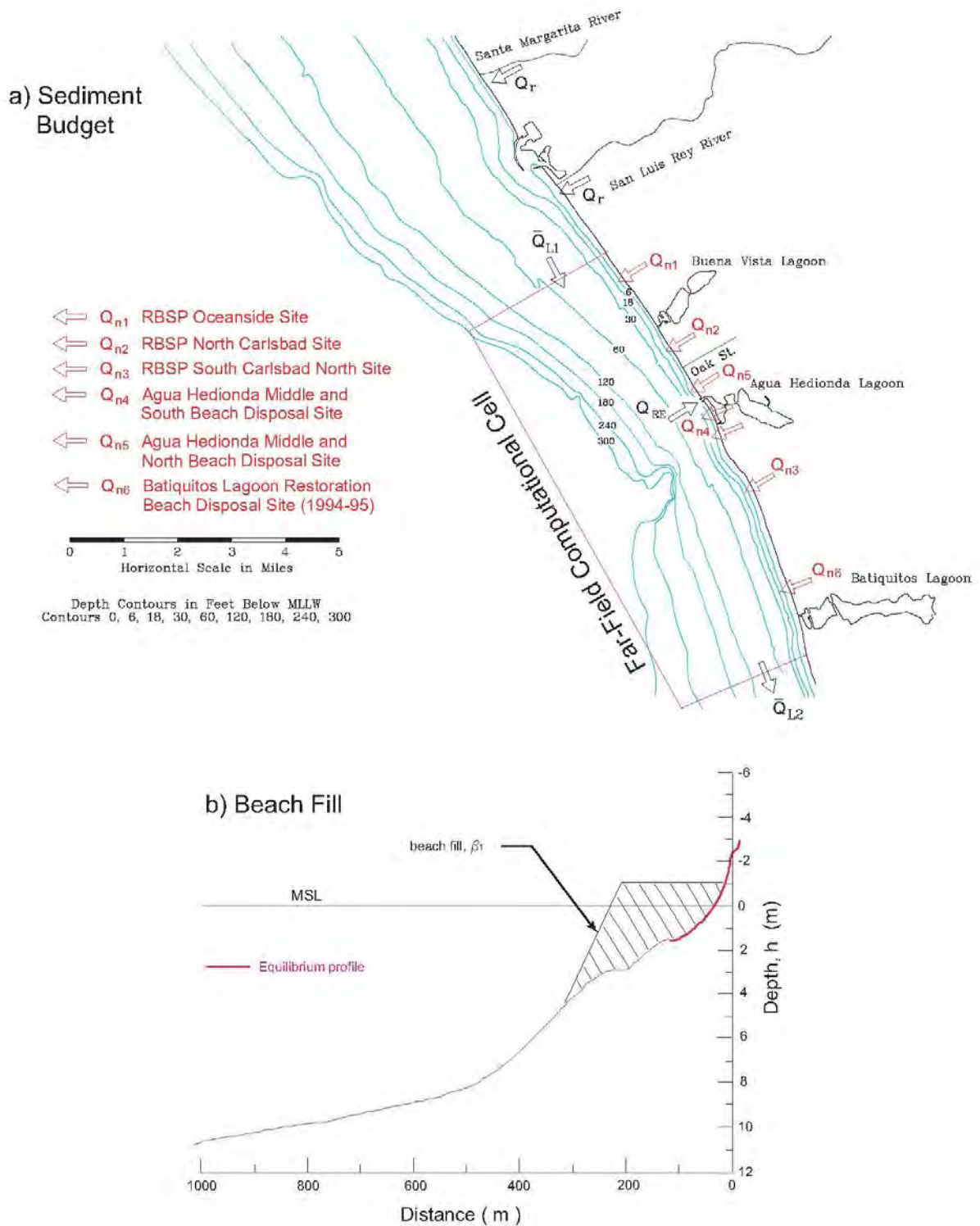
Figure 3: (a) Sediment budget in the far-field of Agua Hedionda Lagoon and the South Beach Groin; (b) Schematic of beach-fill templates for dredge disposal and beach nourishment

new sand was truck hauled from the San Luis Rey River and placed on Oceanside beaches. Coincidentally, the 1983-85 biannual maintenance dredging cycle of the west basin of Agua Hedionda yielded 403,793 cubic yards. This volume equates to an average daily influx rate of 401 cubic yards per day during that two year period. Such high daily influx rates had not been seen since 1960 when 841,200 cubic yards of beach nourishment was placed on Oceanside beaches following new construction dredging and enlargement of Oceanside Harbor facilities.

After the late 1980's there was only one minor beach nourishment project in Oceanside involving infusions of **new** sand, when 40,000 cubic yards were placed in 1994 (see Appendix B and Table 1). However beginning in 1988, the City of Carlsbad imposed conditions requiring *back-passing* defined fractions of the Agua Hedionda dredge volume north of the inlet. Although this action functions as beach nourishment for the North Carlsbad beaches, it does not represent the introduction of new sand to the littoral system. Rather, it is a backward cycling of existing sand that would otherwise proceed southward under the influence of the net littoral drift following conventional down-drift disposal . In 1988, 103,000 cubic yards were back-passed from Agua Hedionda to North Beach in Carlsbad, with a subsequent influx of 458,973 cubic yards into Agua Hedionda Lagoon by 1990, giving an influx rate of about 419 cubic yards per day. During 89 days of dredging operations between December 20, 1993 and April 26, 1994, there were 74,825 cubic yards placed immediately north (updrift) of the Agua Hedionda Lagoon and inlet jetty at the North Beach disposal site. The daily influx rate during this 89 day period rose to an average of 782 cubic yards per day. In 1996 there was 106,416 cubic yards of back-passing dredged sands from Agua Hedionda to North Beach and influx rates increased to 540 cubic yards per day in the 6 months that followed. Although the volume of back-passing has been small relative to prior nourishment efforts in Oceanside, its effect on influx was large due to the close proximity of North Beach to the inlet of Agua Hedionda and the low retention of sand on this beach in the presence of rocky substrate immediately offshore, Elwany et al. (1999) .

Following the east basin dredge project, 202,530 cubic yards were back-passed to North Beach in April 1999. A dredge survey in July 2000 determined that 360,800 cubic

yards had fluxed into the lagoon, increasing the daily rate to an average of 846 cubic yards per day. Throughout the period of record, the percentage of lagoon dredging that has been back-passed to North Beach averages 14.7% of the total dredge volume. The remaining fraction of dredge volume that was not back-passed was divided between the Middle and South Beach disposal sites in an historically averaged split of 85% to 15%.

More recent maintenance dredging event at Agua Hedionda Lagoon involved 429,084 cubic yards dredged during the period between 1 November 2000 and 18 April 2001. Of this total, 142,000 cubic yards were back-passed to North Beach. This represents a back-passing load of 33 %, in excess of the 20 % return load estimated by Elwany (1999) to result naturally from longshore transport reversals. (After considering recreational needs and property valuations of Carlsbad in isolation, Elwany, 1999 recommended a back passing load of 30 % of the long term dredging burden). The remaining fraction of the 2000/01 dredging that was not back-passed to the north was placed on the down-drift side of the inlet on Middle and South Beaches in a 70 % to 30 % split. The implementation of 30% back-passing at Agua Hedionda Lagoon concurrent with the construction of the San Diego Regional Beach Sand Project (RBSP) set the antecedent conditions for the influx of over a million cubic yards of sand through the lagoon inlet in the following 5 year period, 2002-2007, despite dramatic decline of cooling water consumption beginning in 2006 (cf. Figure 3).

The as-built specifications for the RBSP indicate that 2,104, 000 cubic yards were dredged from 4 offshore borrow sites to nourish the 12 designated beaches. Thus, more sand was dredged from fewer borrow sites than specified by the EIR. As a result some beaches received considerably more sand than stated by the EIR (AMEC, 2002), in particular the South Oceanside site updrift of Agua Hedionda (see Figure 8) that was scheduled in th EIR to receive 380,000 cubic yards, but actually received 421,000 cubic yards. The EIR had designated borrow sites SO-7 and SO-9 to supply sand to the 4 receiver beaches in the immediate neighborhood of Agua Hedionda (South Oceanside, North Carlsbad, South Carlsbad State Beach, and Batiquitos), but actual construction used Borrow sites SO-5 and SO-7. These 4 nearest-neighbor beach fill sites received 921,000 cubic yards of new sand having the sediment properties detailed in AMEC, (2002). Due to the proximity of theses beaches (Figure 8a), this unprecedented volume of

new sand was within 1 year travel time of Agua Hedionda at typical littoral drift rates (see Inman & Jenkins, 1985). Not only is this the largest volume ever placed at single time this close to the lagoon, but it was placed simultaneously on both the up-drift and down-drift sides of the lagoon, so that the lagoon remains on the receiving side of the littoral drift regardless of littoral drift reversals.

Dynamically, Agua Hedionda is nested in a sub-cell in the southern end of the Oceanside Littoral Cell (between South Oceanside and the Scripps Submarine Canyon near Torrey Pines) where the RBSP placed 1,833,000 cubic yards within a 5 ½ month period. Sand freely moves back and forth along shore without obstruction in this sub-cell (Figure 3) under the influence the net (southward) littoral drift and episodic reversals to that drift. Altogether the San Diego Regional Beach Sand Project was unprecedented in the history of the region for importation of the largest amount of sand in the shortest period of time, with nearly half that sand placed in the nearfield of Agua Hedionda. The delivery rate of this sand directly to the beaches greatly exceeded natural rates of delivery from regional watersheds, which would first deposit new sand as a sand delta that gradually migrates and diffuses along shore as an accretion wave to nourish the beaches (see Inman & Jenkins, 1985, and 2002). In other words, beaches need time to "digest" new sand and assimilate that new sand in an equilibrium profile. The accretion wave mechanism provides that digestive process in Nature. Furthermore, the RBSP sands were placed in construction templates that were not configured as equilibrium beach profiles. The shore-face slopes of these templates were much steeper than the slopes of natural equilibrium profiles (see Figure 3b). For example, at the North Carlsbad and South Carlsbad State Beach receiver sites (immediately adjacent to Agua Hedionda) the RBSP beach fill was placed at 10:1 slopes and at 20:1 slopes at South Oceanside. These slopes are far in excess of the 2:100 or 3:100 slopes typical of natural equilibrium beach profiles in this region (Inman, et al 1993). Because of the high delivery rates and artificially steep slopes of the sands placed by the RBSP, those sands were highly mobile in the post-construction period as wave action reworks them into equilibrium beach and shoreline configurations. This mobility was further enhanced by the presence of significant fractions in the RBSP sands that are finer than the native beach sand (AMEC, 2002). As a consequence of this remarkably adverse set of circumstances, sand influx rates at Agua

Hedionda Lagoon have been historically unprecedented in the post RBSP period, with daily mean influx rates reaching an historical high of 613 cubic yards per day as determined from the 2001 West Basin dredge statistics; and sustaining historically high rates since, measuring 461 cubic yards per day from the 2002-03 dredging; 495 cubic yards per day from the 2004-05 dredging; and 437 cubic yards per day from the 2006-07 dredging.

2.0) Technical Approach:

The computer model simulations involve a littoral transport/beach equilibrium model used to determine the rate of delivery of littoral sediments to the nearfield beaches at Encina Power Station, (including North Beach, Middle Beach and South Beach, cf. Figure 1) and the subsequent impact of the removal of the South Beach Groin. The numerical details of these models in a generalized Coastal Evolution Model are discussed in Jenkins and Wasyl, 2005 (http://repositories.cdlib.org/sio/techreport/58/). The littoral transport model has two computational domains, a *farfield computational cell* (Figure 3) containing the Oceanside receiver beaches and a *nearfield computational cell* (Figure 1) that is nested inside the farfield and contains the details of North Beach, Middle Beach and South Beach and the South Beach Groin. The nearfield cell computes local wave shoaling and resulting littoral transport rates in the immediate neighborhood of these beaches and rip-rap structures. The tidally induced transport of the lagoon explicitly interacts with the littoral transport within the nearfield cell, and the differences in the tidal velocities between the pre- and post-dredging are accounted for in that interaction. The nearfield cell also accommodates sediment sources associated with beach sand volume changes on North, Middle and South Beach occurring from dredge disposal during maintenance dredging cycles.

The nearfield cell receives littoral sediments from more distant sources, and these are accounted for in the farfield cell. The farfield cell computes fluxes of sediment into the nearfield cell due to regional scale divergence of drift and from sediment sources outside the nearfield cell, principally the beach fill sites associated with the beach restoration efforts in north Carlsbad and South Oceanside, and Oceanside Harbor dredging activities, as listed in Appendix A. Fluxes of sediment into the farfield cell from the net of the harbor effect are critical in limiting the fluxes within the farfield cell

associated with divergence of the net longshore transport. These controlling fluxes were detailed in Jenkins and Wasyl (2001) and are based on long-term averages derived from the sediment budget of the Oceanside Littoral Cell.

Both the near and farfield wave forcing and sediment budget inputs vary in time due to climatic variability. This variability during and after the dredge disposal will be evaluated in Section 3, and the impact on the farfield's ability to supply the nearfield with littoral sediment is quantified by the model analysis in Section 3. The wave climate variability also causes adjustments to beach profiles, resulting in sand volume changes through cyclical erosion and accretion. These changes to the equilibrium beach profile are further altered by beach construction fill and divergence of drift changes to the mean shoreline position. Effects of removal of the South Beach Groin on littoral sand volume, beach equilibrium and mean shoreline position are evaluated in Section 4.

The Coastal Evolution Model (CEM) is a process-based numerical model. It consists of a Littoral Cell Model (LCM) and a Bedrock Cutting Model (BCM), both coupled and operating in varying time and space domains (Figure 4) determined by sea level and the coastal boundaries of the littoral cell at that particular sea level and time. At any given sea level and time, the LCM accounts for erosion of uplands by rainfall and the transport of mobile sediment along the coast by waves and currents, while the BCM accounts for the cutting of bedrock by wave action in the absence of a sedimentary cover.

In both the LCM and BCM, the coastline of the littoral cell is divided into a series of coupled control cells (Figure 5). Figure 6 shows the arrangement of coupled control cells used to model the impacts of removal of the South Beach Groin. Each control cell is a small coastal unit of uniform geometry where a balance is obtained between shoreline change and the inputs and outputs of mass and momentum. The model sequentially integrates over the control cells in a down-drift direction so that the shoreline response of each cell is dependent on the exchanges of mass and momentum between cells, giving continuity of coastal form in the down-drift direction. Although the overall computational domain of the littoral cell remains constant throughout time, there is a different coastline position at each time step in sea level. For each coastline position there exists a similar set of coupled control cells that respond to forcing by waves and current. Time and space scales used for wave forcing and shoreline response (applied at
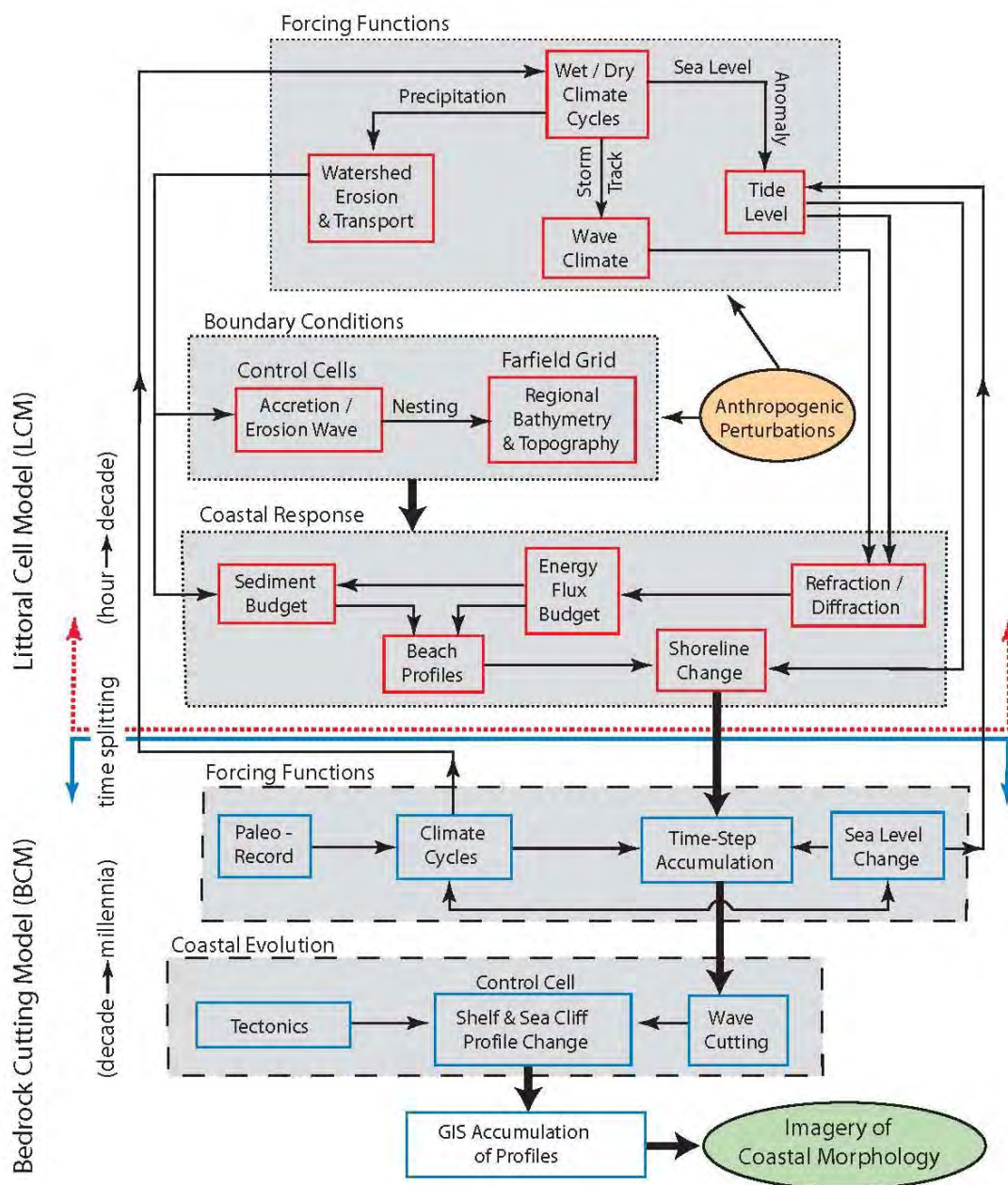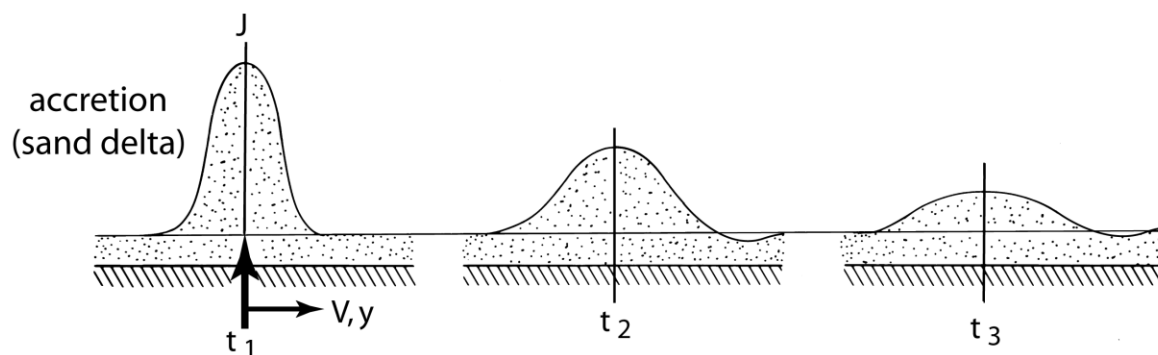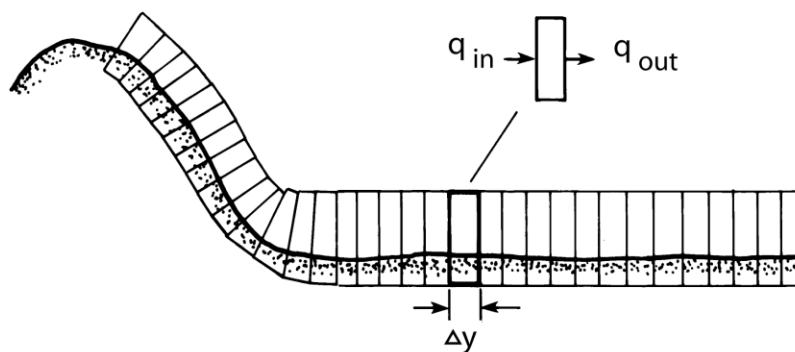
Figure 4: Architecture of the Coastal Evolution Model consisting of the Littoral Cell Model (above) and the Bedrock Cutting Model (below). Modules (shaded) are formed of coupled primitive process models. (from Jenkins and Wasly, 2005).

a) Accretion / Erosion Wave
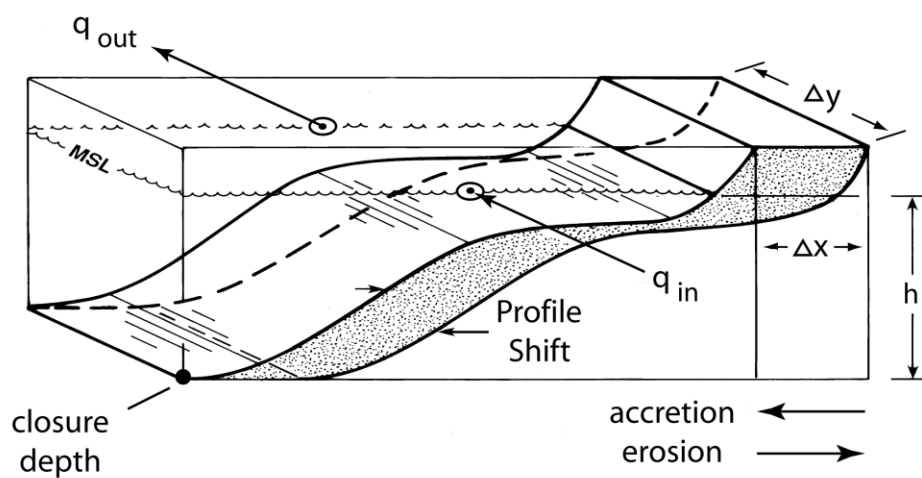

b) Coupled Control Cells

c) Profile Changes

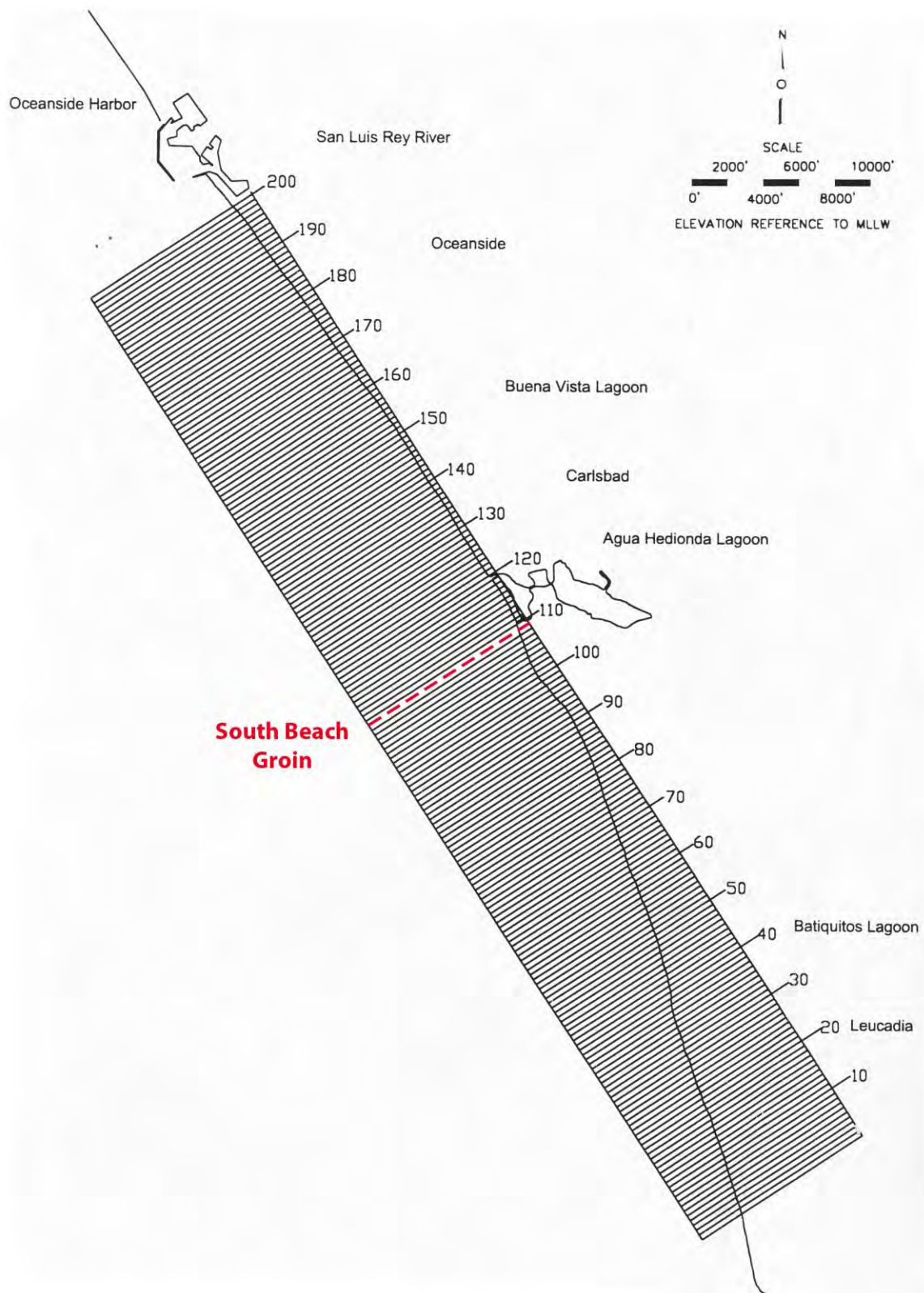**Figure 5:** Computational approach for modeling shoreline change after Jenkins, et. al., (2007).

Figure 6: Arrangement of coupled control cells used to model the impacts of removal of the South Beach Groin.

6 hour intervals) and sea level change (applied annually) are very different. To accommodate these different scales, the model uses multiple nesting in space and time, providing small length scales inside large, and short time scales repeated inside of long time scales.

The LCM (Figure 4, upper) has been used to predict the change in shoreline width and beach profile resulting from the longshore transport of sand by wave action where sand source is from river runoff or from tidal exchange at inlets (e.g., Jenkins and Inman, 1999). More recently it has been used to compute the sand level change (farfield effect) in the prediction of mine burial (Jenkins and Inman, 2002; Inman and Jenkins, 2002). Time-splitting logic and feedback loops for climate cycles and sea level change were added to the LCM together with long run time capability to give a numerically stable couple with the BCM.

In the LCM, the variation of the sediment cover with time is modeled by time-stepped solutions to the sediment continuity equation (otherwise known as the *sediment budget*) applied to the boundary conditions of the coupled control cell mesh diagramed schematically in Figure 3. The sediment continuity equation is written (Jenkins, et al, 2007):

$$\frac{\partial q}{\partial t} = \frac{\partial}{\partial y}\left(\varepsilon \frac{\partial q}{\partial y}\right) - V_l \frac{\partial q}{\partial y} + J(t) - R(t) \tag{1}$$

Where q is the sediment volume per unit length of shoreline (m^3/m), ε is the mass diffusivity, V_l is the longshore current, $J(t)$ is the flux of new sediment into the littoral cell from watresheds and $R(t)$ is the flux of sediment lost to sinks , typically submarine canyons, lagoons, spits, harbors or windblown losses. The first term in (1) is the surf diffusion while the second is divergence of drift. For any given control cell in Figure 10, (1) may be discretized in terms of the rate of change of beach volume, V, in time t, given by:

$$\frac{dV}{dt} = J(t) + q_{L1} + q_{RE} - q_{L2} \tag{2}$$

Sediment is supplied to the control cell by the sediment yield from the rivers, $J(t)$, by the influx littoral drift from up-coast sources, q_{L1} and by new sediment that recharges the system q_{RE} as a consequence of bluff erosion within the control cell. Sediment is lost from the control cell due to the action of wave erosion and expelled from the control cell by exiting littoral drift, q_{L2}. Here fluxes into the control cell ($J(t)$ and q_{L1}) are positive and fluxes out of the control cell (q_{RE} and q_{L2}) are negative. The beach sand volume change, dV/dt, is related to the change in shoreline position, dX/dt, according to:

$$\frac{dV}{dt} = \frac{dX}{dt} \cdot Z \cdot l \tag{3}$$

where $$Z = Z_1 + h_c \tag{4}$$

Here, Z is the height of the shoreline flux surface equal to the sum of the closure depth below mean sea level, h_c, and the height of the berm crest, Z_1, above mean sea level; and l is the length of the shoreline flux surface. Hence, beaches and the local shoreline position remain stable if a mass balance is maintained such that the flux terms on the right-hand side of equation (2) sum to zero; otherwise the shoreline will move during any time step increment as:

$$\Delta x(t) = \frac{1}{\Delta y(Z_1 + h_c)} \int \left(\frac{\partial}{\partial y}\left(\varepsilon \frac{\partial q}{\partial y} \right) - V \frac{\partial q}{\partial y} + J(t) \right) dt \tag{5}$$

where ε is the mass diffusivity, V is the longshore drift , J is the flux of sediment from river sources, Δy is the alongshore length of the control cell, and Z_1 is the maximum run-up elevation from Hunt's Formula. River sediment yield, J, is calculated from streamflow, Q, based on the power law formulation of that river's sediment rating curve after Inman and Jenkins, (1999), or

$$J = \gamma \, Q^{\omega} \tag{6}$$

where γ, ω are empirically derived power law coefficients of the sediment rating curve from best fit (regression) analysis (Inman and Jenkins,1999). When river floods produce large episodic increases in J, a river delta is initially formed. Over time the delta will widen and reduce in amplitude under the influence of surf diffusion and advect down-coast with the longshore drift, forming an accretion erosion wave (Figure 16a). The local sediment volume varies in response to the net change of the volume fluxes, q, between any given control cell and its neighbors, referred to as divergence of drift = q_{in} - q_{out} , see Figure 16b and 16c. The mass balance of the control cell responds to a non-zero divergence of drift with a compensating shift, Δx , in the position of the equilibrium profile (Jenkins and Inman, 2006). This is equivalent to a net change in the beach entropy of the equilibrium state . The divergence of drift is given by the continuity equation of volume flux, requiring that dq/dt is the net of advective and diffusive fluxes of sediment plus the influx of new sediment, J. The rate of change of volume flux through the control cell causes the equilibrium profile to shift in time according to (5).

The BCM (Figure 4, lower) models the erosion of country rock by wave action when the sediment cover has been completely eroded away (Jenkins and Wasyl, 2005). Because bedrock cutting requires the near absence of a sediment cover, the boundary conditions for cutting are determined by the coupled mobile sediment model, LCM. When LCM indicates that the sediment cover is absent in a given area, then BCM kicks in and begins cutting. BCM cutting is powered by the wave climate input to LCM but applied only to areas where mobile sediment is absent. Bedrock cutting involves the action of wave energy flux ECn to perform the work required to abrade and notch the country rock. Both abrasion and notching mechanisms are computed by the newly developed wave-cutting algorithms. These algorithms use a general solution for the recession R (in meters) of the shelf and sea cliff. The recession rate dR/dt is a function of the incident wave energy flux,

$$\frac{dR}{dt} = \frac{\rho}{\rho_s} f_e \, ECn \qquad (7)$$

where ρ is the density of seawater; ρ_s is the density of the bedrock, and f_e is a function that varies from 0 to 1 and is referred to as the erodibility. The units of the erodibility are the reciprocal of the wave force per unit crest length (m/N). The erodibility is given

separate functional dependence on wave height for the platform abrasion and wave notching of the sea cliff. For abrasion, the erodibility varies with the local shoaling wave height $H_{(x)}$ as

$$f_e = K_a \Theta_{ij} H_{(x)}^{1.63} \text{ (abrasion)} \tag{8}$$

where Θ_{ij} is the bedrock failure shape function and K_a is an empirical constant. Consequently, recession by abrasion is a maximum at the wave breakpoint (at a depth of about 5/4 the breaking wave height, H_b) and decreases in both the seaward and shoreward directions. In contrast, the erodibility of the notching mechanism is a force-yield relation associated with the shock pressure of the bore striking the sea cliff (Bagnold, 1939; Trenhaile, 2002). The shock pressure is proportional to the runup velocity squared, which is limited by wave runup elevation. Wave pressure solutions (Havelock, 1940) give

$$f_e = K_n \Theta_{ij} \eta_r^2 \text{ (notching)} \tag{9}$$

where K_n is an empirical constant and the runup elevation η_r is dependent on the tidal level η_o and the breaking wave height by Hunt's formula,

$$\eta_r = \eta_o + \Gamma H_b \tag{10}$$

Here Γ is an empirical constant from Hunt's formula (*Hunt*, 1959).

To quantify the effect of removal of the South Beach Groin on littoral drift and beach stability, we invoke the LCM algorithms of the Coastal Evolution Model (Figure 4) after initializing for historic wave climate and river sediment flux as detailed in Section 3.. The LCM computational sequence begins with forward refraction calculation using OCEANRDS to solve for the wave height and x and y components of the wave number at each point in the sequence of coupled control cells (Figure 5b and Figure 6). The x and y components of wave number are orthogonalized to compute the significant wave angle

in each grid cell relative to the shoreline normal of these near-field computational cells. The calculation is carried shoreward until the wave height meets or exceeds 5/4 the local depth. This condition defines the point of wave breaking. The wave height, H_b wave angle α_b and grid cell location (x_b, y_b) at which this wave breaking condition is met are written into a *breaker file* for use in subsequent potential longshore transport calculations. The breaker files generated by refraction/diffraction calculations are used to compute the potential longshore transport rates at 6 hour intervals. The formulation for the longshore transport rate is taken from the work of Komar and Inman (1970) according to:

$$q_{L2} = K\left(C_n S_{yx}\right)_b \qquad (11)$$

where q_{L2} is the local potential longshore transport rate; C_n is the phase velocity of the waves; $S_{yx} = E sin\alpha_b\, cos\alpha_b$ is the radiation stress component; α_b is the breaker angle relative to the shoreline normal; $E = 1/8\rho g H_b^2$ is the wave energy density; ρ is the density of water; g is the acceleration of gravity; H_b is the breaking wave height; and, K is the transport efficiency equal to:

$$K = 2.2\sqrt{c_{rb}} \qquad (12)$$

$$c_{rb} = \frac{2g \tan^2 \beta}{H_b \sigma^2} \qquad (13)$$

Here c_{rb} is the reflection coefficient which is calculated from a gross estimate of the nearshore bottom slope, as determined from the bathymetry file using the break point coordinates and the position of the 0 MSL contour; and, σ is the radian frequency = $2\pi/T$, where T is the wave period. These equations relate longshore transport rate to the longshore flux of energy at the break point which is proportional to the square of the near breaking wave height and breaker angle. By this formulation, the computer code calculates a local longshore transport rate for each break point locations along the

shoreline of the forward refraction grid shown in Figures 6. The potential longshore sand transport rates calculated for these points are ensemble averaged for each 6 hour time step interval within the 1980-2000 simulation period to obtain estimates of the fluxes, q_{L2} in-and-out of the near-field computational cell due to local longshore transport (littoral drift).

We use state-of-the-art algorithms for the equilibrium beach profile (Jenkins and Inman,2006) to calculate the long term variability of beach profiles along North Beach, Middle Beach and South Beach in the presence of historic back-passing. This analysis takes into account the effects of the two conditions of the South Beach Groin being in place and being removed. The beach profile algorithms are calibrated using pre- and post dredging beach profile surveys from Jenkins and Wasyl (2010) and Elwany, et al, 1999. The calibrated algorithms are then forced by 24 years of continuous wave data using time varying divergence of drift from equation (1) to compute changes in the mean shoreline position from equation (5).

In Jenkins and Inman (2006), equilibrium beaches are posed as isothermal shorezone systems of constant volume that dissipate external work by incident waves into heat given up to the surroundings. By the maximum entropy production formulation of the second law of thermodynamics (the law of entropy increase), the shorezone system achieves equilibrium with profile shapes that maximize the rate of dissipative work performed by wave-induced shear stresses. Dissipative work is assigned to two different shear stress mechanisms prevailing in separate regions of the shorezone system, an outer solution referred to as the *shorerise* and a *bar-berm* inner solution (Figure 7). The equilibrium shorerise solution extends from closure depth (zero profile change) to the breakpoint, and maximizes dissipation due to the rate of working by bottom friction. In contrast, the equilibrium bar-berm solution between the breakpoint and the berm crest maximizes dissipation due to work by internal stresses of a turbulent surf zone. Both shorerise and bar-berm equilibria were found to have an exact general solution belonging to the class of *elliptic cycloids* (Figure 7b). The elliptic cycloid allows all the significant features of the equilibrium profile to be characterized by the eccentricity and the size of one of the two ellipse axes. These two basic ellipse parameters were related In Jenkins
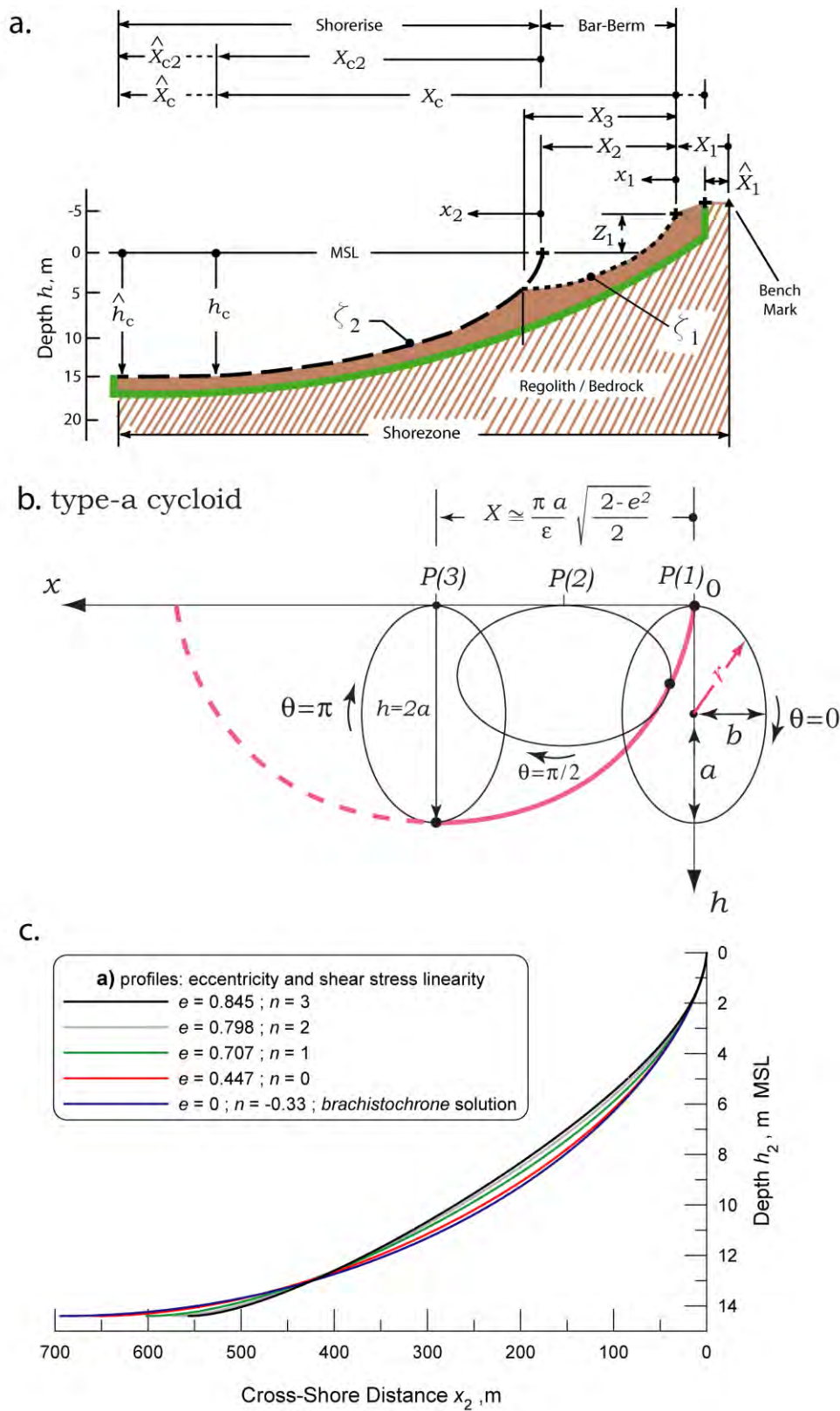
a.

Shorerise — Bar-Berm

$\hat{X}_{c2}$

X_{c2}

$\hat{X}_c$

X_c

X_3

X_2

X_1

x_1

$\hat{X}_1$

x_2

z_1

MSL

Bench Mark

$\hat{h}_c$

h_c

ζ_2

ζ_1

Depth h, m

Regolith / Bedrock

Shorezone

b. type-a cycloid

$$X \cong \frac{\pi a}{\varepsilon}\sqrt{\frac{2-e^2}{2}}$$

x

$P(3)$ $P(2)$ $P(1)_0$

$\theta = \pi$ $h = 2a$

b $\theta = 0$

$\theta = \pi/2$

a

h

c.

a) profiles: eccentricity and shear stress linearity
- $e = 0.845$; $n = 3$
- $e = 0.798$; $n = 2$
- $e = 0.707$; $n = 1$
- $e = 0.447$; $n = 0$
- $e = 0$; $n = -0.33$; *brachistochrone* solution

Depth h_2, m MSL

Cross-Shore Distance x_2, m

Figure 7. Equilibrium beach profile a) nomenclature, b) elliptic cycloid, c) Type-a cycloid solution (from Jenkins and Inman, 2006).

and Inman (2006) to both process-based algorithms and to empirically based parameters for which an extensive literature already exists. The elliptic cycloid solutions display wave height, period and grain size dependence and have demonstrated generally good predictive skill in point-by-point comparisons with measured profiles.

3.0) Model Initialization

Sand influx rates and maintenance dredging volumes are studied using numerical transport models that are run over an historic surrogate time period for which environmental forcing is well-known. The surrogate time period used in this model problem is 1981-2010. This period was chosen because of the simultaneous availability of a number of critical input data sets, in particular an unbroken wave record. In using wave data from this historic period as forcing functions to drive the transport simulations, a number of boundary conditions are adjusted in the model to evaluate the impact of removal of the South Beach Groin under potential future conditions, including large scale beach building in Oceanside and Carlsbad, and back-passing of Agua Hedionda dredge material.

In all such *boundary value problems* input variables are divided between two general classes, forcing functions and boundary conditions. The forcing functions include plant flow rates (Section 3.1), ocean water level variations (Section 3.2), and waves (Section 3.3). The important boundary conditions are lagoon bathymetry (Section 3.4), sediment grain size (Section 3.5), dredge disposal volumes (Table 1 and Appendix A), and watershed washload volumes (Section 3.6). The following provides an accounting of the input data assimilation and model initialization.

3.1 Power Plant Flow Rates: Plant flow rate data was provided in daily average increments by Cabrillo Power I LLC for the period 1999 -2010, and plotted in Figure 8. Flow rate data prior to 1999 was obtained from SDG&E. The merged data base from these two sources is plotted in Figure 8.

3.2 Ocean Water Level Data: The flow of water and sand into and out of the lagoon is driven by the time variation in ocean water level, and by the rate of cooling water consumption by the Encina power plant. Ocean water level variations for the period
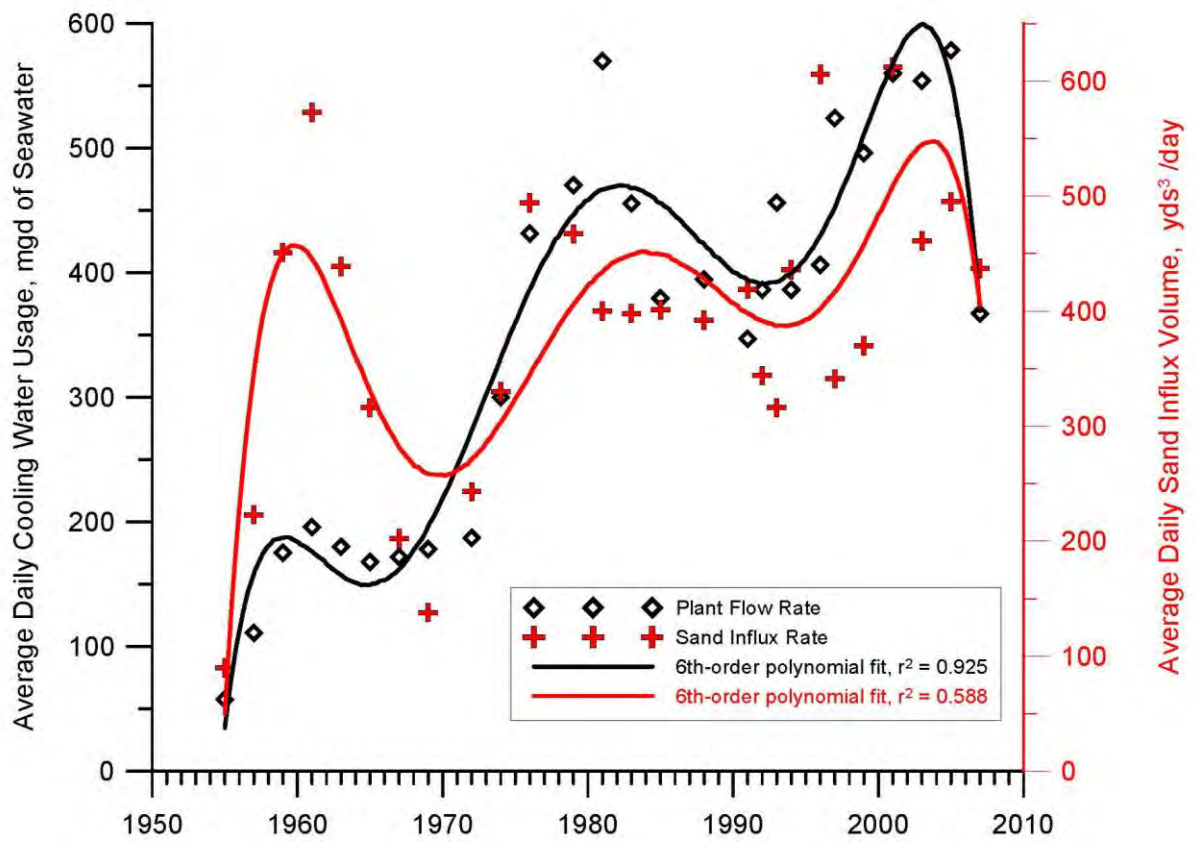
Figure 8: Time history of annual Encina cooling water usage (black) and average sand influx from maintenance dredging volumes (red). Data from SDG&E (1996) and NRG (2010).

beginning with RBSP construction and ending with the most resent lagoon soundings (6 April 2001- 30 September 2002) were obtained from the nearest ocean tide gage station to Agua Hedionda, located at Scripps Pier, La Jolla, CA. This tide gage (NOAA #941-0230) was last leveled using the 1983-2001 tidal epoch. Elevations of tidal datums referred to Mean Lower Low Water (MLLW), in **METERS** are as follows:

HIGHEST OBSERVED WATER LEVEL (11/13/1997)   = 2.332 m

MEAN HIGHER HIGH WATER (MHHW) = 1.624 m

MEAN HIGH WATER (MHW) = 1.402 m

MEAN TIDE LEVEL (MTL) = 0.839 m

MEAN SEA LEVEL (MSL) = 0.833 m

MEAN LOW WATER (MLW) = 0.276 m

NORTH AMERICAN VERTICAL DATUM-1988 (NAVD) = 0.058 m

NGVD29 = 0.700 m

MEAN LOWER LOW WATER (MLLW) = 0.000 m

LOWEST OBSERVED WATER LEVEL (12/17/1933) = -0.874 m

The use of observations of historic ocean water levels in hydraulic modeling exercises requires reconstruction of the water level time series at time steps much shorter than the observation intervals (6 minutes to 1 hour). Reconstruction of water level variations at 2 second time step intervals is necessary for achieving stable modeling simulations of the hydraulic response of the lagoon. The ocean water levels were reconstructed at 2 second time step intervals from astronomic tidal constituents for Scripps Pier using daily offsets to the astronomic tidal elevations to compensate for sea level anomalies (see Flick & Cayan,1984) and achieve agreement with the daily high and low water elevations measured by the Scripps Pier tide gage. These daily offsets were obtained by a minimization of the mean squared error between the predicted and measured water level. The short time step reconstruction from tidal constituents with daily offsets was accomplished with the TID_DAYS program in Jenkins and Wasyl (2005). The TIDE_FEM lagoon model was excited at the ocean inlet by 30 years of tides derived from tidal harmonic constituents for the Scripps Pier tide gage. These tides

provide an assessment of the maximum tidal range effects of the pre- and post-dredging bathymetry.

3.3 Wave Climate: Sediment budget reconstructions of sand of influx into Agua Hedionda Lagoon were computed from the measure waves for the period 1980-2010, although simulations end with the most resent lagoon dredging in 6 April 2007. Continuous unbroken wave records were obtained from the CDIP Oceanside, Dana Point, San Clemente, and Huntington Beach monitoring stations maintained by the Coastal Data Information Program, [CDIP, 2010, at http://cdip.ucsd.edu].

To correct these data from the offshore buoy mooring site to the nearshore of Agua Hedionda Lagoon, they are entered into a refraction/diffraction numerical code, back-refracted out into deep water to remove local refraction and island sheltering effects, and subsequently forward refracted into the immediate neighborhood of Agua Hedionda Lagoon. The backward and forward refractions of CDIP data were done using a numerical refraction-diffraction computer code called OCEANRDS. The primitive equations for this code are lengthy, but a listing of the codes for OCEANRDS Jenkins and Wasyl (2005). These codes calculate the simultaneous refraction and diffraction patterns propagating over a Cartesian depth grid. "OCEANRDS" uses the parabolic equation method (PEM), Radder (1979), applied to the mild-slope equation, Berkhoff (1972). To account for very wide-angle refraction and diffraction relative to the principle wave direction, "OCEANRDS" also incorporates the high order PEM Pade approximate corrections modified from those developed by Kirby (1986a-c). The Pade approximates in "OCEANRDS" are written in tesseral harmonics, per Jenkins & Inman (1985), in some instances improving resolution of diffraction patterns associated with steep, highly variable bathymetry such as found near the Carlsbad Submarine Canyon. These refinements allow calculation of the evolution and propagation of directional modes from a single incident wave direction; which is a distinct advantage over the more conventional directionally integrated ray methods which are prone to caustics (crossing wave rays) and other singularities in the solution domain where bathymetry varies rapidly over several wavelengths.

To perform both the backward and forward shoaling computations, the refraction/diffraction algorithm requires relatively fine-scale resolution of the bottom bathymetry, needing at least two grid points per wavelength of the highest frequency wave to be shoaled. Two detailed bathymetry grids were developed for the model: an outer to perform the backward/forward-refraction calculations from the CDIP monitoring sites out to deep water; the other a fine scale inner grid to forward refract those results into the Agua Hedionda nearshore. The outer grid consisted of 2405 rows of depth data and 4644 columns covering the entire Southern California Bight at 3 arc-second resolution. This bathymetry grid was extracted from an ARCGIS grid of merged bathymetry (NOS) and topography (USGS) data created by Dr. Mike Graham of Scripps Institution of Oceanography.

The boundaries of the inner grid correspond to the farfield control cell in Figure 3 and the depth data used to initialize this grid are taken from recent nearshore surveys by Dyson (2000 and 2001), and is described in detail in Section 2.1 of Jenkins and Wasyl, (2001).

An example of a reconstruction of the wave field throughout the Bight from the CDIP Oceanside buoy data is shown in Figures 9 for the largest wave event to have occurred during construction of the RBSP. Wave heights are contoured in meters according to the color bar scale and represent 6 hour averages, not an instantaneous snapshot of the sea surface elevation. Note how the sheltering effects of Catalina and San Clemente Islands have induced considerable variations in wave height offshore of Carlsbad (labeled **C** in Figure 9). The wave height and direction parameters inside the Channel Islands of Figure 9 are the values used as the deep water boundary conditions along the seaward face of the farfield control cell (Figure 8).

Figure 10 gives the local forward refraction calculation of the regional storm swells shown in Figure 9. Figure 10 gives wave height variations along an 18.5 km section of coastline in the farfield control cell of Figure 1, including wave shoaling in the Oceanside and Carlsbad beach nourishment sites around Agua Hedionda. These local refraction results are used to provide the point-to-point initializations for the sand transport calculations.
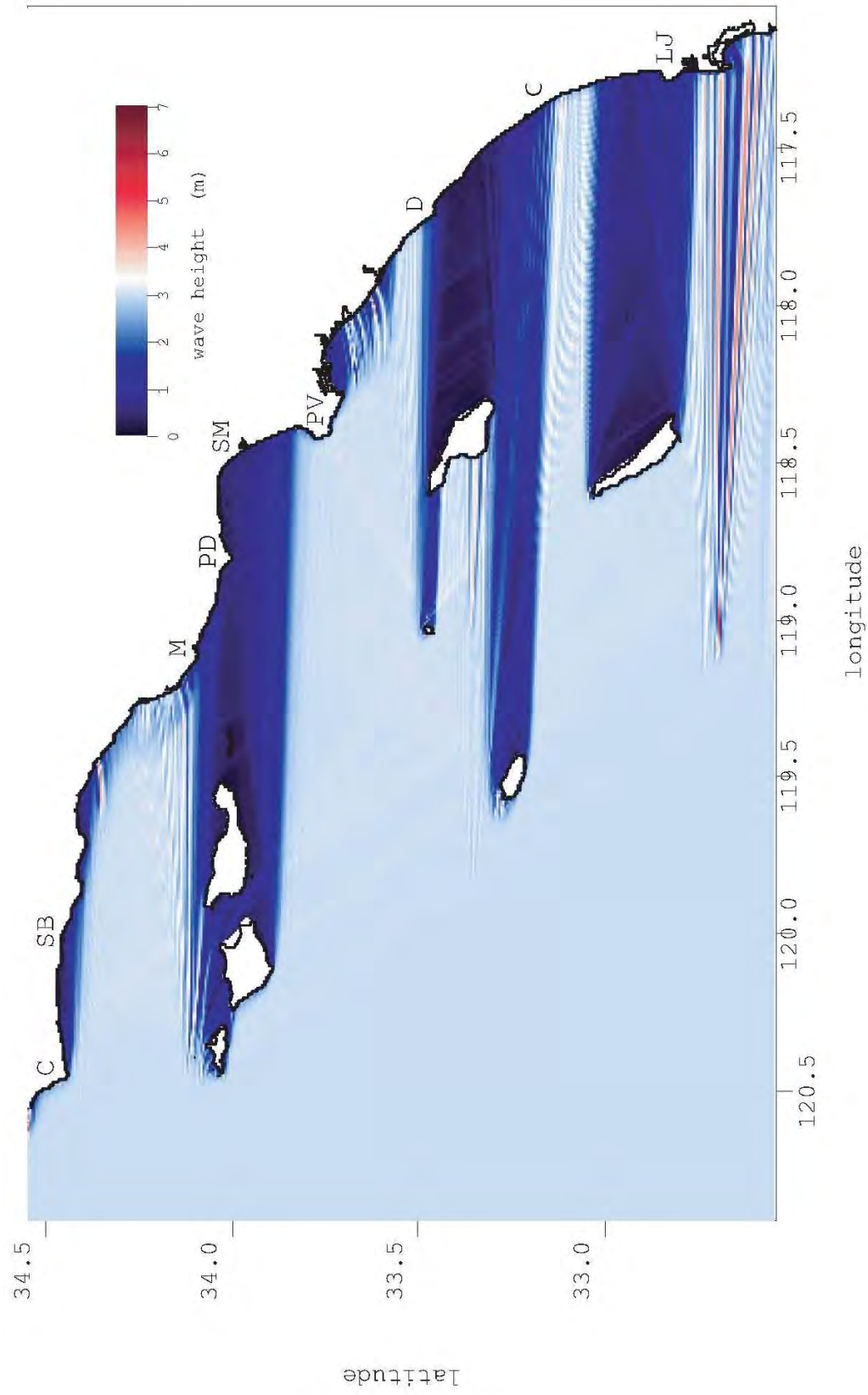
Figure 9. Back-refraction of Southern California Bight wave climate from the Oceanside CDIP buoy measurements (CDIP Station #45) for the storm of 21 April 2001, incident significant wave: H = 3.01 m, T = 9 sec, α = 272 degrees.
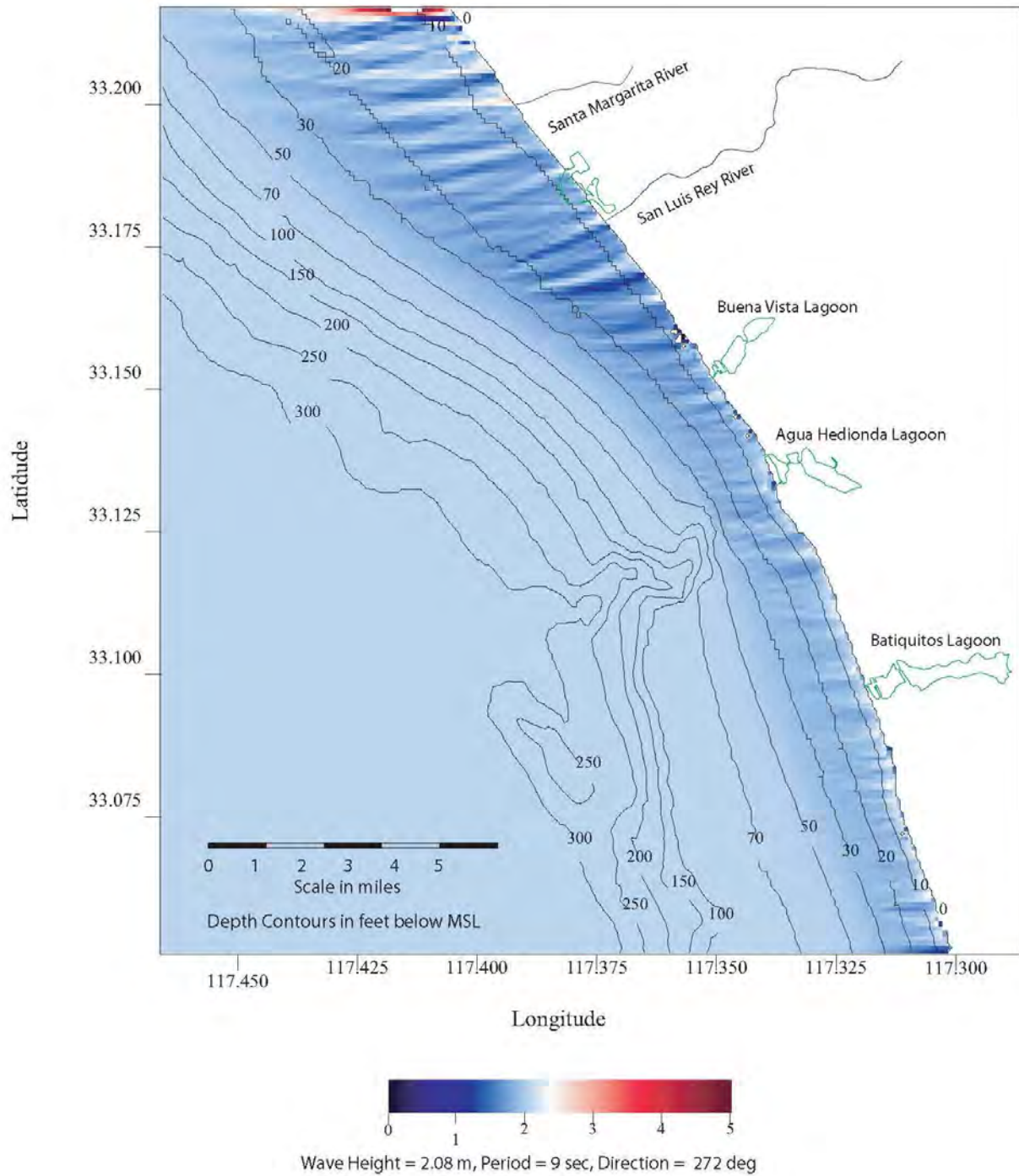
Figure 10. Local wave refraction/diffraction for 21 Apr 2001.

Regional and local shoaling patterns for the largest waves to occur in the post-construction period of the RBSP are shown in Figures 11 & 12, respectively. These waves were a bit more southerly than those in Figure 9 & 10, and the resulting change in island sheltering effects from this small direction change produced a substantial increase in the intensity of the "bright spot" in and around Carlsbad. Such episodes of bright spots during storm events are responsible for the episodic occurrence of high littoral sand transport rates and high lagoon sand influx rates.

Replication of the backward/forward refraction analysis on each of the 3 hour increments of the CDIP monitoring data produced continuous, unbroken records of the wave height, period and direction at each point in the farfield control cell (Figure 3) throughout the 1980-2010 period of record. An example of this continuous data set off the inlet to Agua Hedionda is shown in Figure 13. Comparison of this record with the power plant flow rate record in Figure 3 show that the periods of sustained high waves typically corresponded with the periods of below average plant flow rates. Moreover, the RBSP impact period was in general a time of relatively benign wave climate, wherein the average wave height of this period was only 0.88 meters as compared to an average wave height of 1.21 meters for the preceding 10 year period (see Jenkins & Wasyl, 2001). Data strings like those in Figure 13 were constructed for each alongshore point in the farfield control cell and used to drive the sediment budget calculations.

3.4 Lagoon Soundings, Bathymetric Mapping and Gridding: The most recent lagoon maintenance dredging was completed in April 2007 using differential GPS for precision ranging in conjunction with 40-200 KHz variable frequency fathometers. The 2007 survey did not provide bathymetric information above -2 ft MLLW; so consequently those data had to be merged with other survey data to obtain a complete picture of the lagoon over the entire tidal range. We began this merging exercise by building a bathymetric contour map from the 2007 survey data, obtaining bathymetric detail between -25 ft MLLW and – 2 ft MLLW. To fill in the upper sub-tidal and low-marsh intertidal regions, bathymetric contours from the April 1997 survey were stitched
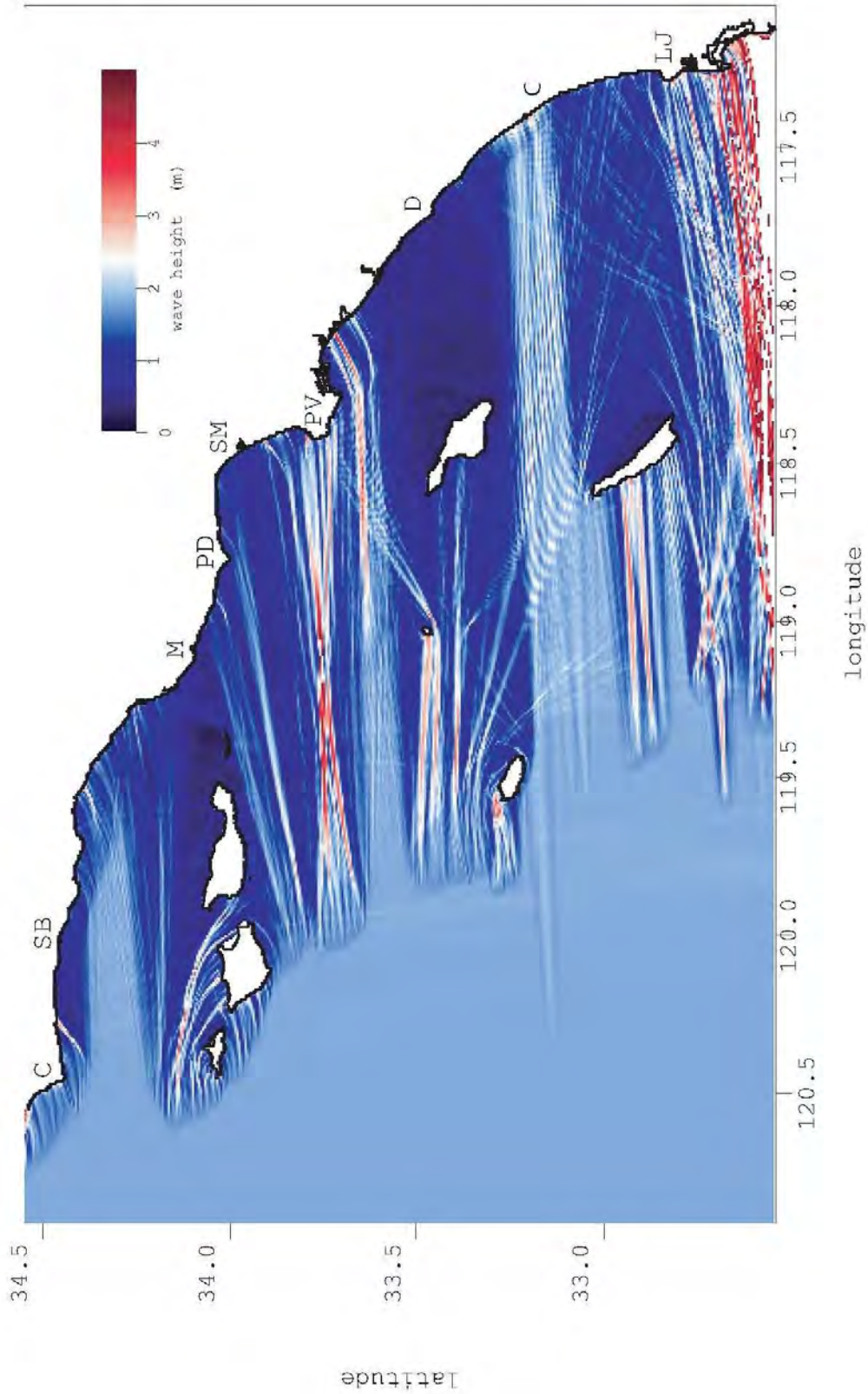
33

Figure 11. Back-refraction of Southern California Bight wave climate from the Oceanside CDIP buoy measurements (CDIP Station #45) for the storm of 8 January 2002, incident significant wave: H = 2.1 m, T = 18 sec, α = 263 degrees.
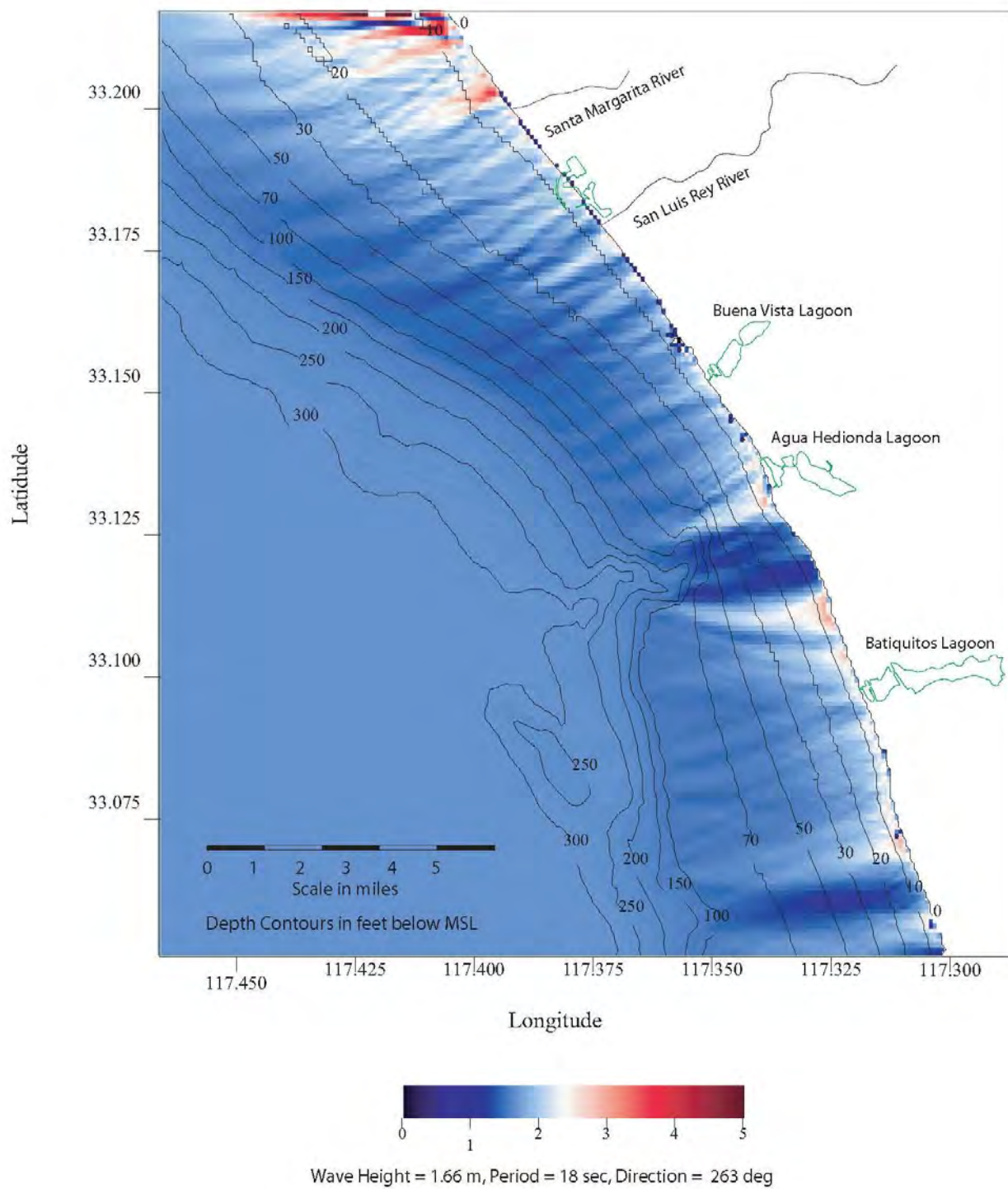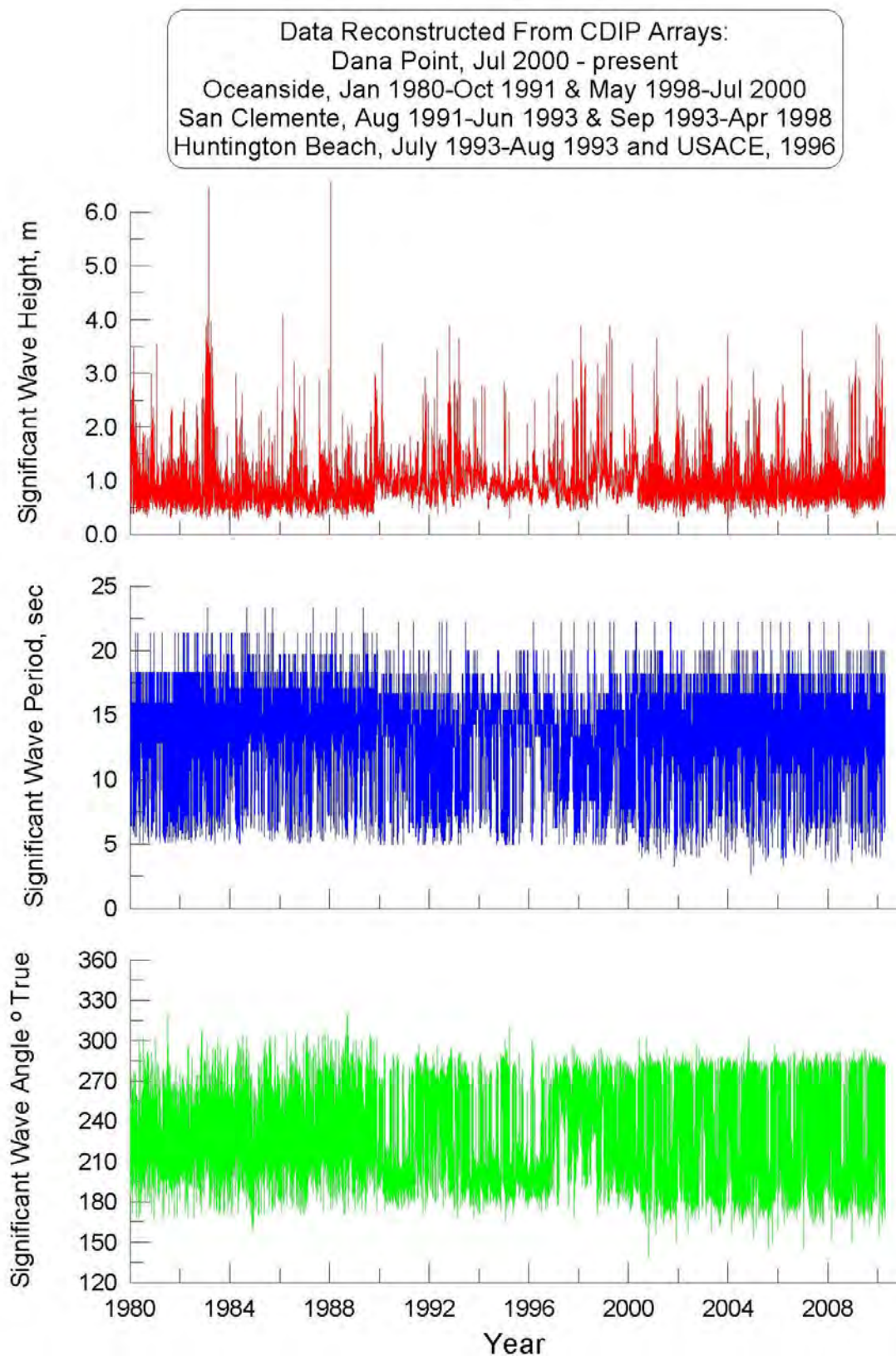
Wave Height = 1.66 m, Period = 18 sec, Direction = 263 deg

Figure 12. Local wave refraction/diffraction for 8 January 2002.

Data Reconstructed From CDIP Arrays:
Dana Point, Jul 2000 - present
Oceanside, Jan 1980-Oct 1991 & May 1998-Jul 2000
San Clemente, Aug 1991-Jun 1993 & Sep 1993-Apr 1998
Huntington Beach, July 1993-Aug 1993 and USACE, 1996

Figure 13. Wave climate reconstruction at Agua Hedionda Lagoon, 1980-2010

into the 2007 survey contours. The mid-marsh and high marsh contours were obtained from field surveys conducted by WRA for the City of Carlsbad that were overlaid on a 3D terrain map to determine the elevation of each point. There was some variation in the elevations of these points from different transects (due primarily to the limitations in accuracy of both the GPS data and the original 1' contours). To compensate for this and to determine the appropriate MHW elevation for the lagoon, WRA took the mean elevation of all of the MHW points. WRA repeated this averaging procedure to create the 0.5 ft, 1 ft, 1.5 ft and 2 ft above MHW contour lines. While this procedure worked quite well throughout much of the lagoon, when creating a 3D model of the terrain in very flat (or topographically complex) portions of the lagoon the software encountered data gaps that resulted in fairly erroneous topographic data in these areas. This could not be avoided when using 1 ft contours. There were relatively few regions of error, and based on fairly straightforward vegetative signatures on the aerials; and using this vegetation data, WRA was able to manually correct the topography.

Upon completion of vetting the topographic data using vegetation types for co-registration, the six mid and high marsh contours between + 2 ft MLLW and extreme high water at + 7.7 ft MLLW were stitched into the master bathymetric file for Agua Hedionda Lagoon, producing the bathymetric map shown in Figure 14. The bathymetrically most dynamic part of the lagoon is the *recharge zone* in the West Basin, generally comprised of the zone indicated by the ⊗ symbols in Figure 15. The recharge zone is the section of the lagoon where the preponderance of in-fluxed sand accumulates as a flood tide bar following dredging. For time-stepped hydrodynamic simulations, the recharge zone was also initialized for bar morphologies from additional condition surveys taken in October 2002 (Figure 15), and November 2004. ArcGIS software is used to calculate the volume of newly accumulated sediment in the recharge zone during time-stepped hydrodynamic simulation based on the point-to-point incremental change in bottom elevation relative to the post-dredging soundings (the April 2007 survey shown in Figure 14). From physical volume in the recharge zone immediately after dredging, it is calculated that 779,962 cubic yards of dry bulk sand are required to completely fill the recharge zone (referred to as the carrying capacity). Probability of *incipient inlet closure*
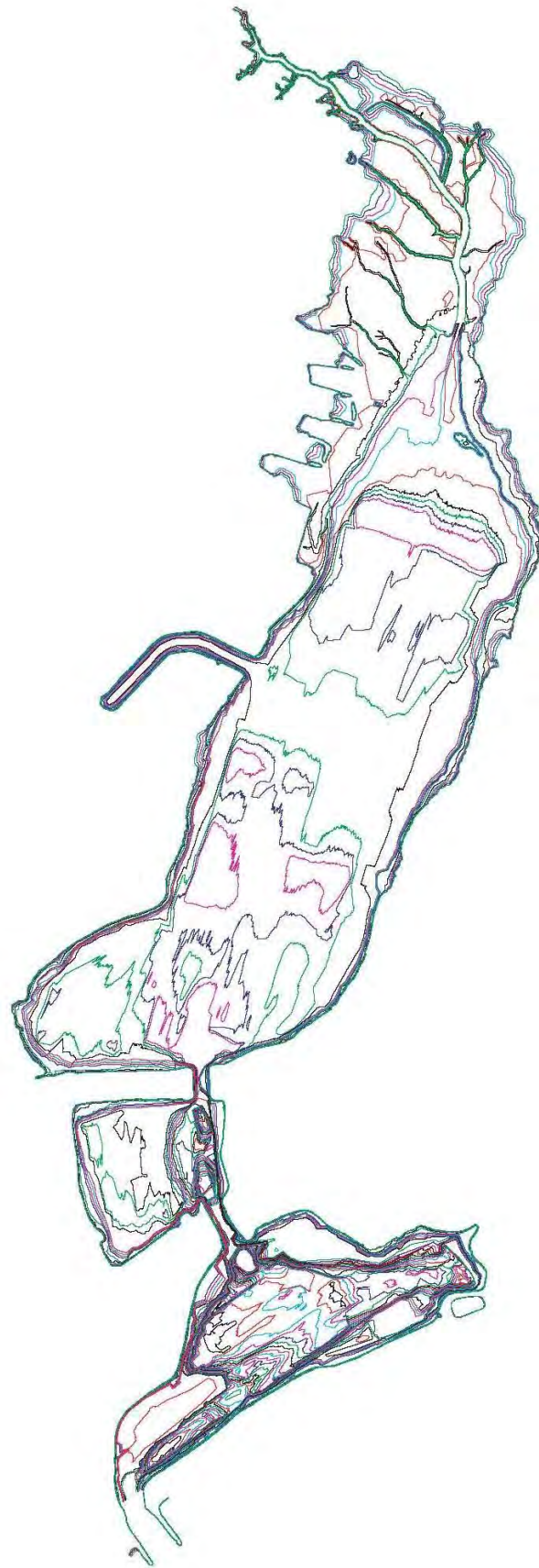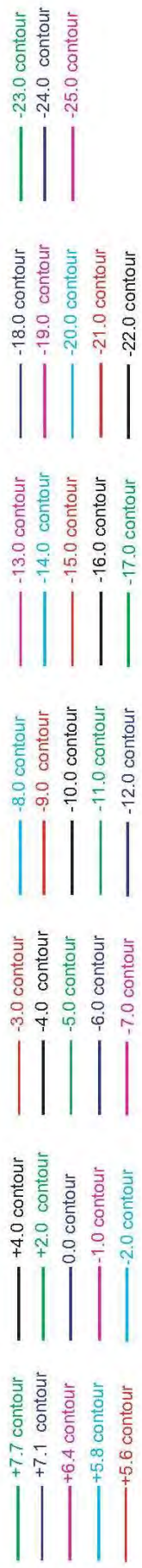
Figure 14. Agua Hedionda bathymetry in ft. MLLW, based on 2007 survey for -25 ft thru -2 ft; 1997 survey for -2.0 thru +2 ft; and on the WRA 2010 topographic survey for +2.0 thru +7.7.
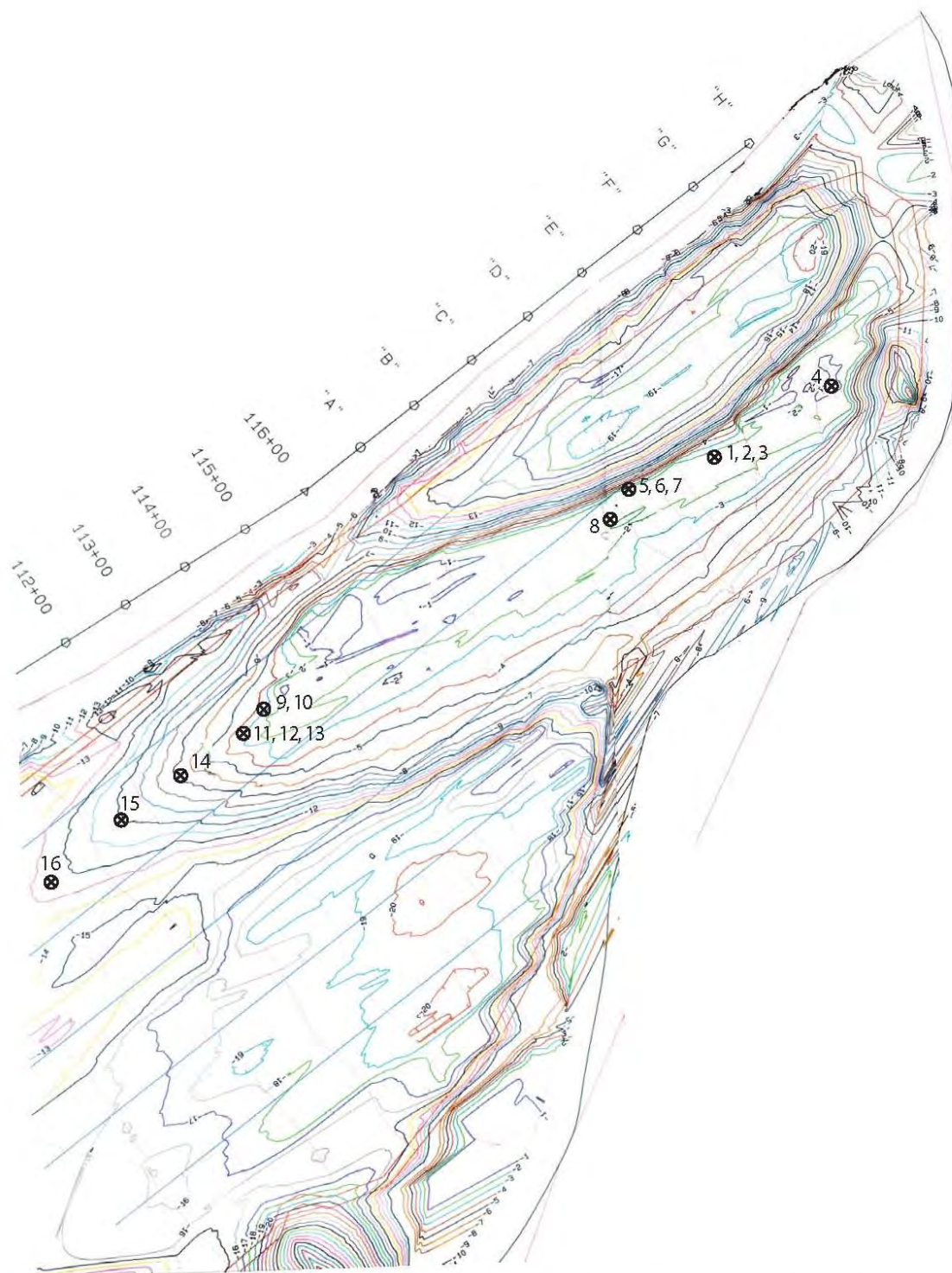
Figure 15. West Basin condition survey 12 October 2002 with locations of sediment sampling.

is thus calculated in terms of the percentage of carrying capacity that is filled by sand influx at any given time.

To quantify hydrodynamic influence of the tidal jet at the inlet to Agua Hedionda Lagoon (associated with protracted periods of reduced flow operations with a partially shoaled inlet), we perform tidal hydraulic simulations using the lagoon bathymetry from Figure 14. The TIDE_FEM tidal hydraulics model presented in Jenkins and Inman (1999) was gridded for a computational mesh of Agua Hedionda Lagoon as shown in Figure 16, using pre- and post-dredging West Basin bathymetry from 2002-03, 2004-05, 2006-07. The pre-dredging bathymetry featured an inlet bar in the West Basin typical of that mapped during the October 2002 condition sounding shown in Figure 15. The post-dredging surveys indicated uniform deep water throughout the west basin with depths ranging from -20 ft MLLW to – 25ft MLLW, similar to that found in Figure 2-2 of Elwany, et al (2005).

Of particular interest to the finite element mesh in Figure 16 are the *hydraulic friction slope coefficients, S_{fj}*, providing tidal muting effects. Two separate formulations are used. One is given for the 3-node triangular elements situated in the interior of the mesh in Figure 16 which do not experience successive wetting and drying during each tide cycle. The other formulation is for the elements situated along the wet and dry boundaries of the lagoon. These have been formulated as 3-node triangular elements with one curved side based upon the cubic-spline matrices developed by Weiyan (1992). These two sets of elements were assembled into a computational mesh of the lagoon conforming to the lagoon extreme high waterline in Figure 16. The wet-dry boundary coordinates of the curved waterline, (x', y'), are linearly interpolated for any given water elevation from the contours stored in the lagoon bathymetry file based on the updated lagoon bathymetry following each maintenance dredge cycle.

Aside from gridding the TIDE_FEM tidal model, the bathymetry in Figure 14 has another important hydraulics aspect, namely the storage capacity of the lagoon for seawater. Figure 17 presents the storage rating function derived from the bathymetry in Figure 14. The 2007 post-dredging survey indicates the lagoon stores 1,500 acre ft of
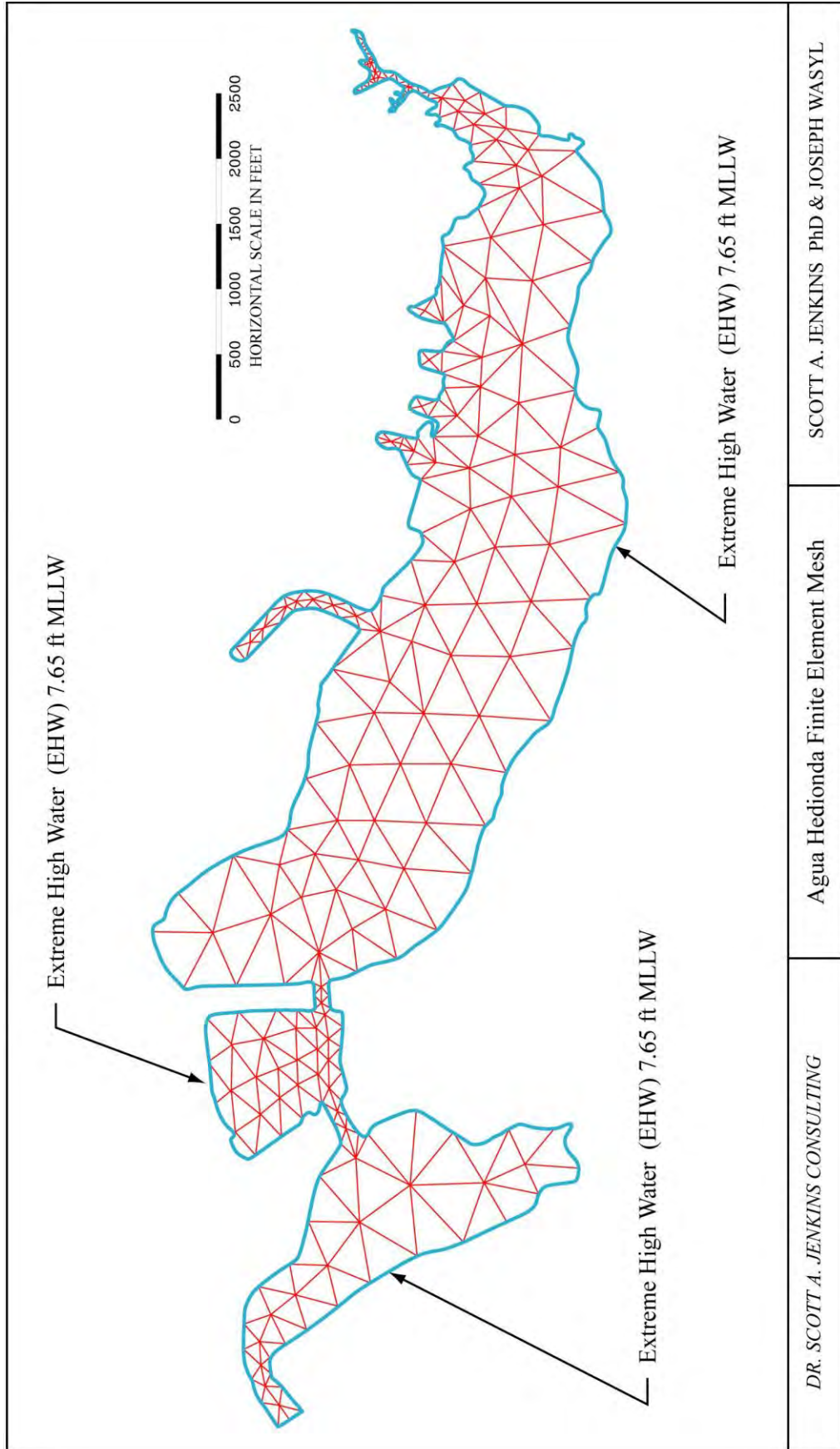
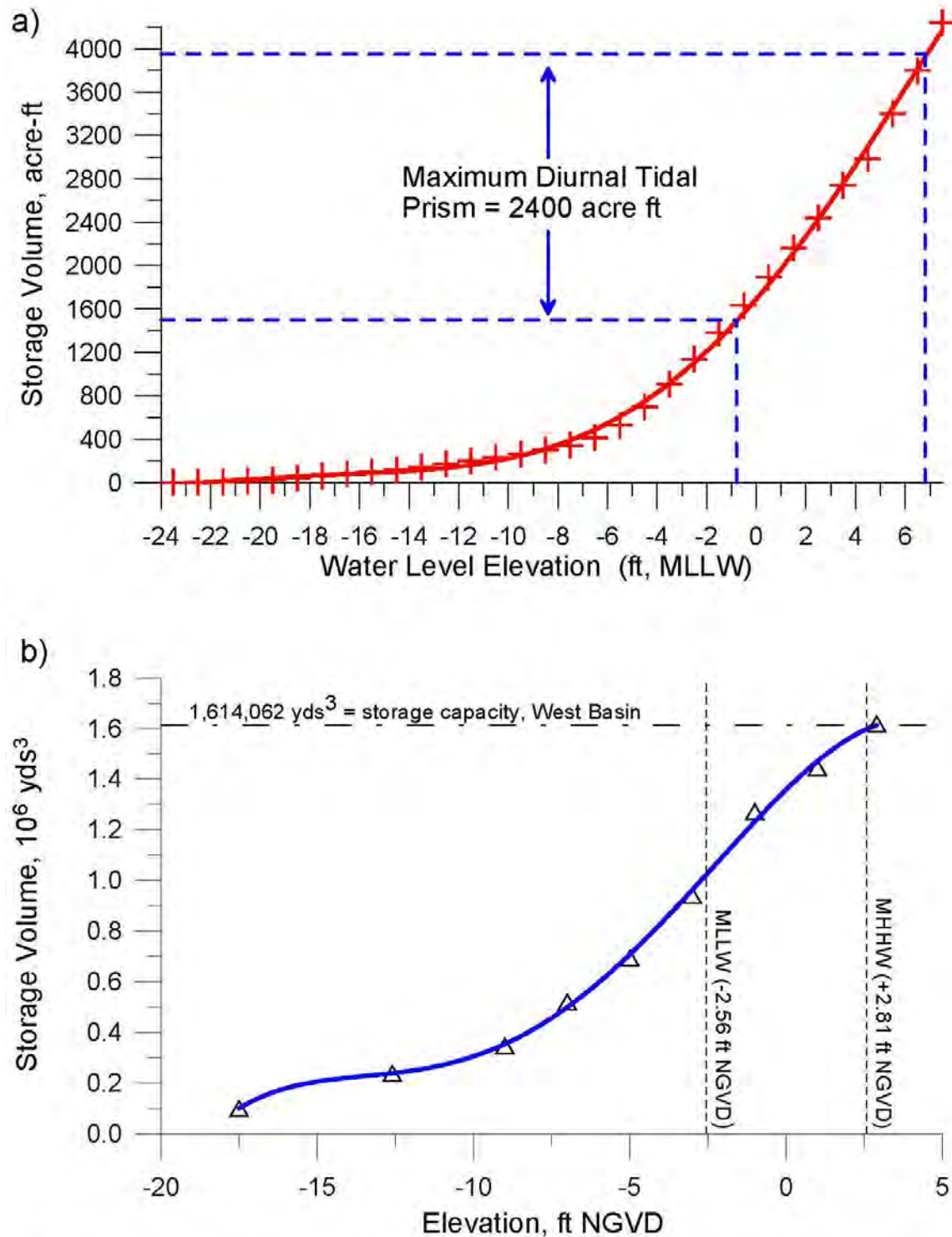Figure 16. Computational mesh for TIDE_FEM tidal hydraulics model of Agua Hedionda Lagoon.

Figure 17. a) Storage rating function for Agua Hedionda Lagoon, based on 2007 sounding. Maximum and minimum water levels for existing conditions from Elwany et al, 2008; b) Storage rating curve: West Basin of Agua Hedionda Lagoon.

sub-tidal water volume and has a maximum tidal prism during spring tides of 2,400 acre ft. These volumes are based on higher-high and lower-low water levels in the lagoon measured by Elwany, et al, (2005).

3.5 Sediment Grain Size Distributions: The bathymetry of the lagoon is comprised of predominantly fine sand which is mobile once the tidal flow exceeds the threshold shear stress of a particular grain size. To account for these grain size dependent motions in the hydrodynamic model, grain size data is required. Figure 15 shows the location of 16 sediment cores collected 12 October 2002 on the flood tide bar formed in the West Basin of Agua Hedionda following the antecedent lagoon maintenance dredging on 18 April 2001. Cores were collected in two separate groups in clusters of 8 cores dispersed between the outer portion of the bar and the inner portion. This was done to determine if there was any significant shear sorting of the influxed sands as the tidal flow diverged and decelerated into the West Basin. Each core was collected by a diver operated coring tool that recovered a 2.2cm diameter, 46 cm depth core from sedimentary bed. The tool and its design, construction and operation are described in Inman, et al (1979 and 1981). Where three separate cores are indicated in Figure 15 at a given core site, a side slope of the sand bar was sampled at its crest, mid-slope and toe locations. In addition, 12 core samples were collected, 6 each from the North Beach and Middle Beach receiver sites (see Figure 1). These beach cores were collected at the MHT, MSL and MLLW elevations (see Section 3.2 for MHT, MSL and MLLW elevation datums).

Each of the cores was segmented into equal quarters that were independently washed in distilled water to remove salts; then dried for 24 hours at 60°C, mixed with a rubber pestle and then split with a Jones-type splitter to recover a 25 gram increment of that quarter. The 25 gram increments of each quarter were combined to produce a representative 100 gram composite sample of that core to be subjected to grain size analysis. The grain size distribution was obtained by shaking the composite core samples through a nest of sieves for 30 minutes with a Porter Sand Shaker (Braun Corp. Model #57400). The sieves ranged in size from 32 mm ($-5.0\,\phi$) through 0.044 mm ($4.5\,\phi$) at $0.5\,\phi$ intervals. The mass fractions recovered by each sieve in the stack were then

weighed on a Mettler (#PB300) analytical scale (precision ±0.01 grams). The mass fractions for each sieve were computed as a percent of the total mass.

Grain Size Distributions of the 8 composite cores collected on the outer portion of the flood tide bar are plotted in Figure 18 and on the inner portion in Figure 19 in the percent finer format. For comparison the historic mean ranges of the native beach sand sizes are plotted as vertical dashed lines from Inman, et al (1954, 1966 1972 and 1991) and Leighton & Associates (1988, 1995). These dashed vertical lines correspond to the median grain size (50% cumulative percent finer in red, D_{50}) and the finer and coarser sorting limits of the native beach sand (16% , D_{16}, and the 84% ,D_{84}, cumulative percent finer in black, respectively). The median grain size of the newly deposited sediments varies between 130 and 204 microns among the cores taken on the outer portion of the flood tide bar and between 120 and 210 microns on the inner portion. The spread in the distributions is nearly identical on inner and outer bar sections and the median grain sizes in both the upper and lower limits of that spread is well below the median beach grain size of 290 microns. The variation in grain size distributions within the lagoon bar deposits correlated with elevation on the bar rather than with distance along the length of the bar. The finest distributions were found at the toe and mid-slope sections of the inlet bar and the coarsest were found at the crest. Therefore, shear sorting did apparently occur, but was controlled by the velocity contrasts between deep and shallow water. Higher velocities over the shallow water sections of the bar crest selectively sorted the coarser fractions from the fines while the finer fractions were sorted away from the high stress regions and towards the lower velocity regions in the deeper water at the toe of the bar.

3.6 Discharges into Lagoon from Agua Hedionda Creek: Agua Hedionda Lagoon is a salt water environment populated by salt water tolerant species. The watershed draining to Agua Hedionda Lagoon consists of 18,800 acres upstream from the lagoon, which drains to the lagoon principally via the Agua Hedionda Creek, (Figure 20). The physical data show that this watershed is too small for runoff from it to significantly alter the predominantly salt water environment of Agua Hedionda Lagoon, even during
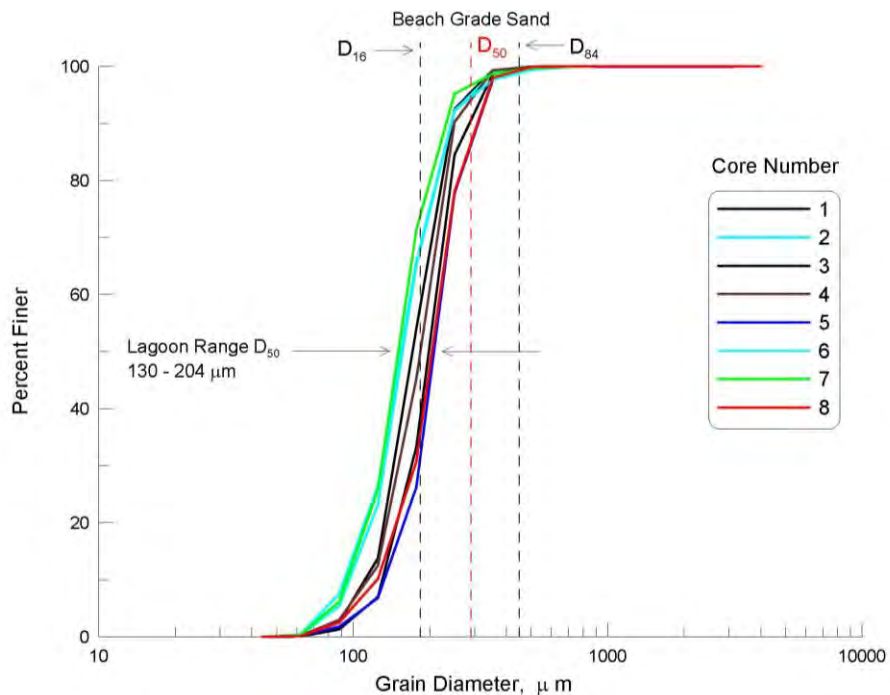
Figure 18. Grain size distribution of samples taken at the outer end of outer lagoon, October, 2002.
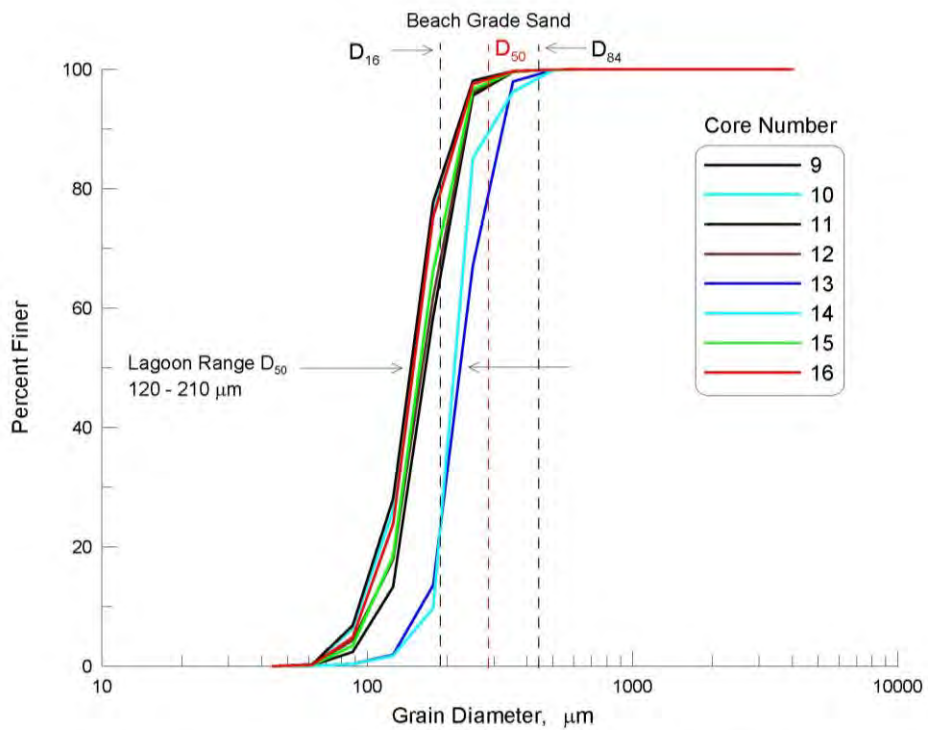

Figure 19. Grain size distribution of samples at the inner end of outer lagoon, October, 2002.

the wettest year on record, from June 2004 to June 2005. Yearly rainfall totals in the Agua Hedionda Creek watershed average 15.6 inches while 19.19 inches of rain fell during the water year, June 2004 to June 2005. We use this period to estimate the maximum probable effects on the lagoon from discharges from Agua Hedionda Creek.

Tetra Tech (2007) prepared a comprehensive report on the Agua Hedionda Watershed water quality for the City of Vista, and Table 3 and Figure 7 of that report provide flow rate measurements for Agua Hedionda Creek for 2005-2007. Unfortunately, Tetra Tech (2007) provides no flow rate data during the first half of 2004, and there were some heavy rainfall events occurring in October 2004. The missing flow rate data can be estimated from rainfall data by establishing a quantitative relationship (hydrographic rating function) between rainfall and creek discharge using the body of data that does exist for 2005-2007. Figure 21a compares the Tetra Tech (2007) daily discharge rates for Agua Hedionda Creek (shown as black crosses) against the daily rainfall (red bars) measured by NOAA/NCDC rain gage #03177 at Carlsbad Airport (cf. NWS, 2009). Note each rainfall event produces a corresponding peak discharge event in the creek, except during a portion of the winter of 2006 when no flow data was collected. Figure 21b indicates that the relation between rainfall and creek discharge rate can be expressed as a second order polynomial (hydrographic rating curve) having a coefficient of determination, R-squared = 0.80, (indicating a reasonably good fit). The polynomial can then be applied to the rainfall during 2004 to fill in the missing creek discharge data. Here, the creek discharge calculated from the hydrographic rating curve (red) tends to over-estimate measured creek discharge rates (black), and consequently errs on the side of caution with respect to not underestimating storm water impacts on the lagoon water quality.

Now, consider how the storm water discharge from Figure 21 is diluted in the volume of sea water in the lagoon. The lagoon exchanges an average of 1,700 acre ft. of seawater with the ocean through tidal flushing (based on mean tidal range in the lagoon) and stores an average of 3,450 acre ft. of seawater, (cf. Figure 17.). Because of tidal flushing, storm water would remain in the lagoon for only 2.6 days, based on the residence time of the lagoon water mass as determined by Elwany, (2005) and Jenkins and Wasyl, (2006) using two independent methods. Applying these dilution volumes and
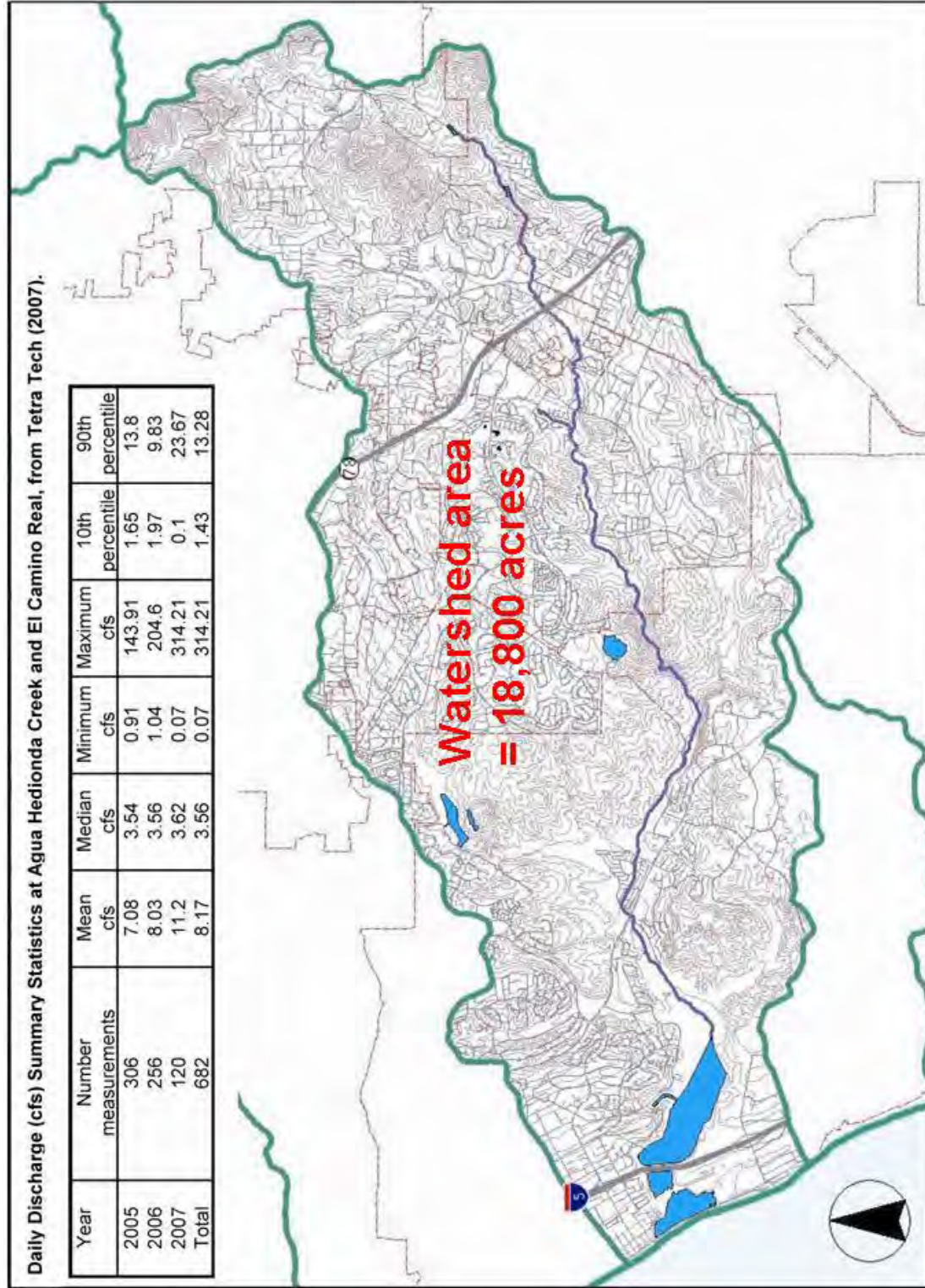
Daily Discharge (cfs) Summary Statistics at Agua Hedionda Creek and El Camino Real, from Tetra Tech (2007).

Year	Number measurements	Mean cfs	Median cfs	Minimum cfs	Maximum cfs	10th percentile	90th percentile
2005	306	7.08	3.54	0.91	143.91	1.65	13.8
2006	256	8.03	3.56	1.04	204.6	1.97	9.83
2007	120	11.2	3.62	0.07	314.21	0.1	23.67
Total	682	8.17	3.56	0.07	314.21	1.43	13.28

Watershed area = 18,800 acres

Figure 20. Flow statistics of Agua Hedionda Creek Watershed, 2005-2007.
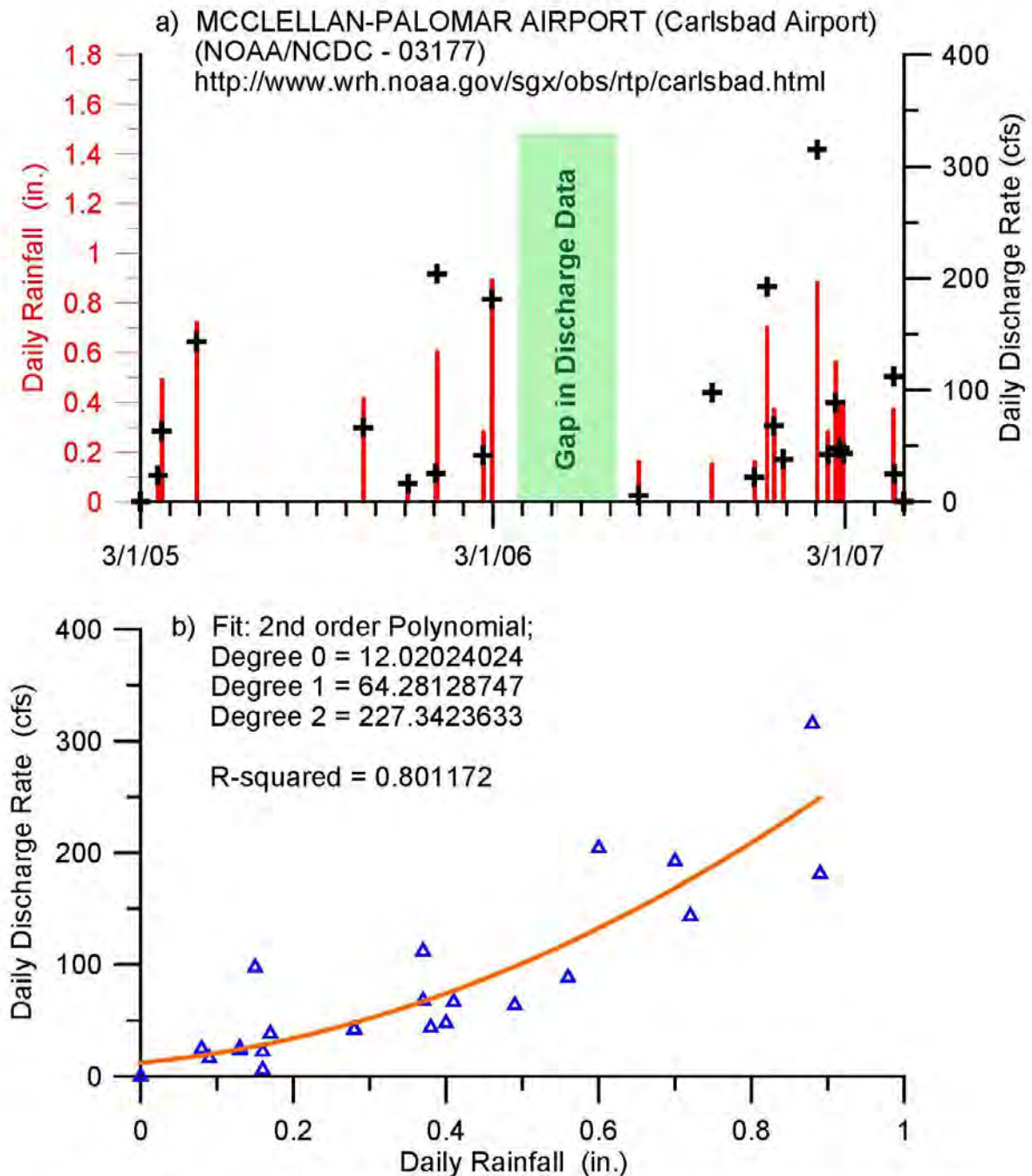
Figure 21. Relation between rainfall and discharge rate of Agua Hedionda Creek: a) Rainfall (red bars) & daily discharge Agua Hedionda Cr. (black crosses from Tetra Tech, 2007). b) Hydrographic rating curve (red) from 2nd order polynomial fit to flow rate vs rainfall data (blue diamonds).

residence times to the creek discharges in Figure 21 results in a time series of lagoon salinity throughout the wettest period on record shown in Figure 22. The predicted lagoon salinity in red compares closely with unpublished near-surface salinity measurements (Tenera Environmental, 2009) shown as blue triangles. The lowest predicted salinity (red) in Figure 22 is 20.4 ppt and the lowest measured salinity (blue) is 20.1 ppt. However the red curve predicts a number of other events of salinity depression in the lagoon when salinity measurements were not taken. Regardless, a histogram analysis in Figure 23 of the salinity variation in Figure 22 indicates that 95 % of the time, lagoon salinity exceeded 32 ppt throughout the 1 June 2004-31 May 2005 monitoring period, while average ocean salinity is 33.52 ppt (Jenkins and Wasyl, 2001, 2006). From this, we conclude that rainfall events during 2004-2005 were neither intense enough nor persistent enough to significantly alter the predominantly salt water environment of Agua Hedionda Lagoon.

Storm water discharge from Agua Hedionda Creek transports primarily washload into the lagoon from erosion of the unhardened surfaces of the watershed (cf. Figure 20). Using the streamflow estimates from Figure 21, we can invoke the surrogate methodology of Inman and Jenkins (1999) to construct a sediment rating curve that predicts the sediment flux into the lagoon from Agua Hedionda Creek during rainfall events. This procedure results in the quadratic dependence of washload sediment flux on streamflow plotted as the red line in Figure 24. This quadratic relation has a coefficient of determination of 0.788 and is used in the SEDXPORT model to specify sediment flux into the East Basin of lagoon from Agua Hedionda Creek in response to rainfall. This sediment flux is silt and clay sized sediment as contrasted with the fine sand that is deposited in the recharge zone of the West Basin from the ocean inlet (cf. Figures 18 & 19). The washload sediment flux into the East Basin begins to flocculate when encountering the salinity plotted in Figure 22. While this accelerates the setting rates of these washload sediments, the lagoon is well flushed and only a relatively small fraction settles in the lagoon. Moreover, the magnitude of the washload flux is minor in comparison to the daily influxes of littoral sediment (cf. Figure 7). None the less, these fine-grained sediment dynamics are accounted by the algorithms of the SEDXPORT model that is calibrated in the Section 2.2.8.
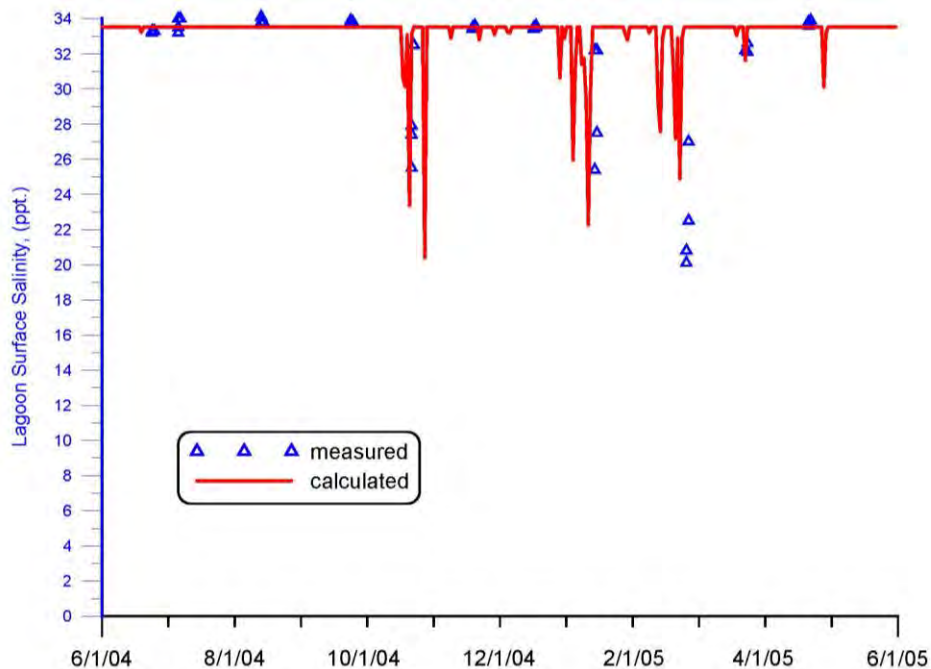
Figure 22: Salinity in Agua Hedionda Lagoon during wettest period on record: 1 June 04- 1 June 05.
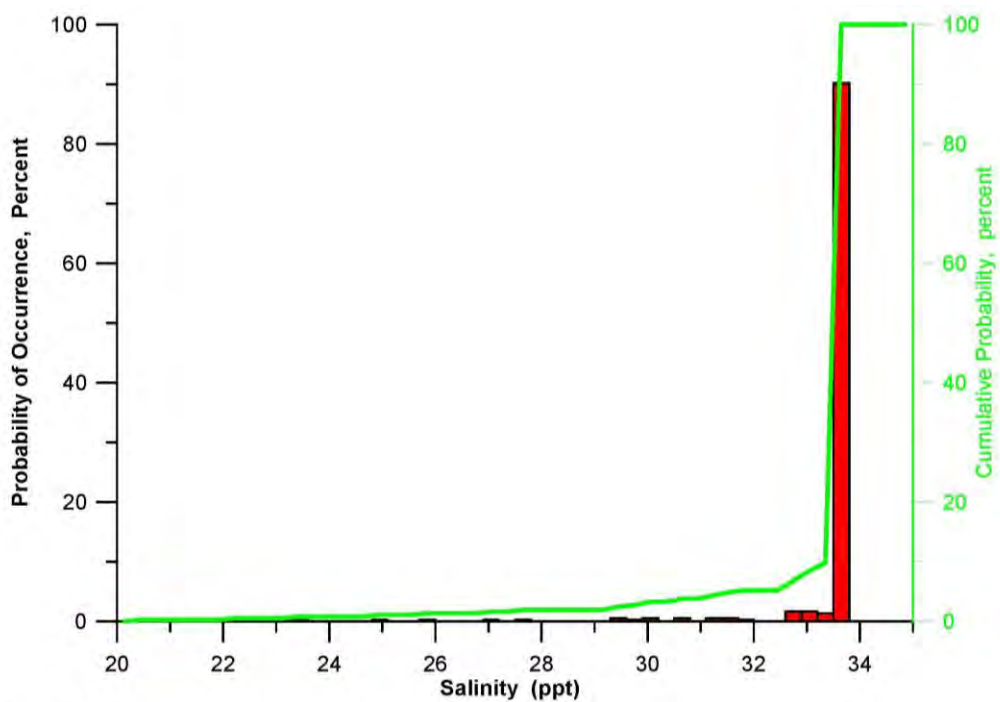

Figure 23. Histogram of salinity in Agua Hedionda Lagoon during wettest period on record, 1 June 2004 - 31 May 2005. Probabilities of occurrence based on the red curve in Figure 22.
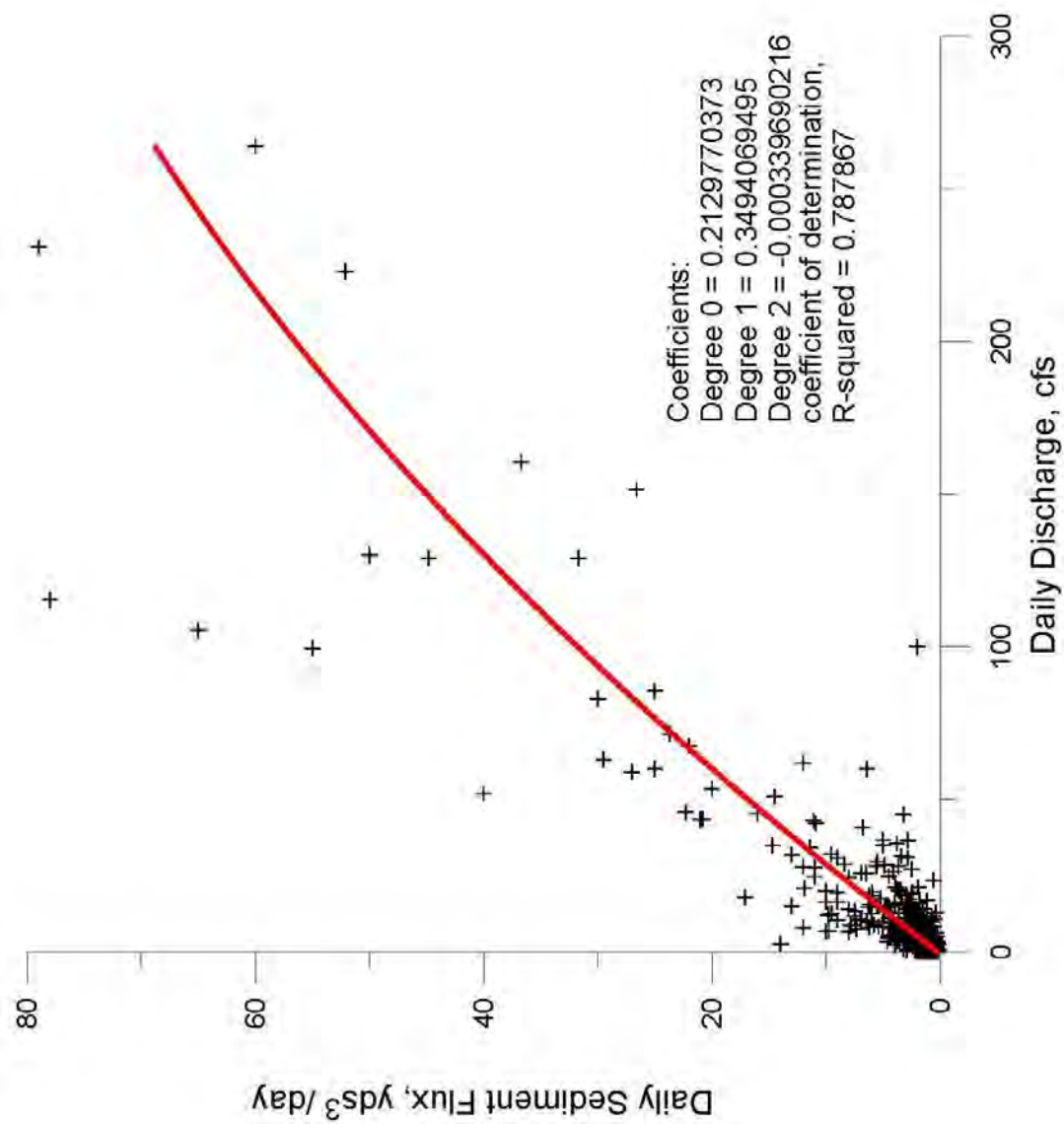
Figure 24 Sediment Rating Curve for Agua Hedionda Creek, after Inman and Jenkins (1999)

Coefficients:
Degree 0 = 0.2129770373
Degree 1 = 0.3494069495
Degree 2 = -0.000339690216
coefficient of determination,
R-squared = 0.787867

Daily Discharge, cfs

Daily Sediment Flux, yds3 /day

3.7 Calibration of the Tidal Hydraulics Model: Spring, neap and mean tidal range simulations of the hydraulics of Agua Hedionda Lagoon were performed using astronomic tidal forcing functions at = 2 sec time step intervals for the period 1980-2007, as discussed in Section 3.2 . Computed water surface elevations and depth averaged velocities from the global solution matrix were converted to lagoon waterline contours and flow trajectories. Calibrations for determining the appropriate Manning factors and eddy viscosities were performed by running the TIDE_FEM model on the Figure 14 bathymetry file and comparing calculated water surface elevations in the East Basin and inlet channel velocities against measurements by Elwany et al. (2005) during a complete spring-neap cycle of 13 -30 June 2005. Plant flow rates during this lagoon monitoring period were input to TIDE_FEM according to Figure 8, daily recordings by Cabrillo LLC. Iterative selection of Manning factor n_0 = 0.03011 and an eddy viscosity of ε = 6.929 ft^2/sec gave calculations of water surface elevation and inlet channel velocities that reproduced the measured values to within 2% over the 18 day spring-neap monitoring cycle.

Figure 25 gives the flow trajectories and depth averaged tidal currents computed by the calibrated TIDE_FEM model during spring flooding tides on 21 June 2005 of the monitoring period from Elwany et al (2005). The model was initialized with a plant flow rate of 501.1 mgd as reported by Cabrillo Power LLC in Figure 3. This flow rate is roughly equivalent to the long-term mean in Figure 3. Maximum currents in the inlet channel reached 1.5 m/sec or 4.9 ft/sec. Flood tide currents in the West Basin form a well defined jet along the north bank at speeds of between 0.9 m/s (2.9 ft/sec) to 1.2 m/sec (3.9 ft/sec), sufficient to scour and transport fine sand in the 120-210 micron size regime (cf. Figures 18 & 19). A sluggish eddy persists in the central portion of the West Basin while the middle portion of the recharge zone is near stagnation, ideal conditions for fine sand to settle in deep water post dredging bathymetry. A feeder current of about -0.4 m/sec (-1.3 ft/sec) spins off the southeast flank of the West Basin eddy, and flows toward the plant intake, thereby supplying feed water at a rate of 501 mgd to the plant. The flood tide jet along the north bank of the West Basin speeds back up to as high as 1.5 m/sec (4.9 ft/sec) as it passes through the hardened channel under the rail road bridge
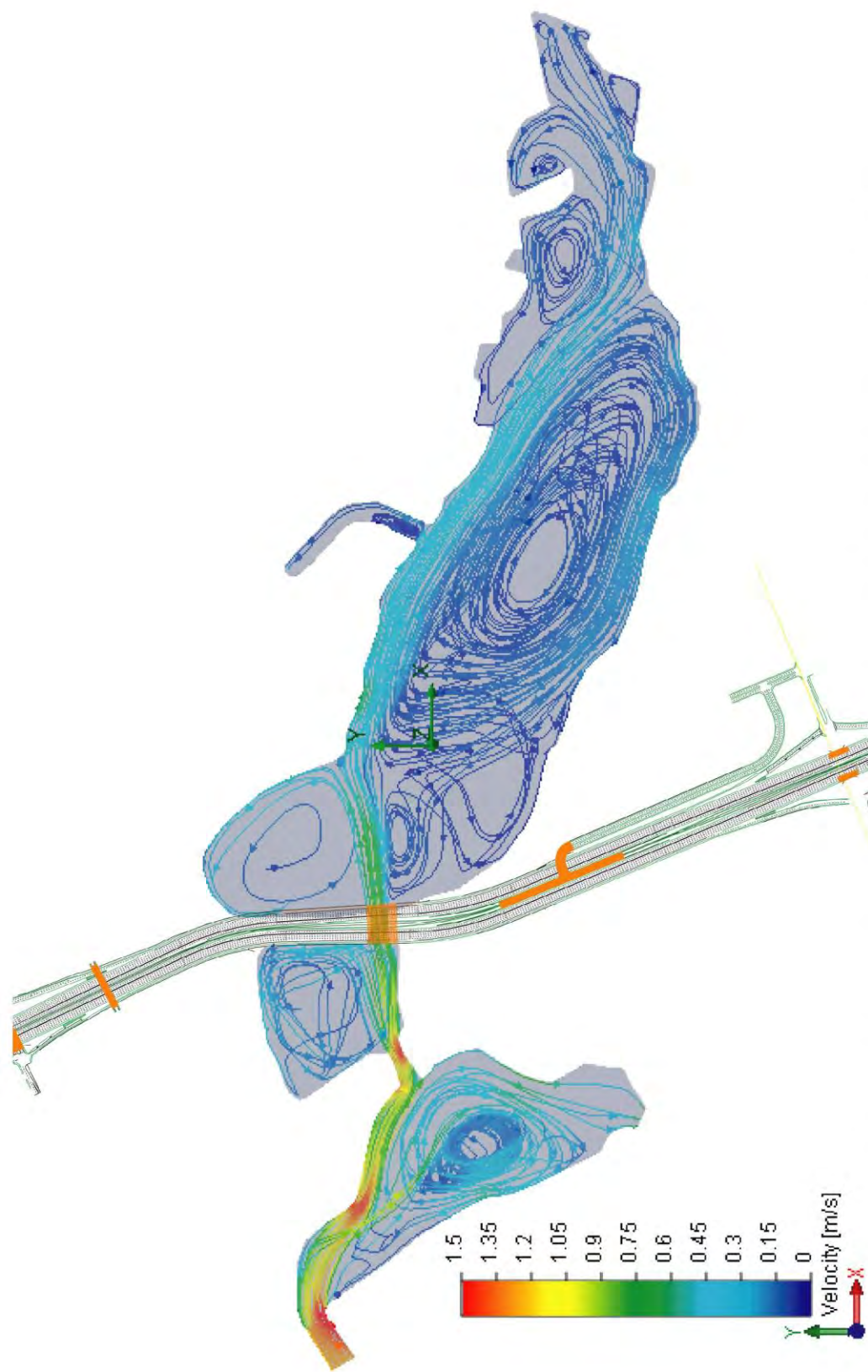
Figure 25. Hydrodynamic simulation of tidal flow into Agua Hedionda Lagoon during spring flooding tides.

and then losses energy as it diverges into the Central Basin, spinning up a somewhat disorganized Central Basin eddy. The core of the Central Basin eddy is at stagnation, again providing ideal conditions for suspended sediment to settle and deposit. Consequently a bar forms here that was removed during the 1997-98 inner basin restoration dredging performed by SDG&E (Jenkins and Wasyl, 1998). Spring flood tide currents speed back up to 0.8-0.9 m/sec (2.6-2.9 ft/sec) through the hardened channel under the I-5 bridge before diverging into a complex set of counter rotating eddies that populate the East Basin. East Basin eddy speeds are on the order of 0.1 m/sec (0.3 ft/sec), insufficient to transport fine sand but an important stirring mechanism for mixing the East Basin water mass to maintain high oxygen levels and to maintain silt and clay sized sediment particles in suspension.

Figure 26 plots the TIDE_FEM simulation of ebbing spring tidal flows in the lagoon on 21 June 2005. The wetted area of the lagoon is significantly reduced relative to the flood tide area in Figure 25, due to the lower water levels acting on the storage rating curve in Figure 17. A creeping flow with complex structure on the order of -0.1 m/sec (-0.3 ft/sec) evacuates the east basin and accelerates to -0.8 m/sec (-2.6 ft/sec) as it passes through the hardened channel under the I-5 bridge. A vigorous well-ordered Central Basin eddy is spun up by an ebb-tide jet flowing along the southern bank of the Central Basin. This jet accelerates to -2m/sec (-6.6 ft/sec) as it passes through the hardened channel under the rail road bridge; and then splits into a south branch current and a north branch current as it diverges into the West Basin. The south branch current flows along the west bank of the West Basin and feeds the power plant source water at a rate of about -0.6 m/sec (-2.0 ft/sec). The north branch current also flows along the west bank of the West Basin and exits the lagoon through the ocean inlet. Maximum ebb flow currents in the inlet channel are only -0.8 m/sec (2.6 ft/sec) as the ebb flow volume flux is divided between the power plant intake and the ocean inlet. This is sufficient to flush the finer grain sizes from the bar in the recharge zone (cf. Figures 18 & 19) but not the coarser fractions in the 200 micron range. Thus the ebb tide flux that is scavenged by the power plant seawater consumption reduces the lagoons ability to flush sand from the lagoon even during spring tides.

Hydrodynamic simulations of flooding and ebbing neap tide currents on 14 June 2005 are plotted in Figures 27 & 28, respectively. The plant flow rate on this date remained at 501.1 mgd, (cf. Figure 8). The neap tide simulations show very similar flow structures as the spring tide simulations in Figures 25 & 26, only more sluggish and with less contrast in wetted lagoon area between flood and ebb due to the small tidal range during neap tides. Eddy systems remain well organized in the East Basin during flooding neap tides (Figure 27) and a weak boundary current (0.2 m/sec or 0.6 m/sec) flows along the north bank, helping to stir the East Basin water mass in spite of the relatively low energy of the system. Maximum inlet channel currents reach 0.7 m/sec (2.3 ft/sec) during flooding neap tides (Figure 27), less than half the inlet channel speeds as occurred during flooding spring tides at equivalent plant flow rate in Figure 25. Maximum inlet channel currents during ebbing neap tide (Figure 28) drop to only -0.2 m/sec (-0.7 ft/sec), well below the threshold of motion of the 120-210 micron fine sand on the West Basin bar in the recharge zone. Those no sand is flushed from the lagoon during neap tides.

TIDE_FEM simulations of flooding and ebbing currents during mean tidal ranges on 30 June 2005 are plotted in Figures 29 & 30, respectively. The plant flow rate on this date was very low, reduced to 207.4 mgd, well below the long term mean or even the flow requirements for the Carlsbad Desalination Project (cf. Figure 8). Again, the mean tide simulations show similar flow structures as the spring tide simulations in Figures 25 & 26, and although a bit more sluggish the wetted lagoon areas during flood and ebb and ebb are somewhat comparable to the spring tide cases. The south branch ebb current in the West Basin is significantly diminished due to the low plant flow rate, reaching only -0.2 m/sec (-0.6 ft/sec). The significant distinction of these mean tide simulations in Figures 29 & 30 is how the reduced plant flow rate has muted the flood flow currents in the inlet channel and allowed the ebb flow currents to be nearly comparable to spring tides and above threshold speed for the finer grain size fractions on the bar in the recharge zone. Maximum flood flow currents in the inlet channel during mean tides (Figure 29) reach 1.0 m/sec (3.2 m/sec), while maximum ebbing currents in the inlet during mean tides (Figure 30) remain at -0.6 m/sec (2.0 ft/sec), sufficient to scour and flush 120-180 micron size sand fractions from the bar in the recharge zone. Thus, reduction in plant flow rates affords improved flushing of sand from the lagoon during
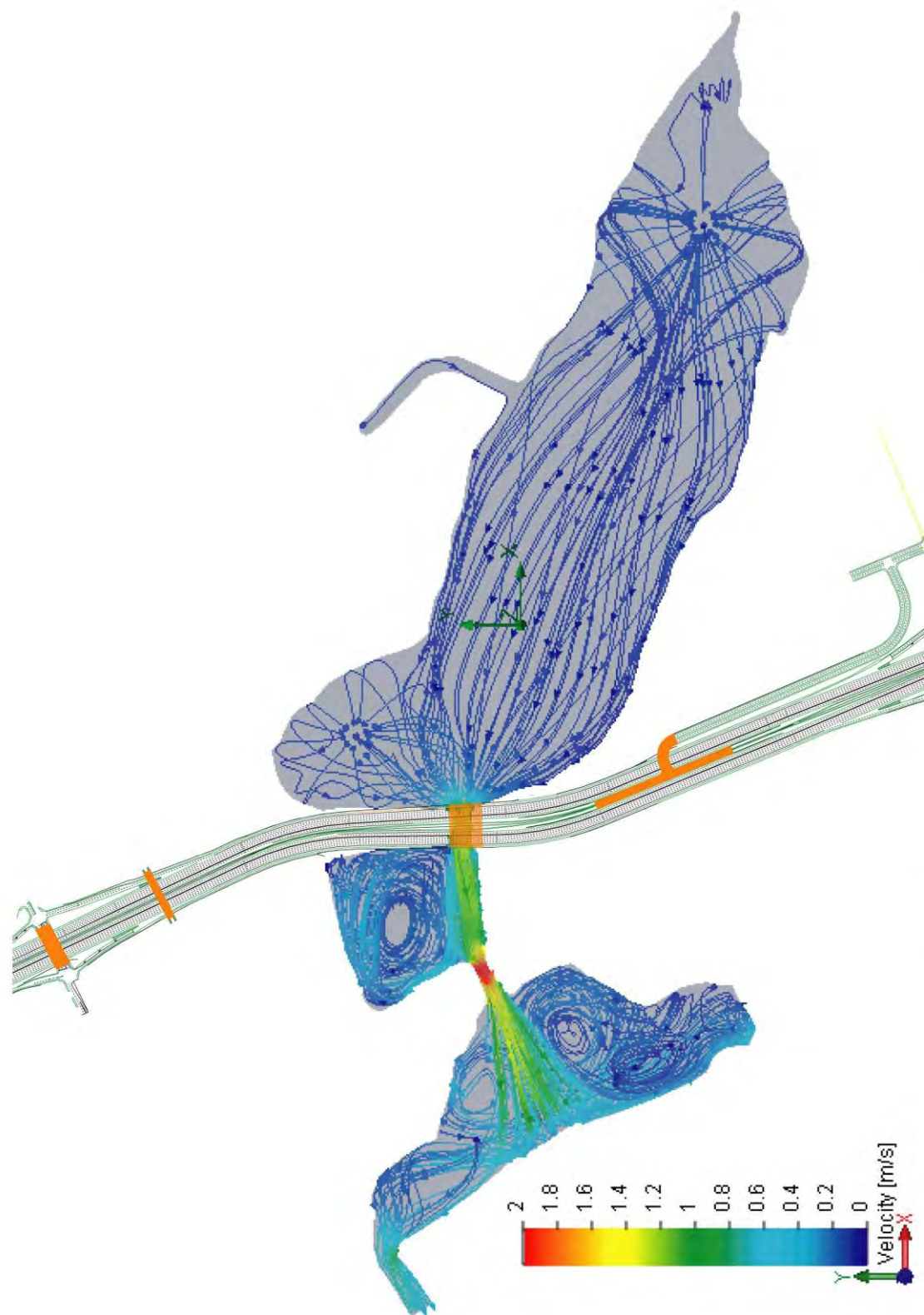
Figure 26. Hydrodynamic simulation of tidal flow out of Agua Hedionda Lagoon during spring ebbing tides.
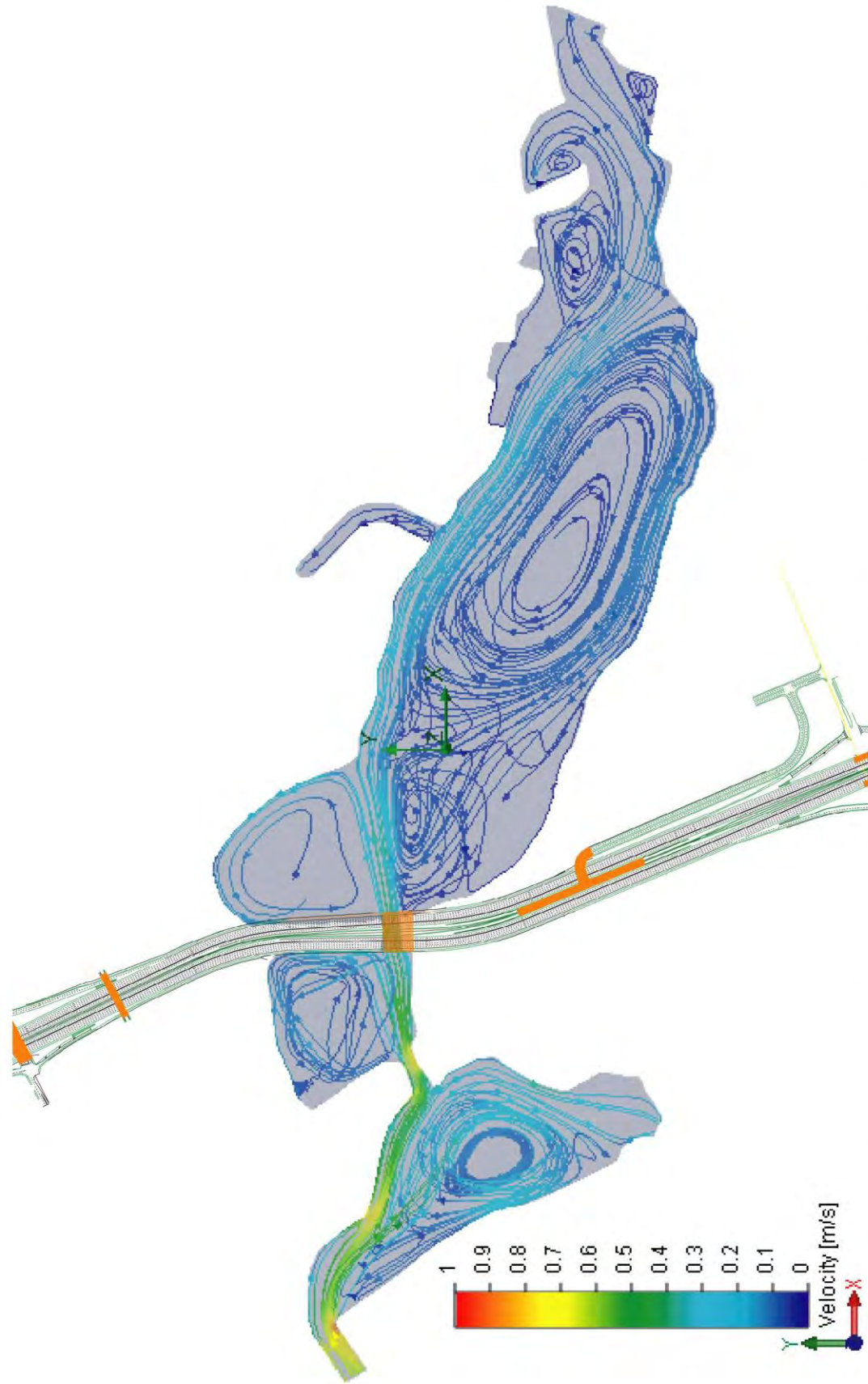
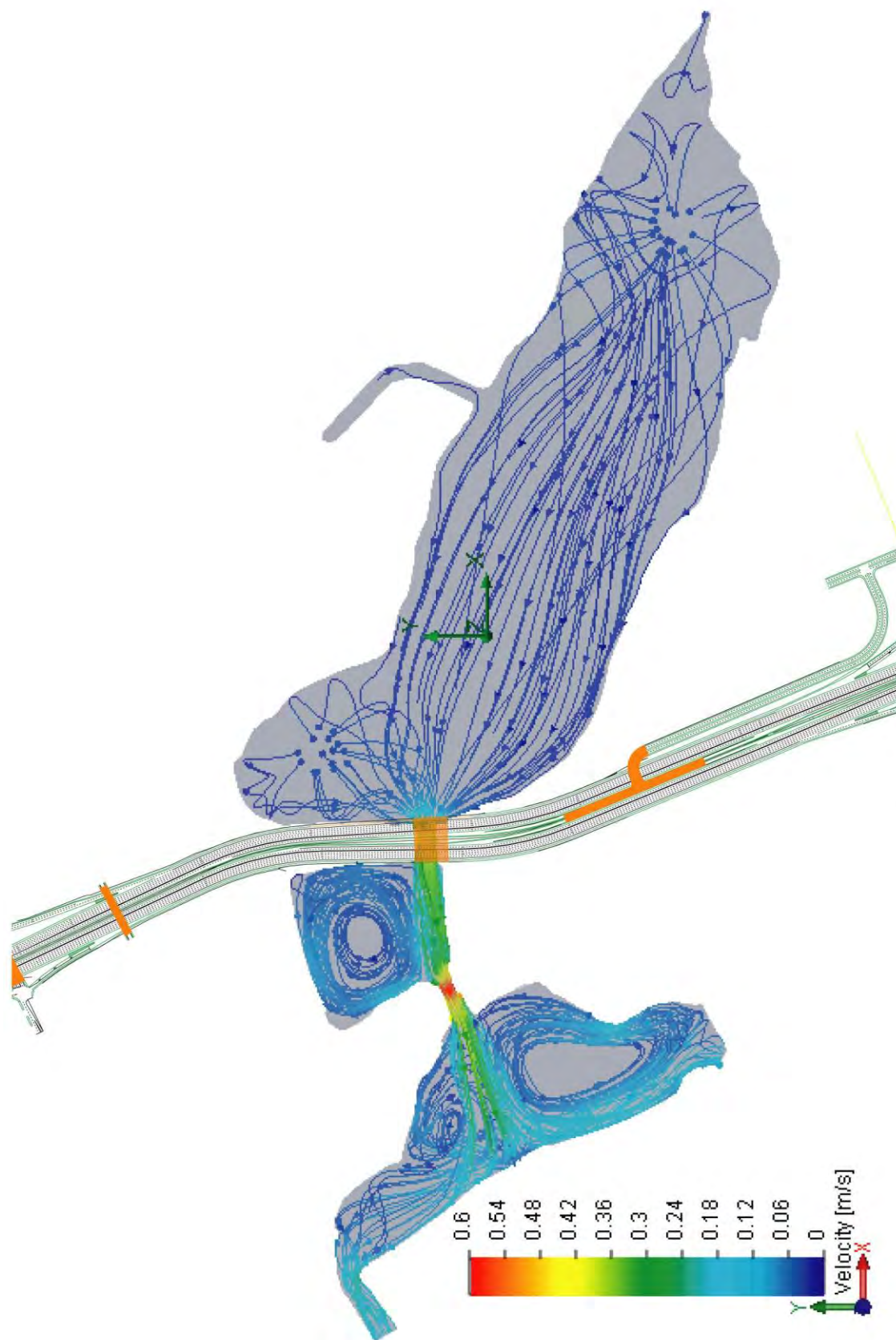**Figure 27.** Hydrodynamic simulation of tidal flow into Agua Hedionda Lagoon during neap flooding tides.

Figure 28. Hydrodynamic simulation of tidal flow out of Agua Hedionda Lagoon during neap ebbing tides.
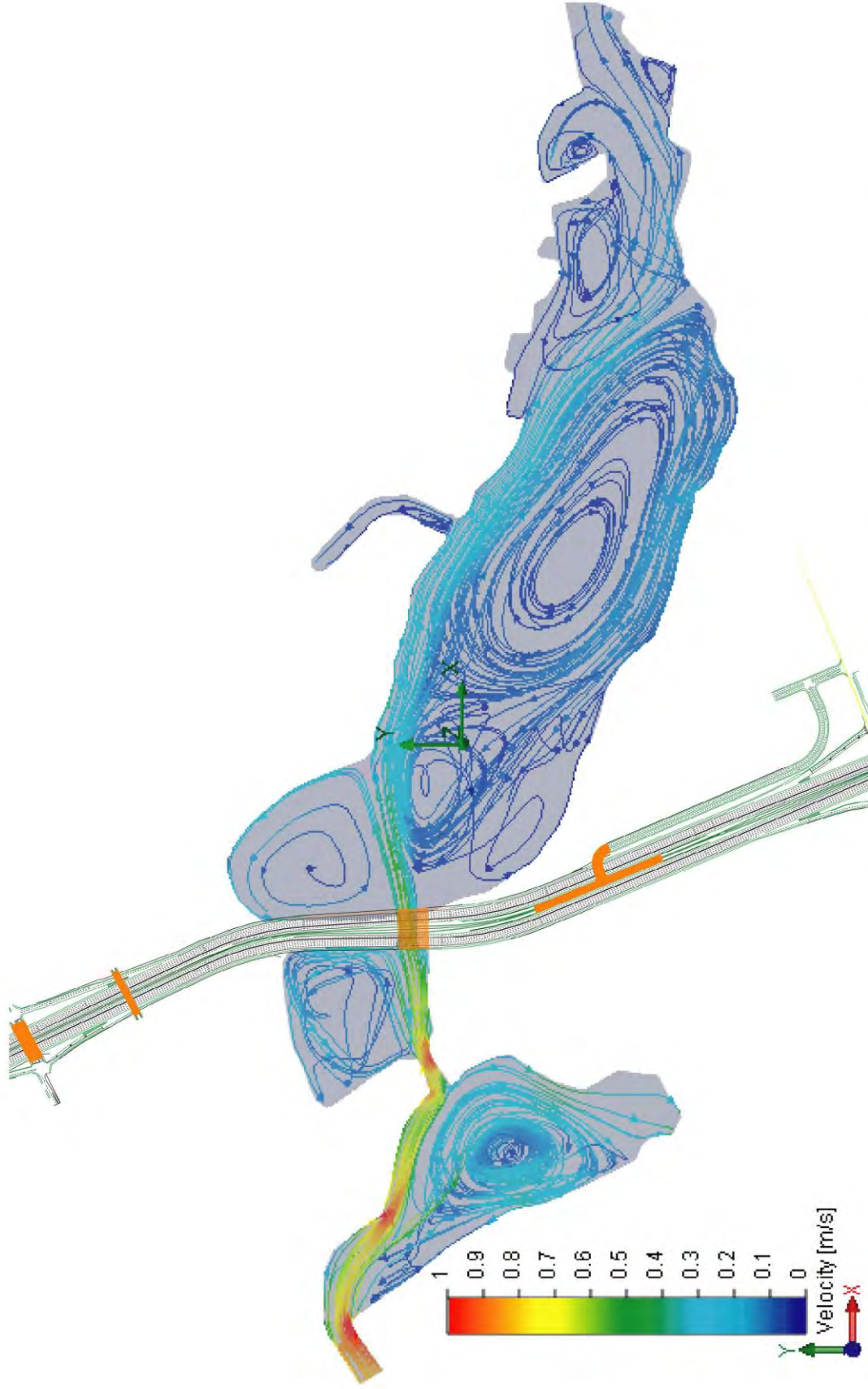
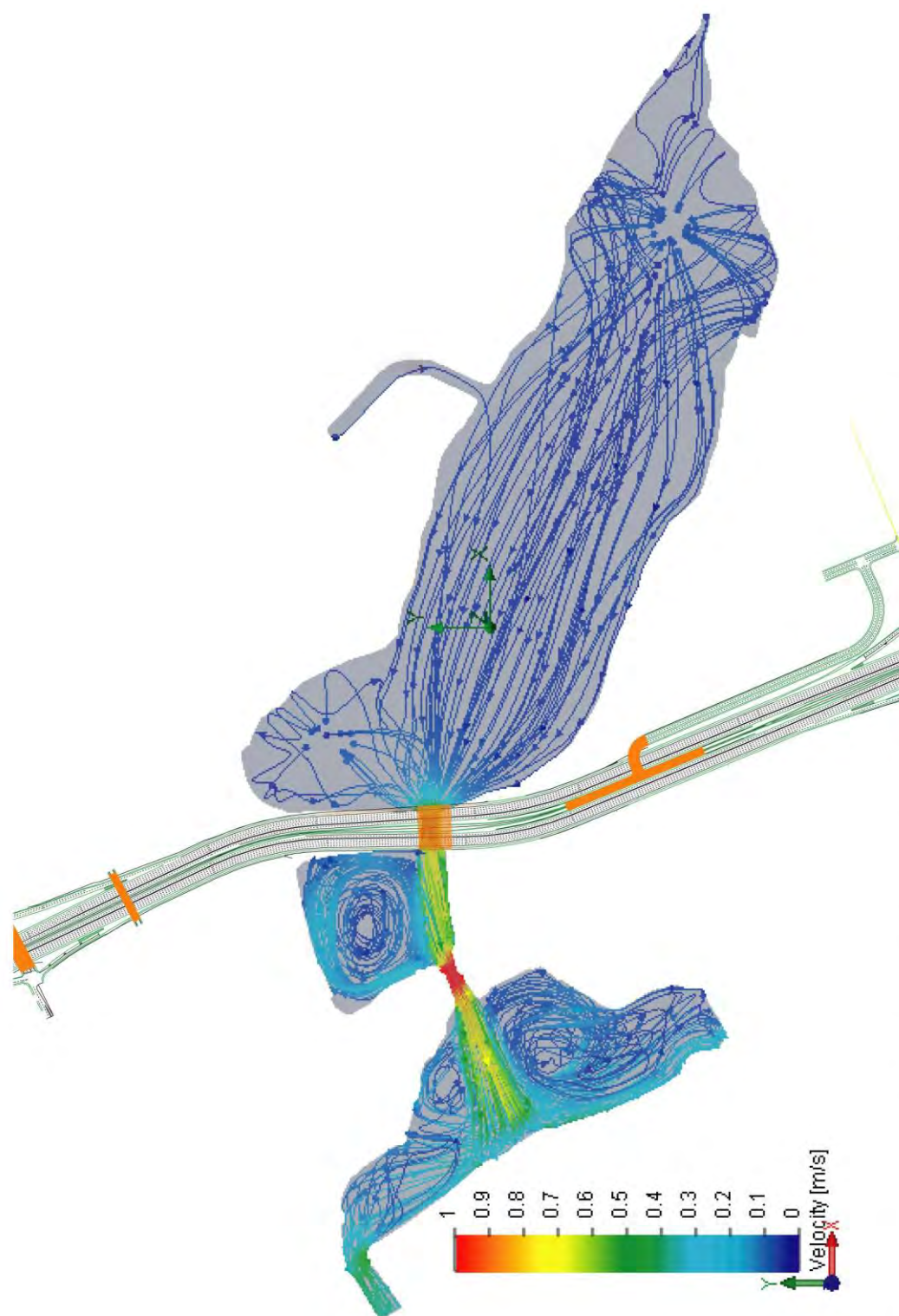**Figure 29.** Hydrodynamic simulation of tidal flow into Agua Hedionda Lagoon during mean flooding tides.

Figure 30. Hydrodynamic simulation of tidal flow out of Agua Hedionda Lagoon during mean ebbing tides.

ebb tide, even at average tidal ranges.

Figure 31 provides a quantitative assessment of the accuracy of the calibrated TIDE_FEM model over the entire 18 day calibration period of 13-30 June 2005. Here we compare East Basin water level variations predicted by the model (purple trace) with the actual water level measurements (black crosses) by Elwany et. al., (2005). The East Basin water level variations in purple are found to lag the ocean water levels by as much as 47 minutes during the spring tides on 21 June 2005, and this phase lag averages 39 minutes over the entire 18 day spring-neap cycle. The amplitudes and degree of non-linearity in the East Basin water level time series simulated by the model closely duplicate that observed in the measured lagoon tides. The maximum error in simulating the low tide elevations was found to be ε_L = +0.1 ft. The maximum high tide error in the model simulation relative to observations was found to be ε_H = -0.05 ft. Consequently, the calibration error appears to exhibit a systematic tendency. When amplitude errors occur they tend to over estimate the water elevation of the LLW tidal stage, and under estimate the water elevation of the HHW tidal stage. Although these errors are quite small and may be considered high predictive skill, this error mode would be consistent with *bathymetry errors* in which depth has been under estimated, Weiyan (1992). Bathymetry errors are the most common cause of modeling errors. Other sources of errors include:

> *ELEMENT INTERPOLATION ERROR*: Due to the degree of the polynomial used to specify shape function, N_i.
>
> *DISCRETIZATION ERRORS*: Due to mesh coarseness and approximating the curved wet/dry boundary side of an element with a quadratic spline.
>
> *QUADRATURE ERRORS*: Due to reducing the weighted residual integrals with the influence coefficient matrices.
>
> *ITERATION ERRORS*: Due to solving the system of algebraic equations reduced from the Galerkin Equations.
>
> *ROUNDOFF ERRORS:* Due to time integration by the trapezoidal rule.
>
> *SEA LEVEL ANOMALIES*: Due to discrepancies between the astronomic tides and the actual observed water levels in the ocean.
>
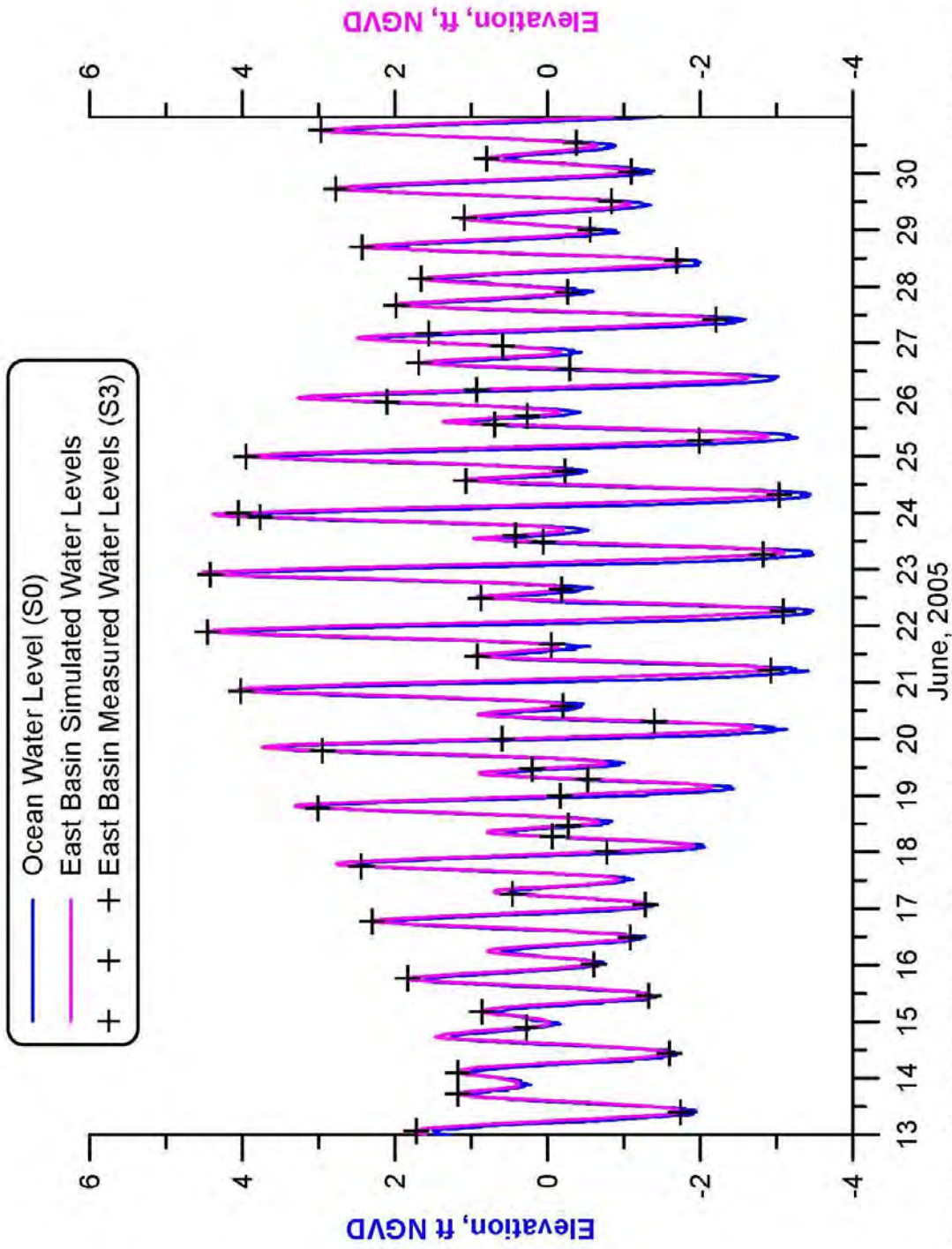> *INSUFFICIENT CALIBRATION DATA*: Due to limitations in the period of record.

Figure 31: TIDE_FEM model calibration using spring-neap cycle water level measurements from Elwany, et al. 2005. Ocean water levels (S0) indicated in blue; hydrodynamic simulation of east basin water levels shown in purple, east basin water level measurements (S3) shown as black crosses.

Power (auto-) spectra are useful tools for determining how the energy in complex time series like Figures 31 is distributed among various frequencies of oscillation. The predominant frequencies where most of the current energy appears (spectral peaks) can give clues that identify the mechanisms that predominate in the local tidal system. In Figure 32, auto spectra of the ocean tides (blue, upper panel) shows the predominant energy is centered on a diurnal frequency 10^{-5} Hz of the K1 lunar-solar diurnal tidal constituent at $f_{K1} = 1.16079$ x 10^{-5} Hz. The energy in this peak is disproportionately high relative to the next largest spectral peak occurring at the M2 principal lunar semi-diurnal tidal constituent, $f_{M2} = 2.2365$ x 10^{-5} Hz. The excess energy at diurnal frequencies is believed to be non-tidal and attributable to a wind-driven current component that has a diurnal fluctuation in response to daily heating of the land. With the onset of summer heating of the inland deserts, this diurnal sea breeze component would be strengthening in the June time frame of the 2005 lagoon monitoring.

Other less energetic tidal peaks are also found in the spectra of Figure 32 including one believed to be a baroclinic *shelf resonance* formed by a resonant *triad* at the sum of the frequencies of the K1 and M2 barotropic tides, ie a diurnal third harmonic at a frequency $f_3 = f_{K1} + f_{M2} = 3.3973$ x 10^{-5} Hz. This diurnal third harmonic is a baroclinic tide excited by the barotropic K1 and M2 tides interacting with the bottom topography, in particular the Carlsbad Submarine Canyon (see Figure 3). Another baroclinic shelf resonance apparent in the spectra of the ocean tides in Figure 32 is a second harmonic of the barotropic M2 tide appearing at a frequency of $2f_{M2} = 4.4730$ x 10^{-5} Hz. The auto spectra of the east basin tides shown in green in the lower panel of Figure 32 exhibits the same primary barotropic and baroclinic tidal peaks as the ocean tides in the upper panel; with one exception; an additional non-linear resonance appears as a triad formed by the sum of the K1 barotropic mode and the baroclinic second harmonic of the M2 tide, $f_{K1} + 2f_{M2} = 5.6338$ x 10^{-5} Hz. Apparently this mode is excited by non-linear tidal interaction with the lagoon bathymetry.

The other quantitative data used to assess the accuracy of the calibrated TIDE_FEM model are the inlet channel currents, measured by Elwany et. al., (2005)
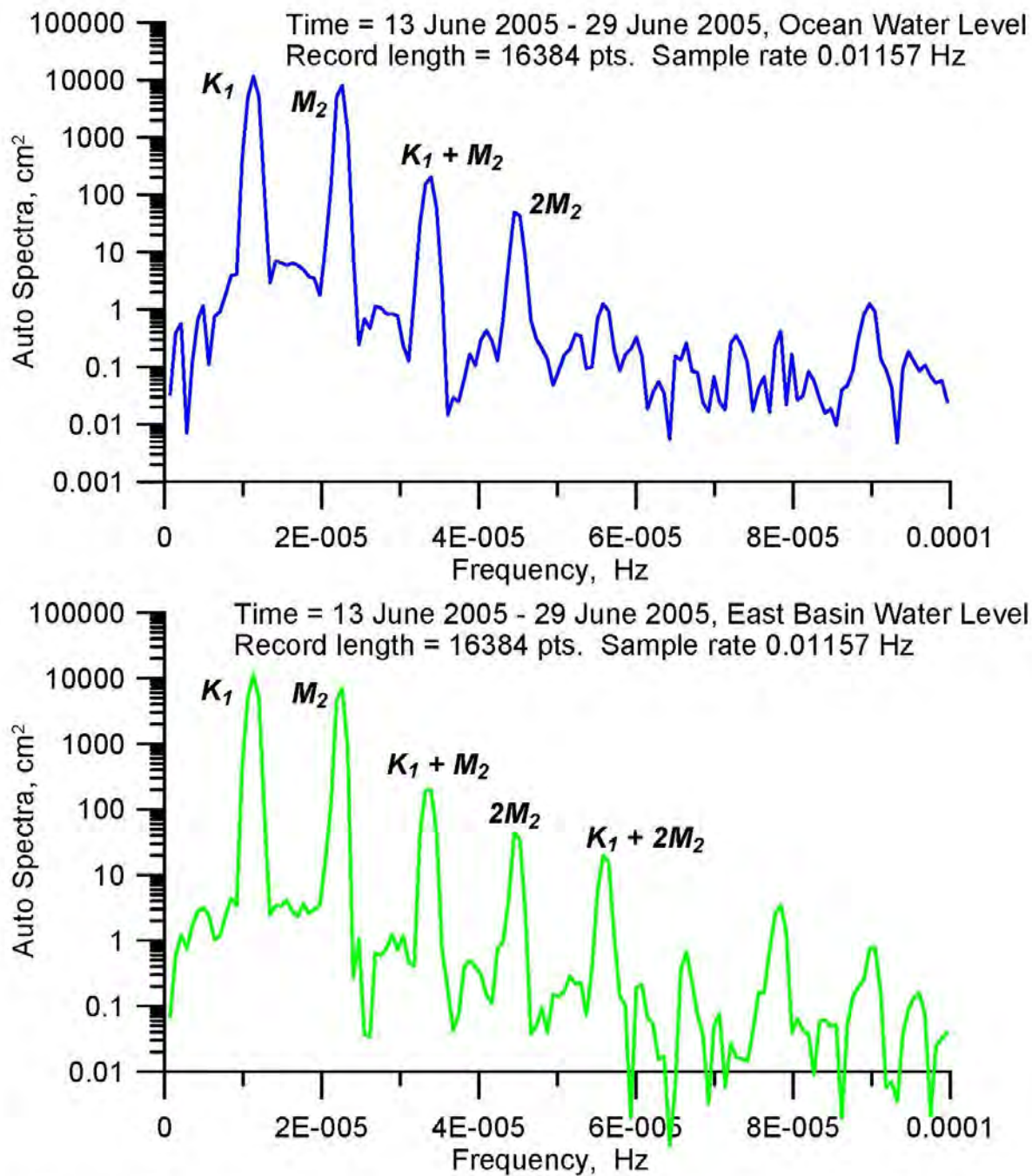
Figure 32 . a) Ocean water level spectra; b) Agua Hedionda East Basin water level spectra, 13 - 29 June 2005.

during the lagoon monitoring period of 13-30 June 2005. Figure 33 compares the TIDE_FEM model simulations of inlet channel currents (green) against inlet velocity measurements (black crosses). For reference, the ocean tides are indicated in blue. The flood and ebb current maximums and minimums in the inlet channel are found to lead the high and low ocean water levels by as much as 13.7 hours during the spring tides on 21 June 2005. Maximum flood tide currents on this day were 5.16 ft/sec, while maximum ebb tide currents were -2.87 ft/sec; the flood tide dominance due to the scavenging effect of the power plant intake rate on the available lagoon water volume which was operating at 501 mgd. Throughout the 18 day monitoring period, average flood tide currents in the inlet channel were 1.91 ft/sec while average ebb tide currents were -0.91 ft/sec while the power plant averaged an intake flow rate of 430.97 mgd. The amplitudes and degree of non-linearity in the inlet current time series simulated by the model closely duplicate that observed in the measured currents. The maximum error in simulating the ebb tide currents was found to be ε_L = +0.1 ft/sec. The maximum flood tide error in the modeled currents relative to observations was found to be ε_H = -0.05 ft/sec. Again, this type of systematic simulation error is characteristic of bathymetry errors in the model input file; however, the size of these errors is well within what is considered to be high predictive skill.

Figure 34 compares the auto spectra of the inlet channel currents in green in the lower panel against the ocean tidal spectra from Figure 32 in blue in the upper panel. Spectral peaks in the ocean tides are all found in the spectra of the inlet channel currents but some of the higher harmonics are disproportionately large and there are also additional higher harmonics not found in the ocean tides. In particular, the M2 tidal peak in the spectra of the inlet channel currents has more energy than the K1 peak. This is probably indicative of non-linear friction effects on the inlet channel currents, producing a second harmonic of the diurnal K1 component that overlays on the semidiurnal M2. The diurnal third harmonic is present in the inlet channel currents at the sum of the frequencies of the K1 and M2 barotropic tides, as well as the second harmonic of the M2 tides. But we also find in the inlet channel current spectra the triad observed in the east basin water level spectra (Figure 32) formed by the sum of the K1 barotropic mode and
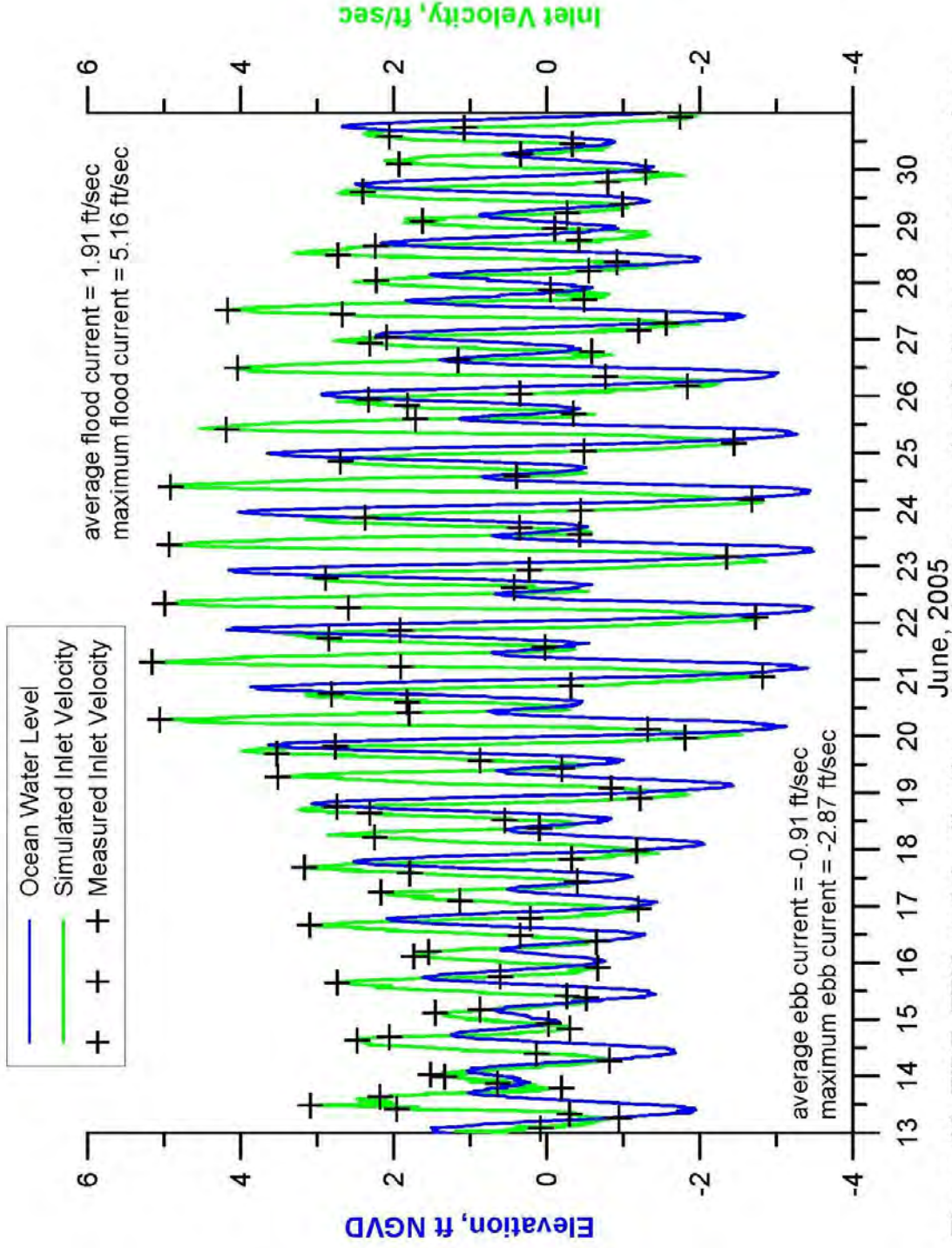
Figure 33: TIDE_FEM model calibration using spring-neap cycle velocity measurements from Elwany, et al. 2005. Ocean water levels (S0) indicated in blue; hydrodynamic simulation of inlet velocity shown in green, inlet velocity measurements (S0) shown as black crosses.
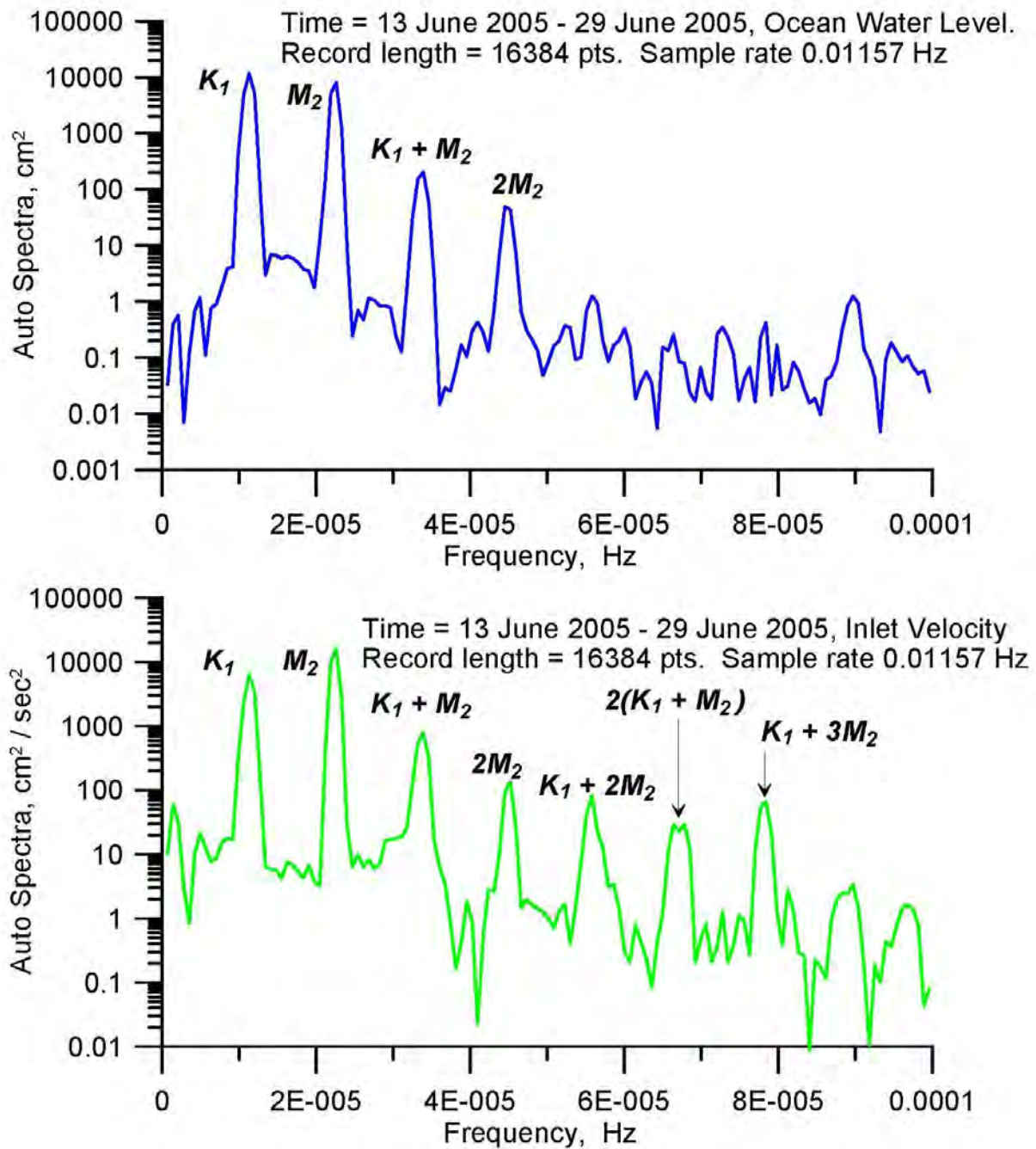
66

Figure 34 . a) Ocean water level spectra; b) Agua Hedionda inlet velocity spectra, 13 - 29 June 2005.

the baroclinic second harmonic of the M2 tide; so apparently that non-linear bathymetric mode was excited at the inlet. Further evidence of non-linear friction interacting with bathymetry is the presence of additional triads at higher harmonics of the inlet channel current spectra. These harmonics are not present with significant energy in the East Basin water level spectra of Figure 32. These frictionally generated harmonics include a second harmonic of the triad formed by the sum of the K1 barotropic mode and the baroclinic second harmonic of the M2 tide, $2\,(f_{K1} + f_{M2}) = 6.7946$ x 10^{-5} Hz; and a triad formed by the sum of the K1 barotropic mode and the baroclinic third harmonic of the M2 tide, $f_{K1} + 3f_{M2} = 7.8703$ x 10^{-5} Hz. The presence of these non-linear higher harmonics in the inlet channel currents exert a strong influence on the transport of sand into the West Basin, as sediment transport is proportional to the cube of the inlet channel velocity.

 As a final test of the calibration and stability of the TIDE_FEM model we perform an ultimate simulation of the tidal transport in Agua Hedionda during the highest ocean water level ever recorded. This is referred to as the extreme high water (EHW) level and occurred during the 1997 El Nino on 13 November 1997 when ocean water levels reached 7.65 ft MLLW at the Scripps Pier tide gage. (One of the utilities of hydrodynamic models is in the recreation of extreme events that were not well observed). Figure 35 shows the flood flow simulation of Agua Hedionda Lagoon during the 13 November 1997 extreme high water level event. It displays many similar flow structures to the spring tide flood flow simulation in Figure 25, although the wetted footprint of the lagoon is significantly larger and more complex during the EHW event. To facilitate comparisons with Figure 25, the EHW simulation in Figure 35 is based on an equivalent plant flow rate of 501.1 mgd, or about the same as the long term mean. Figure 35 reveals maximum currents in the inlet channel reach 2.2 m/sec or 7.2 ft/sec. The flood tide jet along the north bank of the West Basin sustains speeds of between 1.5 m/s (4.9 ft/sec) to 2.0 m/sec (6.5 ft/sec), well above the threshold of motion of the fine sand on the bar in the recharge zone (cf. Figures 18 & 19) and more than sufficient to induce scour and erosion of those sands. The eddy in the central portion of the west basin spins at 0.4 m/sec (1.3 ft/sec) but the middle portion of the recharge zone remains near stagnation. The feeder current toward the plant intake runs at about -0.4 m/sec (-1.3 ft/sec), the same as in the spring tide simulation in Figure 25 since both simulations are using the same
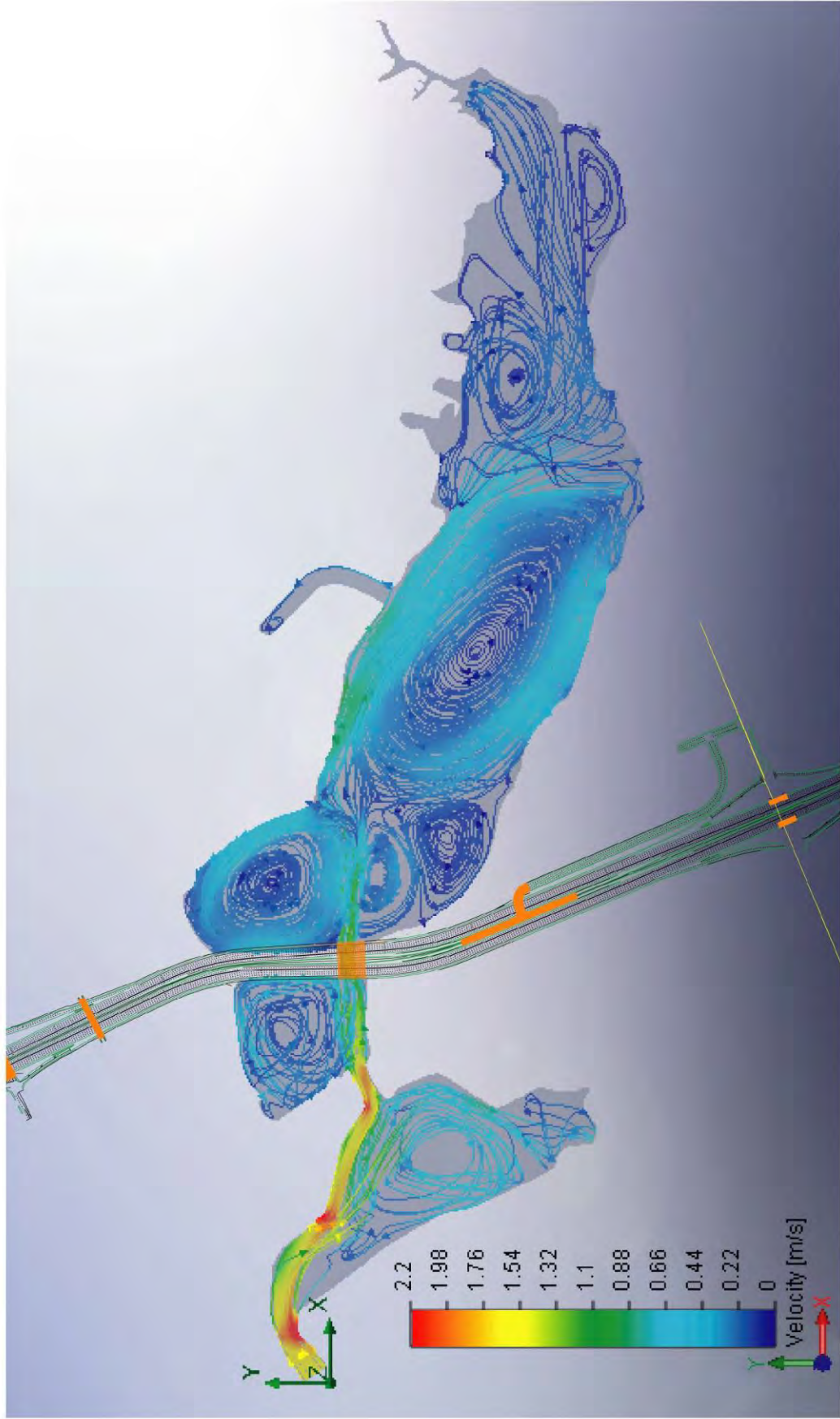
Figure 35. Hydrodynamic simulation of tidal flow into Agua Hedionda Lagoon during extreme high water flooding tides.

plant flow rate, and circulation in the southern end of the West Basin is largely driven by plant flow rate. The flood tide jet along the north bank of the West Basin speeds back up to as high as 1.8 m/sec (5.9 ft/sec) as it passes through the hardened channel under the rail road bridge and then spins up a somewhat more orderly Central Basin eddy. The core of the Central Basin eddy remains at stagnation, again providing ideal conditions for suspended sediment to settle and deposit. Flood tide currents during the EHW event speed back up to 1.0 m/sec (3.2 ft/sec) through the hardened channel under the I-5 bridge before diverging into a complex set of rather vigorous counter rotating eddies that populate the East Basin. This eddy structure includes 5 counter rotating eddies in the East Basin, two more than found for the spring tide flood simulation in Figure 25. East Basin eddy speeds are on the order of at 0.4 m/sec (1.3 ft/sec), for times stronger than for the spring tide flood simulation in Figure 25. The high marsh area at the east end of the East Basin exhibits a disorganized meandering flow system during the EHW event. From this collection of calibration scenarios, we conclude that the TIDE_FEM model remains stable and well-behaved for all the way through the most extreme possible water level variations.

3.8 Calibration of the Coupled Littoral and Tidal Transport Models: In this section we use historic dredge data for Agua Hedionda Lagoon to calibrate the coupled SEDXPORT/TIDE_FEM models. We use this historic dredging survey record from Table 1 to calibrate the tidal hydraulics model such that the modeled sand influx due to tidal transport matches with the historic accumulation of sand in the West Basin as measured by the dredge record. This involved successive iterations which varied the tidal transport efficiencies ε_s , ε_b and the drag coefficient, c_f , in the sediment transport algorithms detailed in Jenkins, et al, (2007). The calibrations were initialized in the nearfield control cell (Figure 1) for historic beach fill placements as indicated in Table 1 due to Agua Hedionda disposal activities, and for regional beach fills in the far field control cell (Figure 3) as indicated in Appendix A.

Figure 36 gives an example of tidal transport simulation through a pair of spring-neap cycles for the historic calibrated conditions during the month of August 1994. This month was selected because the plant flow rate historically had less variability than any month in the period of record, and was roughly constant at 600.6 mgd. This fact helps to
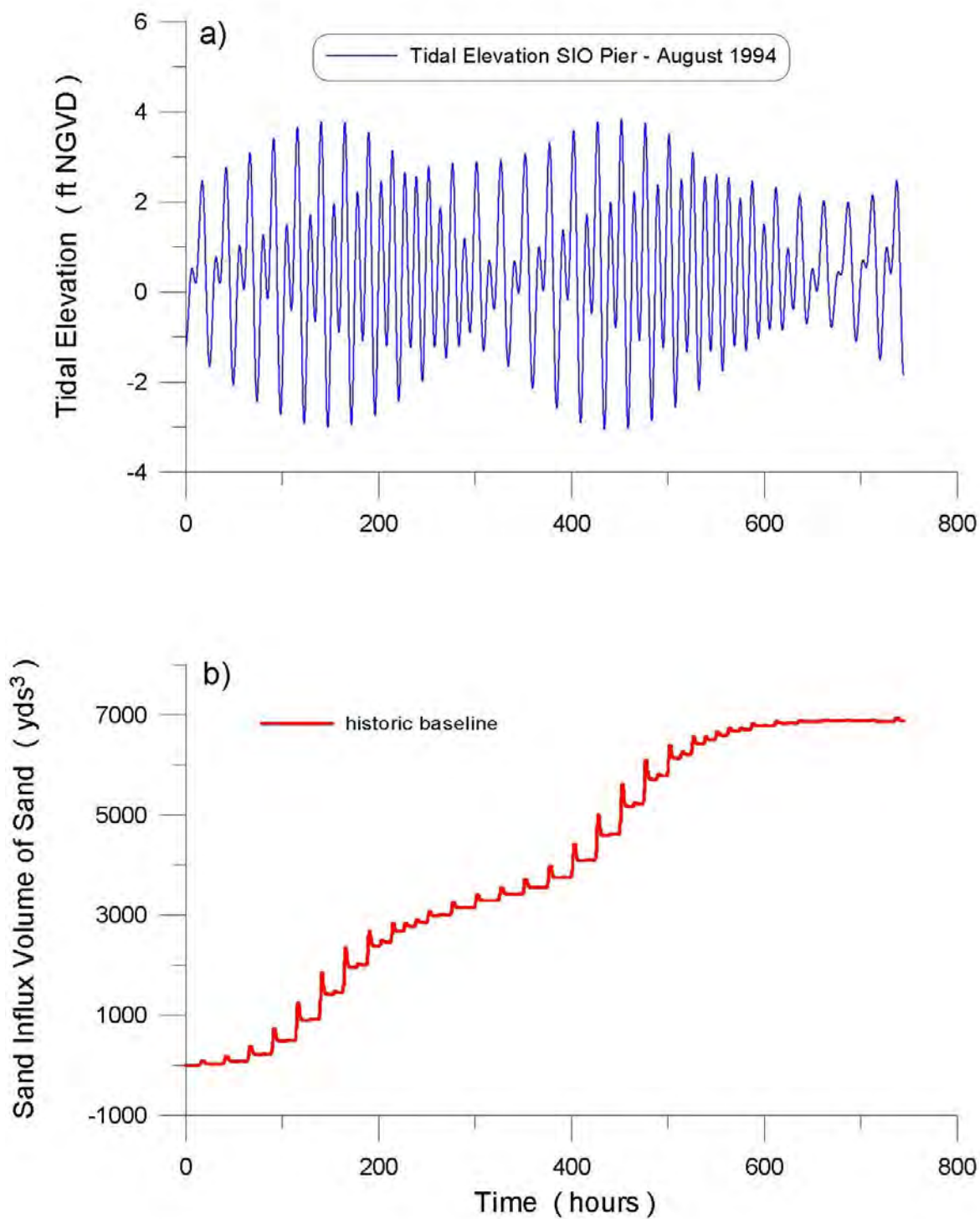
Figure 36. a) tidal elevation at SIO Pier for August 1994, and b) calibrated simulation of sand influx volume accumulated at 0.1 hour intervals for historic conditions.

isolate the modulation on sand influx due to the tides alone. We find from comparing the sand influx in the lower panel with the ocean tides in the upper panel that nearly all of the tidal transport occurs before and after the high tide levels. This results from most of the lagoon storage volume residing at the higher stage elevations, (Figure 17); and that water level variations at these higher stages produce the largest volume exchanges and the highest velocities through the and inlet channel and recharge zone (see Figure 33). Note that the ebb flow transport rates are significantly less than the flood flow transport rates (flood dominance). This is due to withdrawal of lagoon water by the power plant and is further exacerbated by diminished tidal prism when the West Basin shoals from sand influx and begins to reduce the ability of the lagoon to fully drain during ebb flow. The flood dominance effect on transport rate is magnified by the fact that tidal transport varies as the cube of the velocity per Jenkins and Inman (1999) and Jenkins, et. al.,(2007); and that a small asymmetry in tidal velocity magnitudes between flood and ebb makes a large difference in flood vs ebb transport.

The other notable feature of the transport rates in the lower panel of Figure 36 is the fact that a substantial fraction of the flood tide flux is flushed from the recharge zone during the following ebbing flow. The amount of ebb flushing is controlled by the daily tidal prism and plant flow rate. However we will show that the amount of influx during flooding flow can greatly exceed that for the average conditions depicted in Figure 36, particularly during combinations of high littoral transport, spring tides and high user demand.

The importance of the spring neap cycle on sand influx rates is apparent in Figure 36 from the bursts of influx on flood tide are greatest during spring tides, when the tidal velocities and entrainment radius of the inlet flows are greatest. However during the neap tides, when tidal entrainment is minimal, little net influx occurs.

Figures 37-41 give the sediment influx accumulations from the calibration trials of the model over the entire model simulation time period 1981-2007. Each figure gives the cumulative influx volume time series as a separate line type for a particular maintenance dredge cycle. The corresponding daily influx rates to the recharge zone of the West Basin are shown in the lower panel of each figure. Each dredge cycle is annotated with the corresponding beach disposal volumes and locations. Middle
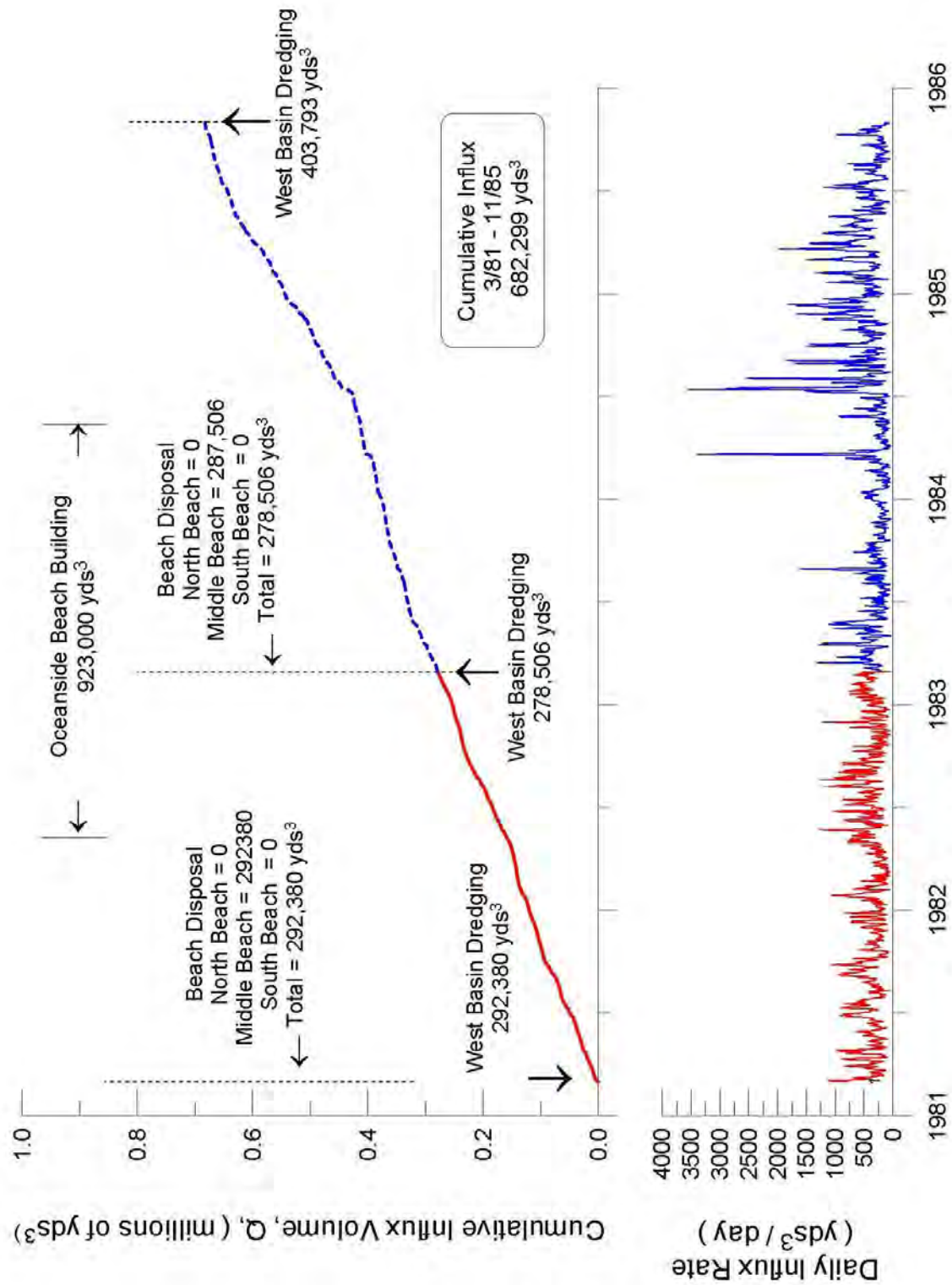
Figure 37. Model Calibration for Sand Influx Rate, Historic Conditions Agua Hedionda Lagoon - Simulation Period 1981-1985
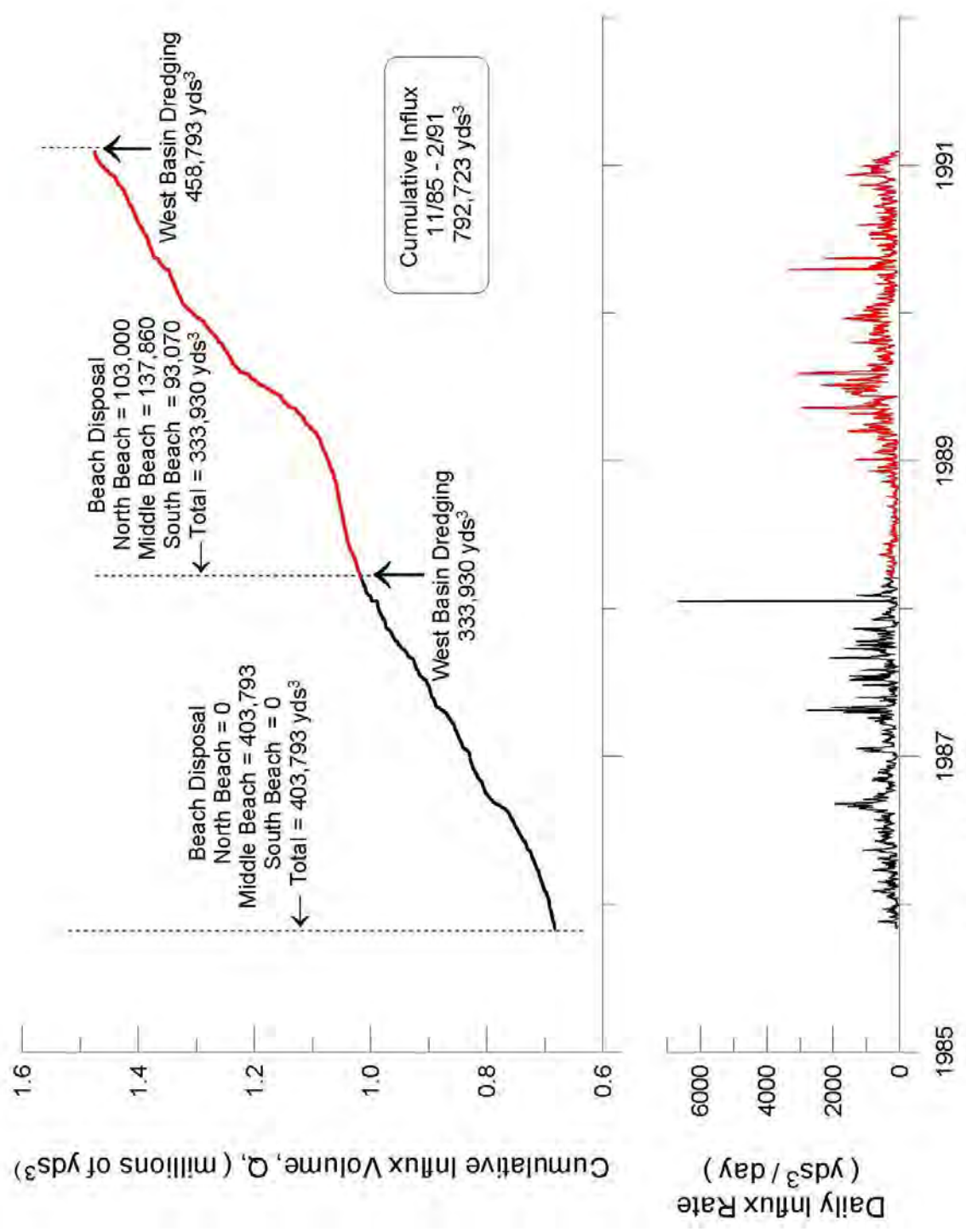
Figure 38. Model Calibration for Sand Influx Rate, Historic Conditions Aqua Hedionda Lagoon - Simulation Period 1985-1991
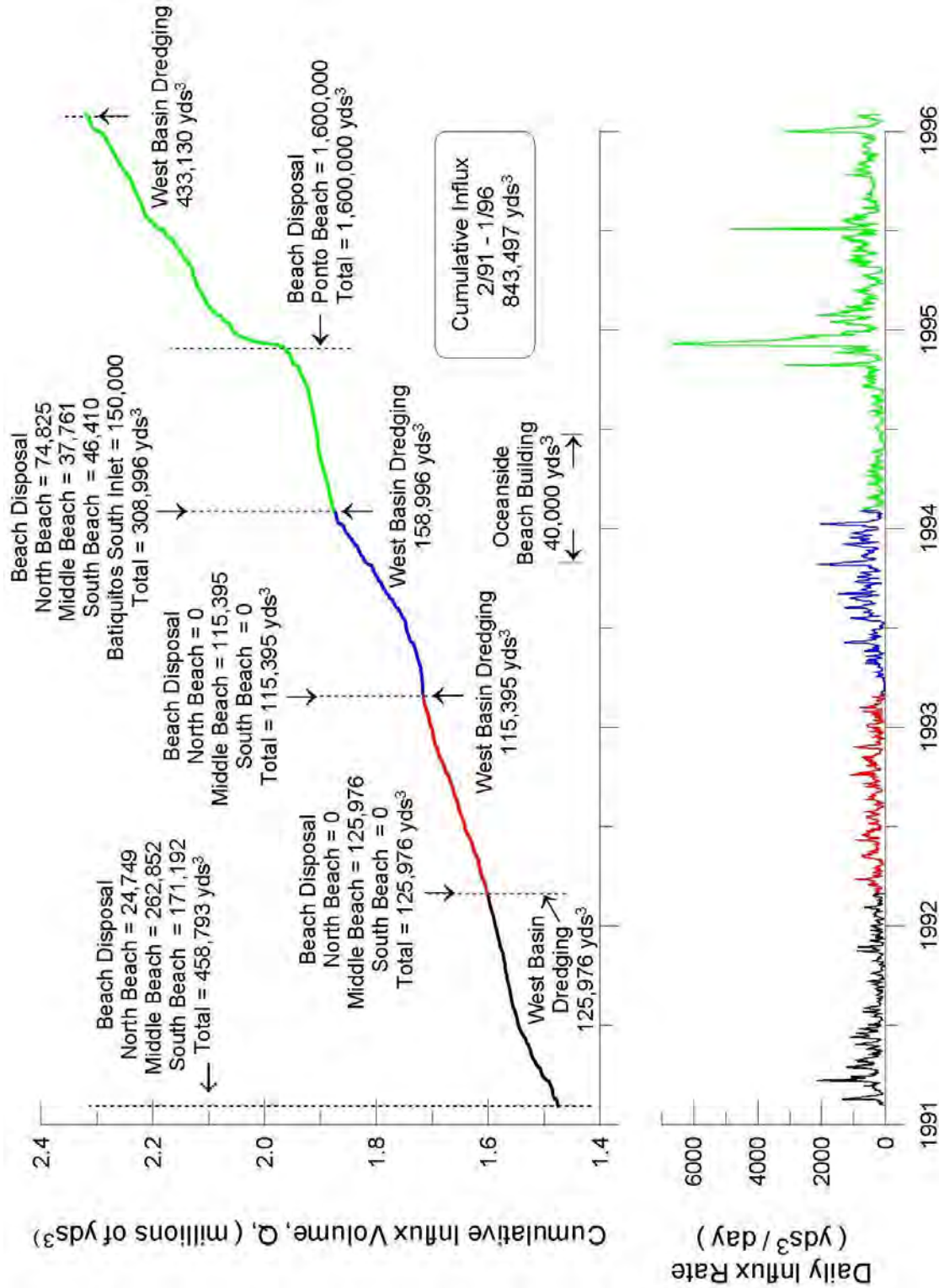
Figure 39. Model Calibration for Sand Influx Rate, Historic Conditions
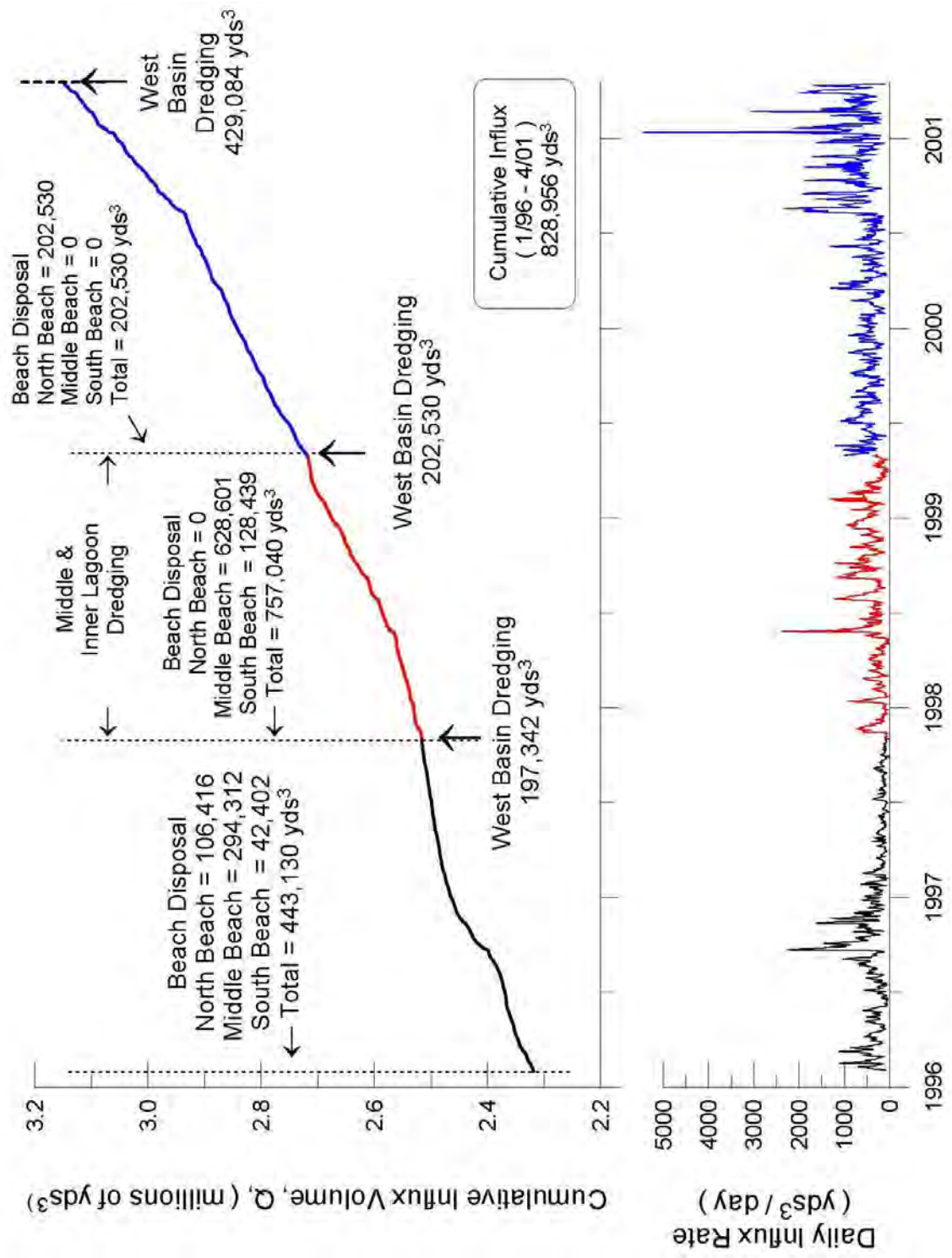Aqua Hedionda Lagoon - Simulation Period 1991-1996

Figure 40. Model Calibration for Sand Influx Rate, Historic Conditions
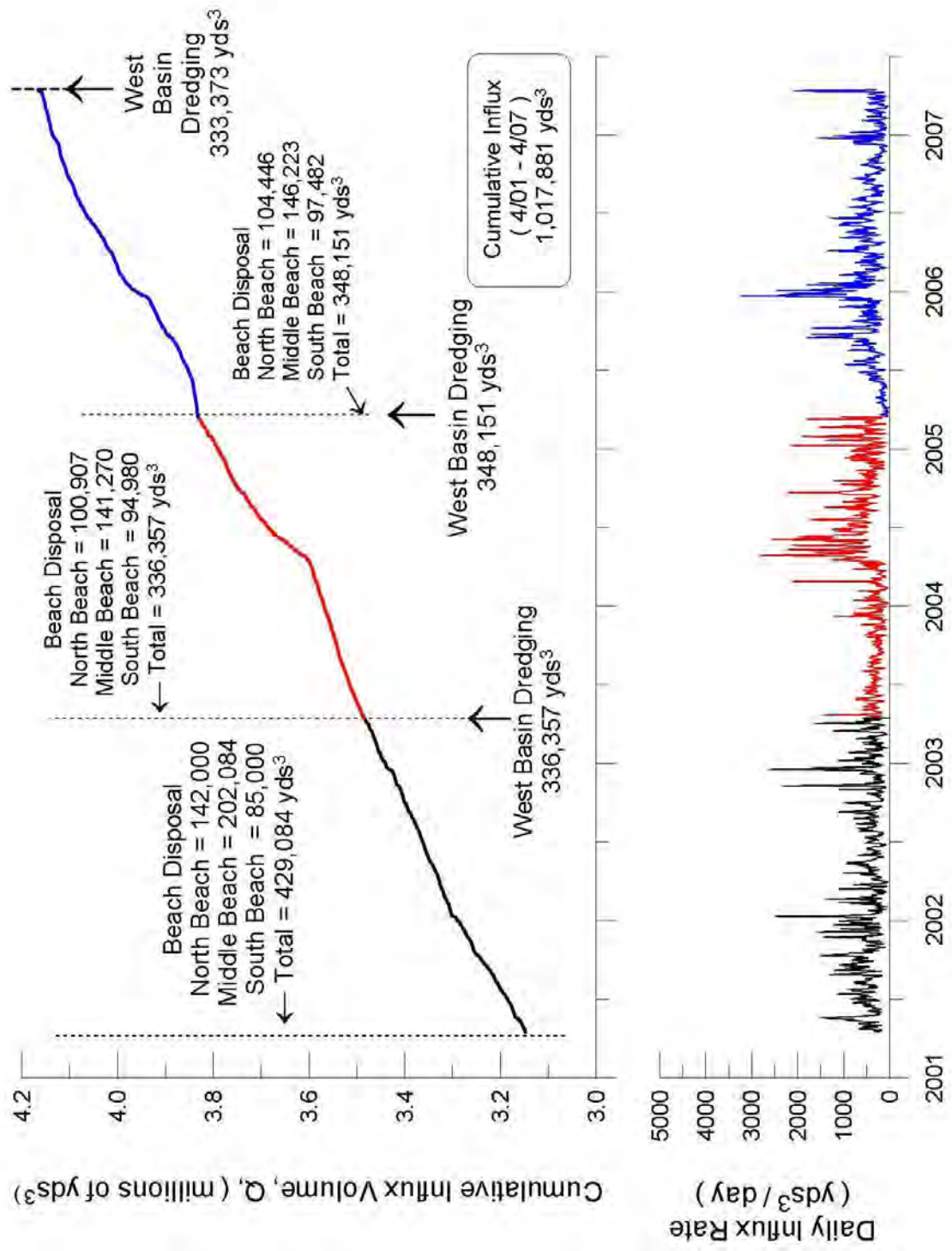Agua Hedionda Lagoon - Simulation Period 1996-2001

Figure 41. Model Calibration for Sand Influx Rate, Historic Conditions
Agua Hedionda Lagoon - Simulation Period 2001 - 2007

and South Beach disposal volumes were initialized at Q_{n4} in Figure 7, while North Beach
disposal volumes were initialized at Q_{n5}.

The total cumulative influx of sand into the lagoon was 4,165,849 cubic yards
over the 27 year calibration period between 1981 and 2007. By manipulation of the
calibration coefficients, the model was forced to match the cumulative dredge totals at
each historic dredge interval. This basket of calibration factors was used without further
modification for all future scenarios studied in Section 3. In general we find that
sediment influx rates accelerate during the events of large waves (Figure 13). This is an
indication that the tidal influx rates of sediment are limited by the rates at which the wave
driven transport delivers littoral sands to the inlet at Agua Hedionda Lagoon. The 1981-
2007 time period contained twenty major episodes of large waves with high littoral
transport rates. Indeed, the biggest wave event in the 27 year period of record (the 18
January 1988 storm) produced the highest littoral transport rate and a very pronounced
acceleration in the sediment influx rate to the lagoon (Figure 38). This storm also
occurred during a spring tide at a time when there was abundant sand supply in the
nearfield due to disposal of 333,930 cubic yards of Agua Hedionda maintenance dredging
with back-passing of 103,000 cubic yards to North Beach ongoing at the time the storm
struck. The simultaneous occurrence of enormous waves, spring tides and enriched
beach volume to the north produced a remarkable daily influx volume of nearly 7,000
cubic yards (Figure 38).

There were other times in the period of record when high littoral transport rates
and high tidal influx rates occurred in the absence of such an extreme wave event. But
these high influx/average wave episodes all occurred immediately after upcoast beach
nourishment or North Beach disposal. In particular 16 January 2001 storm involved
waves less than half as high as the 18 January 88 storm, but still caused almost 5000
cubic yards of daily influx to the lagoon following back-passing of 202,530 cubic yards
to North Beach (Q_{n5} in Figure 5). Furthermore of the 20 high influx rate episodes in the
period of record, 62% occurred following upcoast disposal and nourishment either at
North Beach or Oceanside. Therefore, a leading order cause of high sand influx at Agua
Hedionda appears to be updrift beach nourishment activity. The physics of this
relationship is the fact that sand influx to the lagoon is limited by the longshore wave

driven transport past the inlet, which in turn is frequently limited by the available supply of beach sand updrift of the lagoon.

4.0) Model Analysis of Removal of the South Beach Groin:

In the preceding section the coupled littoral/tidal transport modeling system of the Coastal Evolution Model (CEM) was calibrated to give sand influx rates into the recharge zone of the West Basin that exactly match the historic dredge amounts for historic plant flow rates and back-passing over the extended time period 1981-2007. In this section we will use that calibrated modeling system to estimate the future impacts of removal of the South Beach Groin on the shoreline evolution of North Beach, Middle Beach and South Beach.

The three most critical variables controlling the lagoon dredging and local beach disposal are: 1) *time*, the lagoon traps increasing amounts of littoral sands over time until the recharge zone is completely filled and the inlet closes; 2) *plant flow rates*, as the power plant draws increasing amounts of lagoon water for cooling, the flood tide velocities into the inlet become stronger and the ebb tide velocities weaker, whence more littoral sand is entrained into the lagoon and less flushed out and the lagoon then traps sand at a faster rate; 3) *back-passing*, this is a regulatory requirement for placing sand dredged from the lagoon on the updrift beaches and causes that sand to continuously recycle between the lagoon and the receiver beach, thereby increasing the rate at which the lagoon traps sand. The time variable interacts with the other two because the transport processes are non-linear and continuous, and times controlling influence on historic dredge requirements is obvious in Figures 36-41.

The shoreline evolution scenarios with the South Beach Groin in place and with it removed were run out in time for 20 years in CEM simulations, and then compared over the domain of the nearfield in Figure 6. This domain extends 25,000 ft to the north of the inlet to Agua Hedionda and 35,000 ft to the south, with North Beach, Middle Beach and South Beach nested in the approximate center of this reach of shoreline. Back-passing was assumed to occur at historic rates with every dredge cycle throughout these 20-year long simulations. Figure 42 shows the shoreline evolution at five year intervals over a 20-year long simulation with the South Beach Groin in place and with historic back-passing.
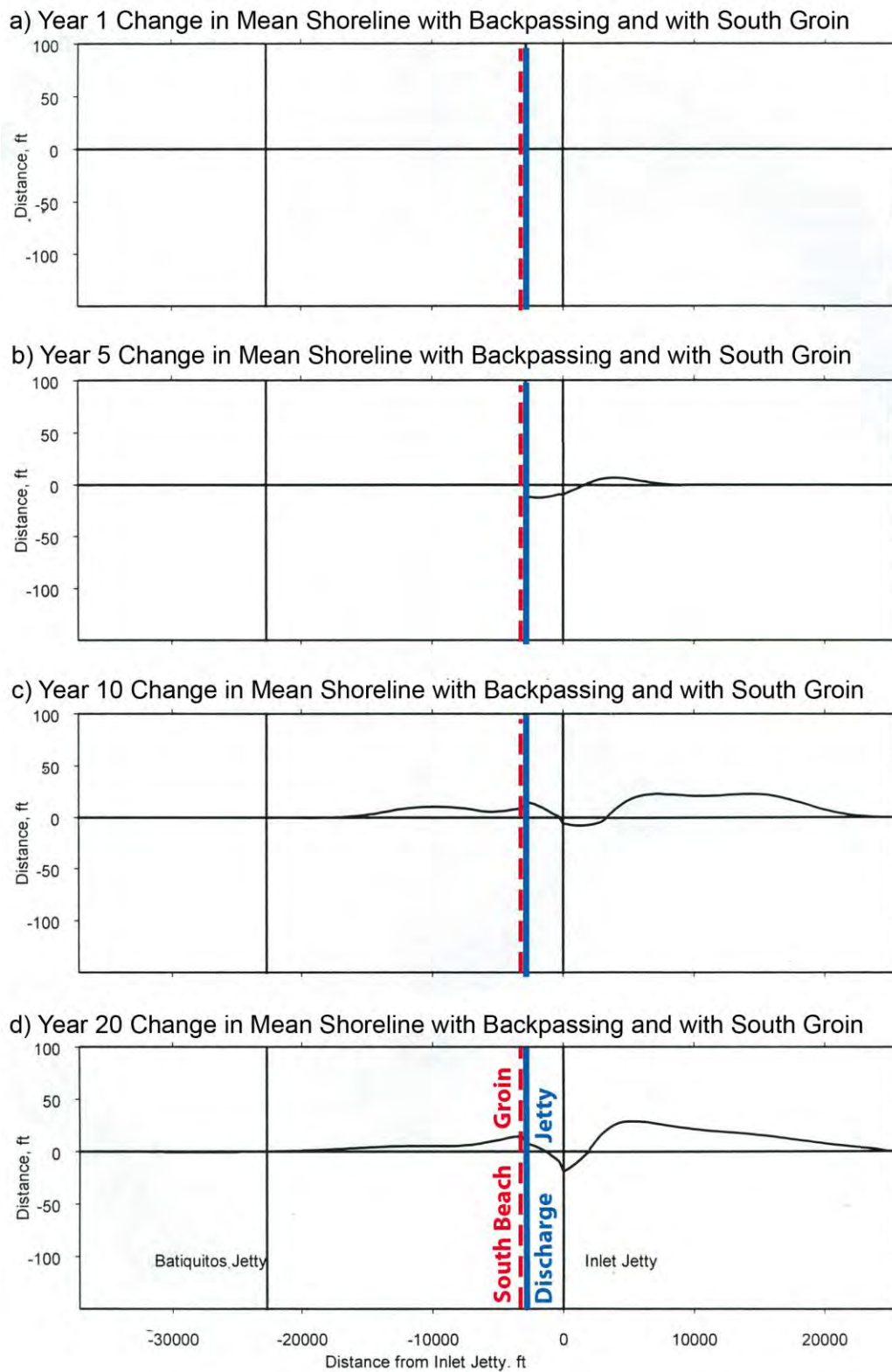
Figure 42: Shoreline evolution simulation of the cross-shore change in the mean sea level shoreline contour with the South Beach Groin in place and with historic back-passing.

The shoreline evolution is expressed on the vertical axes in terms of the cross-shore change in the position of the mean sea level contour (referred to as *mean shoreline*). Positive changes in mean shoreline position relative to the vertical axes represent accretion relative to the $t = 0$ shoreline (start of the simulation); and negative values represent erosion, or shoreline retreat relative to the $t = 0$ shoreline. Figure 43 gives the corresponding 20-year shoreline evolution when the South Beach Groin is removed, but with historic back-passing still occurring during each dredge cycle.

Comparing Figure 42 vs. Figure 43, several features become apparent with respect to shoreline changes related to removal of the South Beach Groin. 1) The South Beach Groin has no apparent effect on shoreline change over the short-term. Only after five years is there a discernible difference in shoreline change in the absence of the South Beach Groin, and this difference is localized to South Beach, where removal of the South Beach Groin causes a small amount of shoreline retreat on the order of 6 ft in the immediate neighborhood of the groins present location (400 ft to 500 ft south of the discharge channel). 2) Shoreline change impacts related to removal of the South Beach Groin are cumulative over time and generally erosional in nature relative to the present condition with the groin in place. Over longer time periods (10 yr. to 20 yr.) these erosional impacts are not confined to the immediate neighborhood of the present location of the South Beach Groin, but the largest impacts occur at South Beach where beach widths are reduced locally by as much as 17 ft, 20 years after the groin is removed. The reason shoreline change impacts related to removal of the South Beach Groin are cumulative and not localized entirely to South Beach is because of the long term effects of back-passing.

Back-passing creates a closed, re-cycling loop of beach sand between North Beach, Middle Beach and South Beach in an otherwise open-ended littoral transport system (the Oceanside Littoral Cell) in which sand would naturally pass through these beaches with the net southward littoral drift. Any perturbation inside this re-cycling loop that reduces the residence time of sand will gradually (over time) impact all three beaches (North Beach, Middle Beach and South Beach). When the concept of residence time is used in reference to the amount of time that dredged beach fill remains on a receiver
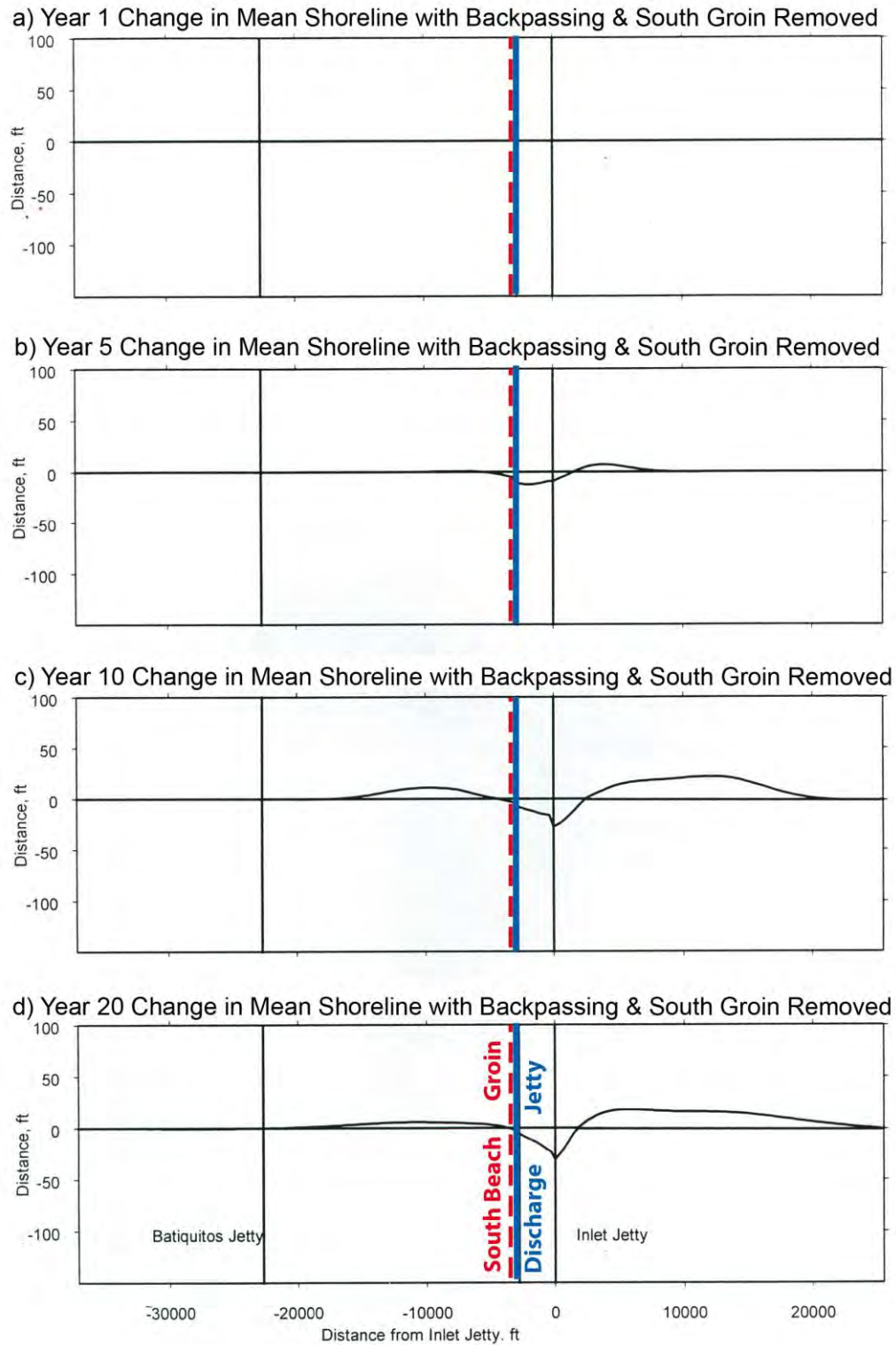
Figure 43: Shoreline evolution simulation of the cross-shore change in the mean sea level shoreline contour with the South Beach Groin in place and with historic backpassing.
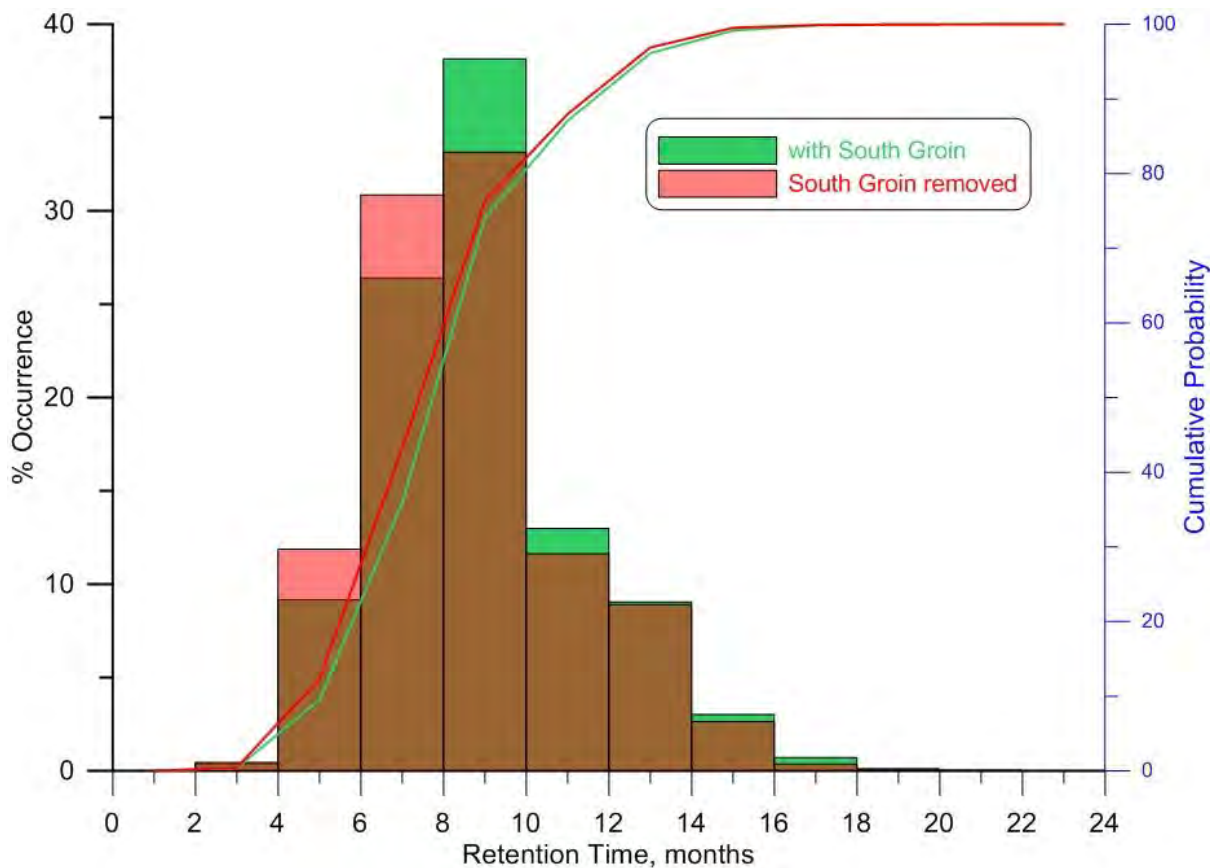
Figure 44: Probability density and cumulative probability of retention time of dredged sands placed on South Beach with the South Groin in place (green) vs with the South Groin removed (red).

beach, it is referred to as ***retention time***. Figure 44 gives the probability density and cumulative probability of retention time of dredged sands placed on South Beach in any arbitrary dredge cycle during the long-term CEM simulations. Solutions calculated with the South Groin in place are shown in green, while those for the South Groin removed are shown in red. Brown shows overlap between the two sets of solutions. The cumulative probability curves show that removal of the South Beach Groin reduces the median retention time of dredged sands placed on South Beach by 1 month; while longer retention times on the order of 18 months to 20 months are only possible with the South Beach Groin remaining in its present condition and location. Since dredging and beach disposal of the dredged sands typically occurs every 2 years, an average loss of 1 month of retention time adds up to a significant loss of beach sand volume over many years (on the order of 20 yr.) for the North Beach/Middle Beach/South Beach back-passing/ sand re-cycling system.

5.0) Conclusions:

This study invokes a well-tested and peer-reviewed Coastal Evolution Model to assess potential beach impacts in the near-field of Encina Power Station as a consequence of removal of the stone rip-rap jetty on South Beach (South Beach Groin) that presently amours a fuel oil pipeline. (This pipeline is being de-commissioned by the power station). From computer simulations using this model to predict shoreline evolution over 20-year long historic periods of waves, tides, currents and dredge disposal, the following conclusions were reached: 1) The South Beach Groin has no apparent effect on shoreline change over the short-term. Only after five years is there a discernible difference in shoreline change in the absence of the South Beach Groin, and this difference is localized to South Beach, where removal of the South Beach Groin causes a small amount of shoreline retreat on the order of 6 ft in the immediate neighborhood of the groin's present location (400 ft to 500 ft south of the discharge channel). 2) Shoreline change impacts related to removal of the South Beach Groin are cumulative over time and generally erosional in nature relative to the present condition with the groin in place. Over longer time periods (10 yr. to 20 yr.) these erosional impacts are not confined to the immediate

neighborhood of the present location of the South Beach Groin, but the largest impacts occur at South Beach where beach widths are reduced locally by as much as 17 ft, 20 years after the groin is removed. Removal of the South Beach Groin reduces the median retention time of dredged sands placed on South Beach by 1 month; while longer retention times on the order of 18 months to 20 months are only possible with the South Beach Groin remaining in its present condition and location. The reason shoreline change impacts related to removal of the South Beach Groin are cumulative and not localized entirely to South Beach is because of the long term effects of back-passing. Since dredging and beach disposal of the dredged sands typically occurs every 2 years, an average loss of 1 month of retention time adds up to a significant loss of beach sand volume over many years for the North Beach/Middle Beach/South Beach back-passing, sand re-cycling system.

6.0) Peer Reviewed Model Publications:

Jenkins, S. A. & D. L. Inman, 1999, "Sand transport mechanics for equilibrium tidal inlets," *Shore & Beach* (Magoon Volume, Jan 99), v. 67, n. 1, p. 53–58.

Grant, S.B., J.H. Kim, B.H.Jones, **S.A. Jenkins**, J.Wasyl, and C.Cudaback, 2005, "Surf zone entrainment, along-shore transport, and human health implications of pollution from tidal inlets," *Jour. Geophys. Res.,* v.110, C10025, doi:10.1029/2004JC002401, 20 pp.

Jenkins, S. A. and D. L. Inman, 2006, "Thermodynamic solutions for equilibrium beach profiles", *Jour. Geophys. Res.,* v.3, C02003, doi:10.1029, 21pp.

Jenkins, S. A., Inman, D.L., Michael D. Richardson, M.D., Thomas F. Wever, T.F. and J. Wasyl, 2007, "Scour and burial mechanics of objects in the nearshore", *IEEE Jour.Oc.Eng*, vol. 32, no. 1, pp 51-65.

7.0) Agua Hedionda Lagoon Studies and Related Technical Reports:

Jenkins, S. A., D. W. Skelly & J. Wasyl, 1989, "Dispersion and momentum flux study of the cooling water outfall at Agua Hedionda," *SIO Reference Series* No. 89-17, 36 pp.

Jenkins, S. A. and J. Wasyl, 1994, "Numerical modeling of tidal hydraulics and inlet closures at Agua Hedionda Lagoon," submitted to San Diego Gas and Electric Co., 91 pp.

Jenkins, S. A. and J. Wasyl, 1996, "Analysis of inlet closure risks at Agua Hedionda Lagoon, CA and potential remedial measures," submitted to San Diego Gas and Electric, Co., 316 pp.

Jenkins, S. A. and J. Wasyl, 1998, "Coastal processes analysis of maintenance dredging requirements for Agua Hedionda Lagoon," submitted to San Diego Gas and Electric Company, 176 pp. + 60 figs. + 8 appens.

Jenkins, S. A. and J. Wasyl, 1999, "Coastal currents in the neighborhood of Agua Hedionda Lagoon during the migration period of the Tidewater Goby," submitted to Cabrillo Power 1LLC, 34 pp., + 2 appens.

Jenkins, S. A. and J. Wasyl, 2001, "Agua Hedionda Lagoon North Jetty Restoration Project sand influx study," submitted to Cabrillo Power 1LLC, 178 pp., + 2 appens.

Jenkins, S. A. and J. Wasyl, 2001, "Hydrodynamic modeling of dispersion and dilution of concentrated seawater produced by the Ocean Desalination Project at the Encina Power Plant, Carlsbad, CA," submitted to Poseidon Resources, 186 pp.

Jenkins, S. A. and J. Wasyl, 2003, "Sand influx at Agua Hedionda Lagoon in the aftermath of the San Diego Regional Beach Sand Project," submitted to Cabrillo Power 1LLC, 107 pp., + 2 appens.

Jenkins, S. A. and J. Wasyl, 2005, "Coastal evolution model," Scripps Institution of Oceanography Tech. Rpt. No. 58, 179 pp + appendices. http://repositories.cdlib.org/sio/techreport/58/

8.0) References

Abbott, M. B., A. Damsgaard and G. S. Rodenhuis, 1973, ASystem 21, Jupiter,@ *Jour. Hydraulic Res.*, v. 11, n. 1.

AMEC, 2002, "Regional Beach Sand Project Post-construction Monitoring Report for Intertidal, Shallow Subtidal and Kelp Forest Resources", submitted to SANDAG, http://www.sandag.org.

Connor, J. J. and J. D. Wang, 1973, AFinite element modeling of two-dimensional hydrodynamic circulation,@ *MIT Tech. Rpt.*, #MITSG 74-4, p. 1-57.

Elwany, M. H. S., A. L. Lindquist, R. E. Flick, W. C. O'Reilly, J. Reitzel and W. A. Boyd, 1999, "Study of Sediment Transport Conditions in the Vicinity of Agua Hedionda Lagoon," submitted to California Coastal Commission, San Diego Gas & Electric, City of Carlsbad.

Elwany, M. H. S., R. E. Flick, M. White, and K. Goodell, 2005, "Agua Hedionda Lagoon Hydrodynamic Studies," prepared for Tenera Environmental, 39 pp. + appens.

Ellis, J.D., 1954, "Dredging Final Report, Agua Hedionda Slough Encina Power Station," San Diego Gas and Electric Co., 44pp.

Gallagher, R. H., 1981, *Finite Elements in Fluids*, John Wiley & Sons, New York, 290 pp.

Inman, D. L. and B. Brush, 1970, "The coastal challenge" *Science*, vol38, no. 5 pp36-45.

Inman, D. L. & S. A. Jenkins, 1985, "Erosion and accretion waves from Oceanside Harbor," p. 591-593, in *Oceans '85: Ocean Engineering and the Environment,* IEEE and Marine Technology Society, v. 1, 674 pp.

Inman, D. L. and Masters, P. M., 1991, "Coastal sediment transport concepts and mechanisms," Chapter 5 (43 pp.) in *State of the Coast Report, San Diego Region, Coast of California Storm and Tidal waves Study*, U. S. Army   Corps of Engineers, Los Angeles District Chapters 1-10, Appen. A-I, 2 v.

Inman, D. L., M. H. S. Elwany and S. A. Jenkins, 1993, "Shorerise and bar-berm profiles on ocean beaches," *Jour. Geophys. Res.*, v. 98, n. C10, p. 18,181-199.

Inman, D. L., S. A. Jenkins, and M. H. S. Elwany, 1996, "Wave climate cycles and coastal engineering practice," *Coastal Eng., 1996, Proc. 25th Int. Conf.,(Orlando)*, Amer. Soc. Civil Eng., Vol. 1, Ch. 25, p. 314–327.

Inman, D. L. & S. A. Jenkins, 1997, "Changing wave climate and littoral drift along the California coast," p. 538-549 in O. T. Magoon et al., eds., *California and the World Ocean '97*, ASCE, Reston, VA, 1756 pp

Inman, D. L. & S. A. Jenkins, 1999, "Climate change and the episodicity of sediment flux of small California rivers," *Jour. Geology,* v. 107, p. 251–270.

Inman, D. L. & S. A. Jenkins, 2004, "Scour and burial of objects in shallow water," p. 1020–1026 in M. Schwartz, ed., *Encyclopedia of Coastal Science*, Kluwer Academic Publishers, Dordrecht, Netherlands.

Jenkins, S. A. and D. W. Skelly, 1988, "An Evaluation of the Coastal Data Base Pertaining to Seawater Diversion at Encina Power Plant Carlsbad, CA," submitted to San Diego Gas and Electric, Co., 56 pp.

Jenkins, S. A., D. W. Skelly, and J. Wasyl, 1989, "Dispersion and Momentum Flux Study of the Cooling Water Outfall at Agua Hedionda," submitted to San Diego Gas and Electric, Co., 36 pp. + appens.

Jenkins, S. A. and J. Wasyl, 1993, "Numerical Modeling of Tidal Hydraulics and Inlet Closures at Agua Hedionda Lagoon," submitted to San Diego Gas and Electric, Co., 91 pp.

Jenkins, S. A. and J. Wasyl, 1994, "Numerical Modeling of Tidal Hydraulics and Inlet Closures at Agua Hedionda Lagoon Part II: Risk Analysis," submitted to San Diego Gas and Electric, Co., 46 pp. + appens.

Jenkins, S. A. and J. Wasyl, 1995, "Optimization of Choke Point Channels at Agua Hedionda Lagoon using Stratford Turbulent Pressure Recovery," submitted to San Diego Gas and Electric, Co., 59 pp.

Jenkins, S. A. and J. Wasyl, 1997, "Analysis of inlet closure risks at Agua Hedionda Lagoon, CA and potential remedial measures, Part II," submitted to San Diego Gas and Electric, Co., 152 pp. + appens.

Jenkins, S. A. and J. Wasyl, 1998a, Analysis of Coastal Processes Effects Due to the San Dieguito Lagoon Restoration Project: Final Report, submitted to Southern California Edison Co., 333 pp.

Jenkins, S. A. and J. Wasyl, 1998b, Coastal Processes Analysis of Maintenance Dredging Requirements for Agua Hedionda Lagoon, submitted to San Diego Gas and Electric Co., 176 pp. + appens.

Jenkins, S. A. and D. L. Inman, 1999, A Sand transport mechanics for equilibrium in tidal inlets, *Shore and Beach*, vol. 67, no. 1, pp. 53-58.

Jenkins, S. A. and J. Wasyl, 2001, Agua Hedionda Lagoon North Jetty Resoration Project: Sand Influx Study, submitted to Cabrillo Power LLC., 178 pp. + appens.

Jenkins, S. A. and J. Wasyl, 2003, Sand Influx at Agua Hedionda Lagoon in the Aftermath of the San Diego Regional Beach Sand Project, submitted to Cabrillo Power LLC., 95 pp. + appens

Jenkins, S. A. and J. Wasyl, 2005, Hydrodynamic Modeling of Dispersion and Dilution of Concentrated Sea Water Produced by the Ocean Desalination Project at the Encina Power Plant, Carlsbad, CA. Part II: Saline Anomalies due to Theoretical Extreme Case Hydraulic Scenarios, submitted to Poseidon Resources, 97 pp.

Jenkins, S. A. and J. Wasyl, 2005, "Oceanographic considerations for desalination plants in Southern California coastal waters," Scripps Institution of Oceanography Tech. Rpt. No. 54, 109 pp + appendices.
http://repositories.cdlib.org/sio/techreport/54/

Jenkins, S. A. and J. Wasyl, 2005, "Coastal evolution model," Scripps Institution of Oceanography Tech. Rpt. No. 58, 179 pp + appendices.
http://repositories.cdlib.org/sio/techreport/58/

Jenkins, S. A. and D. L. Inman, 2006, "Thermodynamic solutions for equilibrium beach profiles", *Jour. Geophys. Res.,* v.3, C02003, doi:10.1029, 21pp.

Jenkins, S. A., Inman, D.L., Michael D. Richardson, M.D., Thomas F. Wever, T.F. and J. Wasyl, 2007, "Scour and burial mechanics of objects in the nearshore", *IEEE Jour.Oc.Eng*, vol.32, no. 1, pp 78-90.

Leendertse, J. J., 1970, AA water quality model for well-mixed estuaries and coastal seas,@ vol. I, *Principles of Computation*, Memorandum RM-6230-RC, The Rand Corporation, Santa Monica, California, Feb.

Liebeck, R. H., 1976, "On the design of subsonic airfoils of high lift," paper no. 6463, McDonnell Douglas Tech. Report, 25 pp.

Liebeck, R.H., and Ormsbee, A.I., "Optimization of Airfoils for Maximum Lift," *AIAA Journal of Aircraft*, v. 7, n. 5, Sept-Oct 1970.

McCormick, B., 1979, *Aerodynamics, Aeronautics and Flight Mechanics*, John Wiley & Sons, New York, 652 pp.

NOAA, 1998, AVerified/Historical Water Level Data@ http://www.opsd.nos.noaa.gov/data_res.html

NWS, 2009, "National Weather Service Daily Climate Reports," http://www.wrh.noaa.gov/sgx/obs/rtp/carlsbad.html

Stratford, B.S., 1959, The Prediction of Separation of the Turbulent Boundary Layer, *Jour. Fluid Mech.*, v. 5.

Stratford, B.S., 1959, An Experimental Flow with Zero Skin Friction Throughout its Region of Pressure Rise, *Jour. Fluid Mech.*, v. 5.

Tenera Environmental, 2009, "EPS Field Data.xls" un-published salinity data during the Impingement and Entrainment Assessment

Tetra Tech, 2007, "Agua Hedionda Watershed Water Quality Analysis and Recommendations Report", submitted to City of Vista, CA, 91 pp.

Weiyan, T., 1992, *Shallow Water Hydrodynamics*, Water & Power Press, Hong Kong, 434 pp.

APPENDIX A: Historic Dredge Disposal and Beach Nourishment Occurring Outside of Agua Hedionda Lagoon Operations

Table A-1: Dredge Disposal and Beach Nourishment Occurring Outside of Agua
Hedionda Lagoon Operations

Year	Amt. Dredged (yd^3)	Material Source	Disposal Location	Comments
1942	500000	Del Mar Boat Basin	Increase grade around Boat Basin	Material was not placed on the beach
1944	200000	Entrance Channel	Upland	Material was not placed on the beach
1955	800,000	Harbor Construction	Oceanside Beach	Dredged Material
1960	41,000	Entrance Channel	Oceanside Beach	Dredged Material
1961	481,000	Channel	Oceanside Beach	Dredged Material
1963	3,800,000	Harbor	Oceanside Beach	1.4myd3 was new
1965	111,000	Entrance Channel	Oceanside Beach	Dredged Material
1966	684,000	Entrance Channel	2nd St.-Wisconsin St.	Dredged Material
1967	178,000	Entrance Channel	3rd St.-Tyson St.	Dredged Material
1968	434,000	Entrance Channel	River-Wilconsin St.	Dredged Material
1969	353,000	Entrance Channel	River-3rd	Dredged Material
1971	552,000	Entrance Channel	3rd-Wisconsin St.	Dredged Material
1973	434,000	Santa Margarita R.	Tyson-Wisconsin St.	New Material-Beach
1974	560,000	Entrance Channel	Tyson-Whitterby	Dredged Material
1976	550,000	Entrance Channel	Tyson-Whitterby	Dredged Material
1977	318,000	Entrance Channel	Tyson-Whitterby	Dredged Material
1981	403,000	Entrance Channel	6th St.-Buccaneer	Dredged Material
1981	403,000	Offshore Borrow Site	Oceanside Beach	Dredged Material
1982	923,000	San Luis Rey R.	Oceanside Beach	New Material-Beach
1983	475,000	Entrance Channel	Tyson Street	Dredged Material
1986	450,000	Entrance Channel	Tyson Street	Dredged Material
1988	220,000	Entrance Channel	Tyson Street	Dredged Material
1990	250,000	Entrance Channel	Tyson Street	Dredged Material
1992	106,700	Bypass System	Tyson Street	Dredged Material
1993	483,000	Modified Entrance	Tyson Street	Dredged Material
1994	40,000	Santa Margarita R.	Wisconsin St.	New Material-Beach
1994	161,000	Entrance Channel	Nearshore Wisconsin	Dredged Material
1994	150,000	Bataquitos Lagoon	Inlet South Side	New Material-Beach

Table A-1: (continued)

Year	Amt. Dredged (yd^3)	Material Source	Disposal Location	Comments
1995	1,600,000	Bataquitos Lagoon	Ponto Beach	New Material-Beach
1996	162,000	Entrance Channel	Nearshore Wisconsin	Dredged Material
1997a	150,000	Entrance Channel	Nearshore Oceanside	
1997b	100,000	Entrance Channel	Wisconsin St.	Dredged Material
2001	921,000	RBSP Offshore	Oceanside, Carslbad	New Material-Beach
	18,237,700	**Total**		

Blank Page